iScience

CellPress
OPEN ACCESS

Article

Cholesterol-binding translocator protein TSPO regulates steatosis and bile acid synthesis in nonalcoholic fatty liver disease

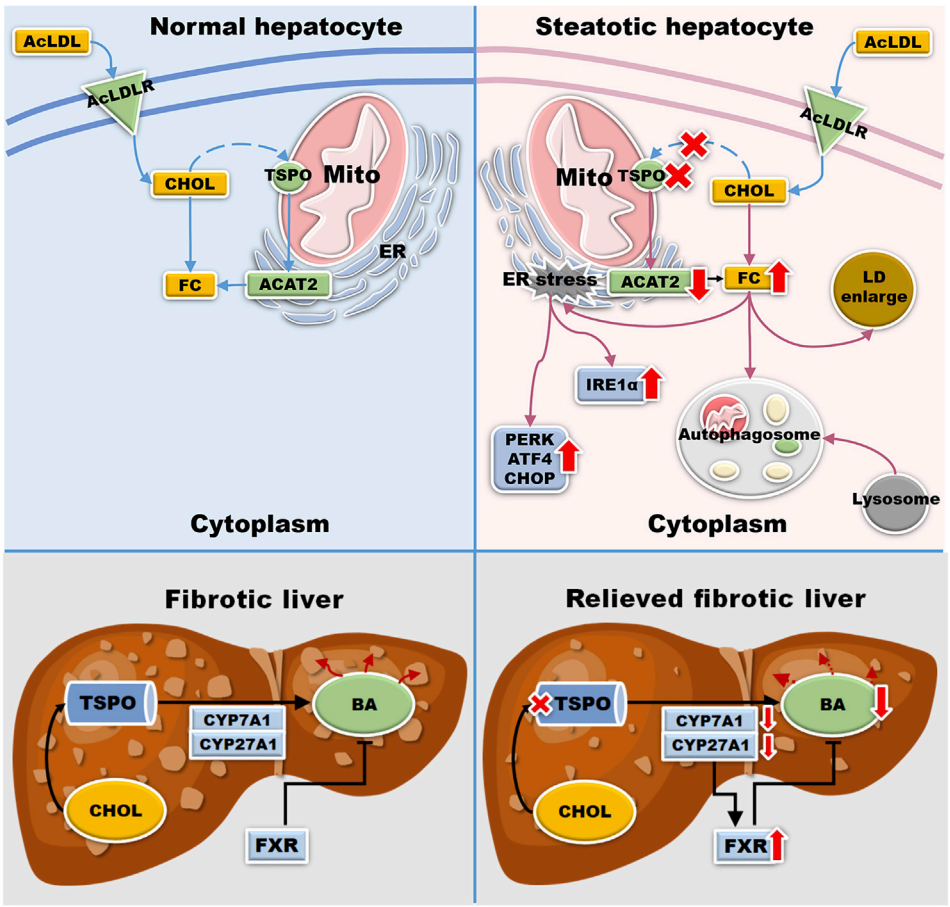

Yuchang Li, Liting Chen, Lu Li, ..., Bangyan Stiles, Kinji Asahina, Vassilios Papadopoulos

vpapadop@usc.edu

Highlights

TSPO expression levels correlate with the progression of NAFLD

TSPO deficiency inhibits ACAT2 leading to FC accumulation

Loss of TSPO in hepatocytes leads to FC accumulation that promotes simple steatosis

Loss of TSPO attenuates liver fibrosis via downregulation of bile acid production

Li et al., iScience *24*, 102457
May 21, 2021 © 2021 The Author(s).
https://doi.org/10.1016/j.isci.2021.102457

iScience

CellPress
OPEN ACCESS

Article

Cholesterol-binding translocator protein TSPO regulates steatosis and bile acid synthesis in nonalcoholic fatty liver disease

Yuchang Li,[1] Liting Chen,[1] Lu Li,[1] Chantal Sottas,[1] Stephanie K. Petrillo,[2,3] Anthoula Lazaris,[2,3] Peter Metrakos,[2,3] Hangyu Wu,[1] Yuji Ishida,[4,5] Takeshi Saito,[4,6] Lucy Golden-Mason,[4,6] Hugo R. Rosen,[4,6] Jeremy J. Wolff,[7] Cristina I. Silvescu,[7] Samuel Garza,[1] Garett Cheung,[1] Tiffany Huang,[1] Jinjiang Fan,[2,8] Martine Culty,[1] Bangyan Stiles,[1] Kinji Asahina,[6,9,10] and Vassilios Papadopoulos[1,2,8,11,*]

SUMMARY

Translocator protein (TSPO, 18 kDa) levels increase in parallel with the evolution of simple steatosis (SS) to nonalcoholic steatohepatitis (NASH) in nonalcoholic fatty liver disease (NAFLD). However, TSPO function in SS and NASH is unknown. Loss of TSPO in hepatocytes *in vitro* downregulated acetyl-CoA acetyltransferase 2 and increased free cholesterol (FC). FC accumulation induced endoplasmic reticulum stress via IRE1A and protein kinase RNA-like ER kinase/ATF4/CCAAT-enhancer-binding protein homologous protein pathways and autophagy. TSPO deficiency activated cellular adaptive antioxidant protection; this adaptation was lost upon excessive FC accumulation. A TSPO ligand 19-Atriol blocked cholesterol binding and recapitulated many of the alterations seen in TSPO-deficient cells. These data suggest that TSPO deficiency accelerated the progression of SS. In NASH, however, loss of TSPO ameliorated liver fibrosis through downregulation of bile acid synthesis by reducing CYP7A1 and CYP27A1 levels and increasing farnesoid X receptor expression. These studies indicate a dynamic and complex role for TSPO in the evolution of NAFLD.

INTRODUCTION

Nonalcoholic fatty liver disease (NAFLD) is a chronic clinicopathological condition associated with significant lipid deposition in hepatocytes and an increased risk of liver injury (Abd El-Kader and El-Den Ashmawy, 2015; Huang et al., 2020). NAFLD encompasses a wide histological spectrum of diseases ranging from simple steatosis (SS) without inflammation or fibrosis to nonalcoholic steatohepatitis (NASH) with inflammation and eventually cirrhosis and ultimately hepatocellular carcinoma (HCC) (Brown and Kleiner, 2016; Kleiner et al., 2005; Takahashi and Fukusato, 2014). In Western countries, NAFLD has become one of the most prevalent chronic liver diseases (Benedict and Zhang, 2017). Therefore, it is of crucial importance to impede SS and NASH progression because these two stages can still be reversed to normal (Kleiner et al., 2005).

Translocator protein (TSPO; 18 kDa), a ubiquitous high-affinity cholesterol- and drug-binding protein located in the outer mitochondrial membrane (OMM), has been well-characterized by its direct or indirect involvement in numerous biological functions, including mitochondrial cholesterol transport, steroid hormone biosynthesis, cell proliferation, apoptosis, porphyrin transport, heme synthesis, and anion transport (Papadopoulos et al., 2006, 2018). In a normal human liver, TSPO expression is low (Papadopoulos et al., 2006; Savino et al., 2016) but increases in NAFLD (Hatori et al., 2015). Recent studies demonstrated serious steatosis aggregates and necroinflammatory infiltration during the progression from NASH to HCC in the higher-uptake regions of ^{18}F-FEDAC, a radiotracer specific for TSPO (Hatori et al., 2014; Xie et al., 2012). Therefore, TSPO has been proposed as a specific molecular imaging biomarker of NAFLD. However, the function of TSPO in the progression of NAFLD is still unknown.

Total cholesterol (TC) is present as unesterified free cholesterol (FC) and cholesteryl ester (CE). Acyl-coenzyme A: cholesterol acyltransferase (ACAT) is an intracellular enzyme that catalyzes the formation of CE

[1]Department of Pharmacology and Pharmaceutical Sciences, School of Pharmacy, University of Southern California, Los Angeles, CA 90089, USA

[2]Research Institute of the McGill University Health Center, Montreal, QC H4A 3J1, Canada

[3]Department of Surgery, McGill University, Montreal, QC H3G 1A4, Canada

[4]Department of Medicine, Division of Gastrointestinal and Liver Diseases, Keck School of Medicine, University of Southern California, Los Angeles, CA 90089, USA

[5]Research & Development Department, PhoenixBio, Co., Ltd, Higashi-Hiroshima, Hiroshima, Japan

[6]University of Southern California Research Center for Liver Diseases, Los Angeles, CA 90089, USA

[7]Bruker Daltonics, 40 Manning Road Billerica, MA 01821, USA

[8]Department of Medicine, McGill University, Montreal, QC H4A 3J1, Canada

[9]Department of Pathology, Keck School of Medicine, University of Southern California, Los Angeles, CA 90089, USA

[10]Southern California Research Center for ALPD and Cirrhosis, Los Angeles, CA 90089, USA

[11]Lead contact

*Correspondence: vpapadop@usc.edu

https://doi.org/10.1016/j.isci.2021.102457

This is an open access article under the CC BY-NC-ND license (http://creativecommons.org/licenses/by-nc-nd/4.0/).

from FC and long-chain fatty acyl-CoA (Chang et al., 1998). The ACAT family includes two members, ACAT1 and ACAT2. In the liver, ACAT1 is distributed only in Kupffer cells (Parini et al., 2004), whereas ACAT2 is expressed primarily in hepatocytes (Anderson et al., 1998). Thus, ACAT regulates the balance between FC and CE forms. Any perturbation of this balance will disrupt cholesterol homeostasis and lead to pathological conditions, from hypercholesterolemia (Daniels et al., 2009) to NAFLD (Lee et al., 2009; Tous et al., 2005). Mice fed with a high-fat diet showed FC accumulation in mouse hepatic stellate cells (HSCs), which further sensitized these cells to TGFβ-induced activation, leading to exaggerated liver fibrosis in NASH (Tomita et al., 2014). In addition, after treatment of isolated liver sinusoidal endothelial cells with acetylated LDL (AcLDL) and ACAT inhibitor 58035 (3-[decyldimethylsilyl]-N-[2-{4-methylphenyl}-1-phenylethyl] propenamide), FC but not CE levels were significantly increased in endolysosome-enhanced TLR9-mediated signaling (Teratani et al., 2017), exacerbating the TLR9/inflammasome pathway in the liver. In the HCC cell line Huh7, acute accumulation of FC induced the degradation of perilipin 2 and Rab18-dependent fusion of the endoplasmic reticulum (ER) and lipid droplets (LDs) (Makino et al., 2016), thus perturbing cholesterol metabolism. Increased hepatic FC correlated with disease progression in patients, without CE alteration (Puri et al., 2007). These results indicated that FC accumulation, but not CE, marked NAFLD progression. However, whether TSPO affects NAFLD progression through FC accumulation remains unknown.

In this study, we induced lipid accumulation *in vitro* by treating Huh7 cells or primary mouse hepatocytes with either AcLDL to increase TC or AcLDL+58035 to induce FC accumulation in the presence or absence of TSPO. We also treated Huh7 cells with 19-Atriol, a ligand binding at the cholesterol recognition amino acid consensus (CRAC) domain of TSPO (Midzak et al., 2011), to inhibit cholesterol binding to assess whether it can reproduce the effects exhibited after loss of TSPO function. We examined FC accumulation, LD alterations, and the TSPO-ACAT2 association. Furthermore, we investigated the effect of FC accumulation on ER stress and autophagy. We also induced *in vivo* NASH in wild-type and TSPO-knockout (KO) rats using the methionine-choline-deficient (MCD) diet and investigated the role of TSPO in the fibrotic liver.

RESULTS

TSPO levels correlated with the progression for NAFLD

Although TSPO was reported to be a potential indicator for NAFLD progression (Hatori et al., 2014; Xie et al., 2012), there has surprisingly been no comprehensive study of TSPO expression across the spectrum of NAFLD. To that end, we examined TSPO expression at all stages of NAFLD in the human and mouse. The human liver samples were first blind scored using the NAFLD activity score (NAS) system by a pathologist, regardless of gender. A total of 12 samples were randomly picked as representative of different liver stages by NAS grades of normal, steatosis, NASH, and cirrhosis (n = 3 for each stage) for further analysis (Table S1). TSPO immunoreactivity was low in a normal liver but elevated in SS, NASH, and cirrhotic livers (Figure 1A, black arrows). After the removal of areas of blood and vessels by ImageJ software, TSPO signal intensity was significantly higher in patients with steatosis, NASH, and cirrhosis than in controls, and this increase was proportional to the extent of liver damage.

We assessed TSPO expression in mouse liver sections from different stages of NAFLD generated in mice fed with a diet rich in fructose, palmitate, and cholesterol (Wang et al., 2016). The steatosis group (n = 12) was generated after 20 weeks of feeding with a fructose-palmitate-cholesterol diet (FPC) supplemented with 0.05% cholesterol, and the NASH group (n = 9) was generated after 22 weeks of feeding with a FPC diet supplemented with 1.2% cholesterol. The control group (n = 6) was generated after 20 weeks of feeding with a chow diet. TSPO immunoreactivity was seen by immunofluorescence in control samples (Figure 1B). The TSPO positive signal was significantly higher in steatosis and highest in NASH samples (Figure 1B). qPCR analysis indicated corresponding increases in *Tspo* mRNA expression in these models, which gradually increased from control (1×) to steatosis (1.99×) to NASH (2.68×) (Figure 1C). Taken together, TSPO expression levels correlated with the progression from control, steatosis, and onto the NASH stage.

FC and TAG accumulation in TSPO-deficient cells after AcLDL+58035 treatment

To examine the role of TSPO in human liver cells, we generated a stable TSPO knockdown (KD) Huh7 hepatocarcinoma cell line by transfection of human TSPO shRNA plasmid or scrambled shRNA plasmid-A (Scram). TSPO was significantly downregulated in TSPO-shRNA-transfected cells compared with Scram-shRNA-transfected cells (Figure 2A). The immunofluorescence staining of TSPO and MitoTracker confirmed reduced TSPO density in mitochondria by shRNA (Figure 2B).

CellPress
OPEN ACCESS

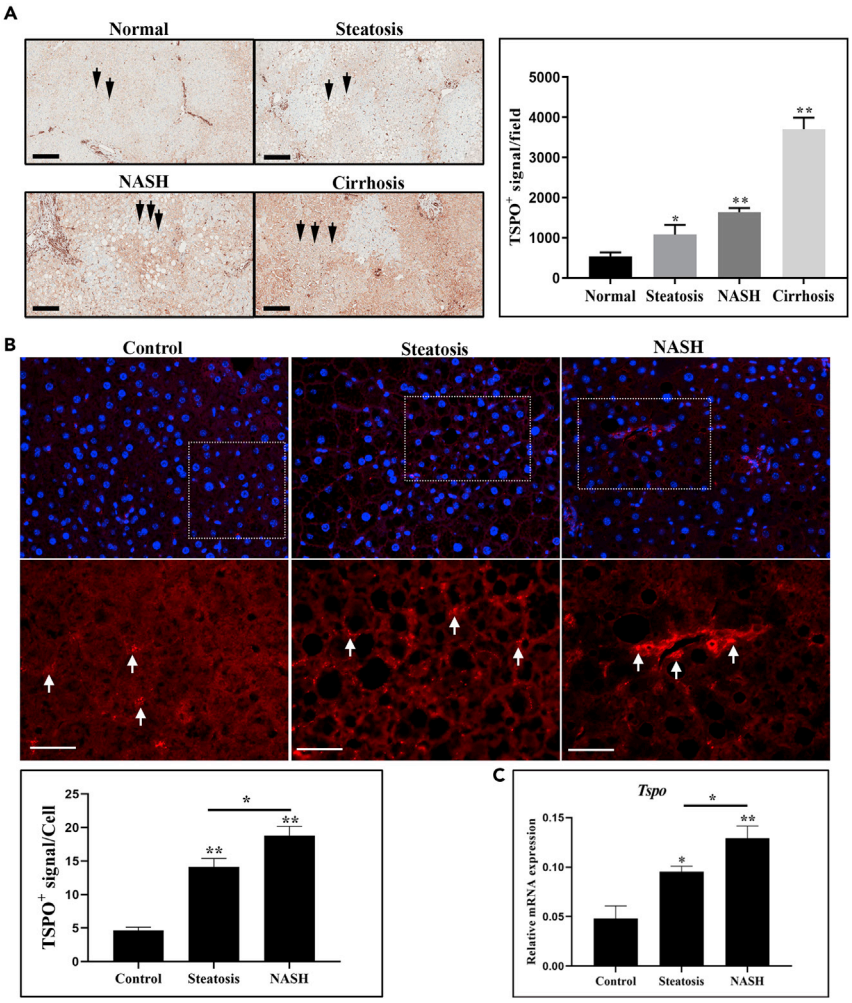

Figure 1. TSPO is an indicator of the progression of NAFLD

(A) Immunohistochemistry staining showing TSPO levels in human liver paraffin sections (n = 3). The brown color indicates a positive TSPO signal (black arrow, left panel). After the removal of areas of blood and vessels by ImageJ software, quantification showed the TSPO positive signal in each field in normal, steatosis, NASH, and cirrhosis liver (right panel). Scale, 200μm.

(B) Immunofluorescence staining showing TSPO immunoreactivity signal in control (chow diet), steatosis, and NASH mouse models. The upper panels are low magnification, and the lower panels are high magnification of the selected dotted areas. Red colors indicate positive TSPO signal (white arrow). TSPO signals were quantified in control, steatosis, and NASH models. Scale, 40 μm.

(C) qPCR data showing *Tspo/Gapdh* relative mRNA expression in mouse liver of control, steatosis, and NASH (n = 3). Data are represented as mean ± SD, *p < 0.05, **p < 0.01 by one-way ANOVA.

Using zinc finger nuclease technology, we previously generated a TSPO null mutant rat (Owen et al., 2017). Serendipitously, we observed abnormal LD accumulation in TSPO homozygous KO rats when compared with WT and heterozygous TSPO rats (Figure S1), implying a liver steatosis-like phenotype in TSPO HO KO rats. This observation prompted us to explore the possible contribution of TSPO to lipid accumulation and NAFLD. First, we demonstrated AcLDL uptake into Huh7 by visualizing the acetylated low-density lipoprotein, Dil complex (Dil-AcLDL) trafficking into the cells (Figure S2A). To assess the effect of TSPO in lipid-loaded Huh7 cells, we treated KD and Scram control Huh7 cells for 24 h with AcLDL to increase TC levels or with AcLDL +58035, the latter being an ACAT inhibitor, to block cholesterol esterification. Cell viability was measured using the MTT assay. Cell viability was significantly decreased in KD cells compared with Scram (Figure 2C). After treatment with AcLDL or AcLDL+58035, cell viability continually declined and decreased more in KD than Scram, suggesting cholesterol-lipid accumulation resulted in cell death and the presence of TSPO was essential for the maintenance of cell viability.

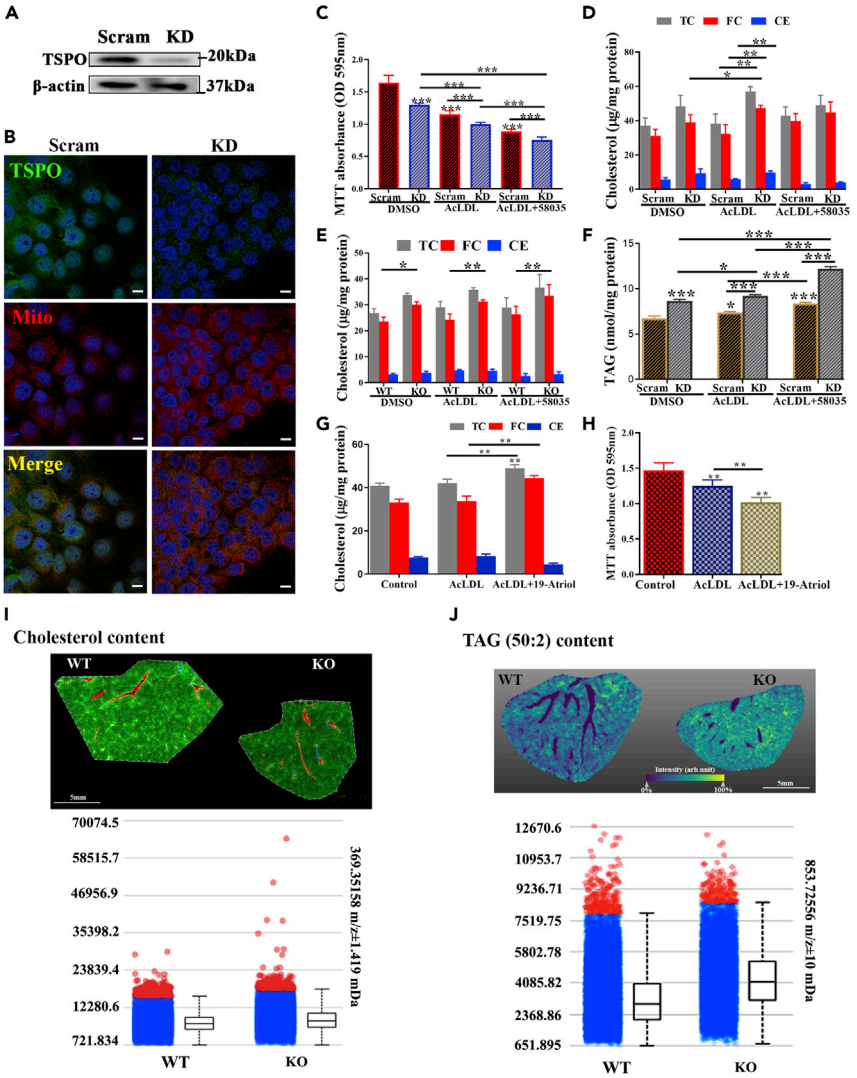

Figure 2. Total cholesterol or free cholesterol and TAG accumulation in TSPO-deficient cells

(A) Immunoblotting data showing Huh7 TSPO knock down (KD) cells. β-actin is a loading control.

(B) Colocalization of TSPO (green) and MitoTracker (Mito; red) under confocal microscopy. Scale, 10μm.

(C) MTT assay for Scram and KD cells treated with DMSO, AcLDL, or AcLDL+58035 for 24 h.

(D) Determination of TC, FC, and CE content in Scram and TSPO KD Huh7 after treatment with DMSO, AcLDL, and AcLDL+58035 for 24h.

(E) Determination of TC, FC, CE content in WT and TSPO KO primary mouse hepatocytes after treatment with DMSO, AcLDL, and AcLDL+58035 for 24 h.

(F) Determination of TAG in Scram and KD cells after treatment with DMSO, AcLDL, and AcLDL+58035 for 24 h.

(G) Determination of TC, FC, and CE after treatment with DMSO, AcLDL, and AcLDL+19-Atriol for 24 h in Huh7.

(H) MTT assay for Huh7 cells treated with DMSO, AcLDL, and AcLDL+19-Atriol for 24 h.

(I) Measurement of TC in WT and TSPO KO mouse liver by MALDI IMS. Upper: coregistration of MS image with the optical image showing morphological features: The green indicates TC perfusion throughout the liver tissue in the hepatic lobules and around vasculature; the red indicates the distribution of heme molecule from blood cells revealing vasculature. Lower: intensity plots showing cholesterol distribution in the WT and TSPO KO liver. Scale, 5 mm.

(J) Measurement of TAG (50:2) content in the WT and TSPO KO mouse liver by MALDI. Upper: the yellow indicates TAG tissue distribution and the blue shows absence of TAG from respective tissue compartments (blood vessels or biliary ducts). The TAG signal is illustrated as a color gradient from dark blue which represents absence of TAG to yellow which shows strong TAG signal. Lower: intensity plots showing TAG distribution in WT and TSPO KO liver. Scale, 5 mm. Data are represented as mean ± SD, *$p < 0.05$, **$p < 0.01$, ***$P < 0.001$ by one-way ANOVA.

CellPress
OPEN ACCESS

Next, we measured TC, FC, and CE after AcLDL or AcLDL+58035 treatment in Scram and KD cells. The results showed that AcLDL treatment slightly increased TC levels in Scram and KD cells (Figure 2D). However, there was a significant accumulation of FC in KD cells compared with Scram after AcLDL treatment. Surprisingly, TC and FC levels in KD were reduced after treatment with AcLDL+58035 compared with AcLDL (Figure 2D). Considering that cell viability decreased significantly after AcLDL+58035 treatment (Figure 2C), it is likely that excessive FC accumulation caused by 58035 led to cell death. In addition, CE levels did not change in AcLDL+58035 between Scram and KD cells. Meanwhile, we used the same treatments for 24 h on isolated hepatocytes from WT and TSPO global KO mice, previously generated in our laboratory (Fan et al., 2020). We found the treatment of hepatocytes with AcLDL or AcLDL+58035 resulted in significant increase in FC in TSPO KO cells compared with WT (Figure 2E); CE levels did not change with any treatment between WT and KO.

In addition, we isolated human hepatocytes from humanized liver-chimeric mice (Tateno et al., 2015; Yamasaki et al., 2020). After silencing TSPO using human *Tspo* siRNA (Figure S2B), we examined TC, FC, and CE levels after treatment with DMSO, AcLDL, and AcLDL+58035. The results obtained showed that FC is significantly elevated after silencing TSPO compared with WT cells after AcLDL+58035 (Figure S2C).

Next, we measured triacylglycerol (TAG) levels in KD and Scram cells after AcLDL or AcLDL+58035 treatment. The results showed that TAG was significantly elevated in KD cells versus Scram (Figure 2F). AcLDL or AcLDL+58035 treatment steadily and significantly promoted TAG accumulation in Scram and KD cells, with TAG levels increasing more in KD than in Scram, suggesting that the loss of TSPO enhances TAG accumulation when treated with AcLDL or AcLDL+58035.

To examine whether inhibition of cholesterol binding to TSPO was involved in the observed changes, we treated Huh7 cells with AcLDL or AcLDL+19-Atriol. We previously showed 19-Atriol is a drug ligand inhibiting FC binding at the TSPO CRAC domain (Chung et al., 2013; Midzak et al., 2011). The results showed that TC and FC levels significantly increased with AcLDL+19-Atriol treatment (Figure 2G). Given that FC accumulated after 19-Atriol treatment, it may contribute to reduce cell viability (Figure 2H). Taken together, these results demonstrate that loss of TSPO or inhibition of cholesterol binding to TSPO leads to TC, FC, and TAG accumulation, all hallmarks of hepatic steatosis.

To further examine lipid alteration *in vivo* after loss of TSPO, we performed matrix-assisted laser desorption/ionization imaging mass spectrometry (MALDI IMS) to assess the levels of cholesterol, TAG, and fatty acids in WT and KO mouse livers. Cholesterol was detected as $[\text{cholesterol-}H_2O + H]^+$. As seen, cholesterol (green) is evenly distributed through WT and KO livers, while the density is greater in the KO liver (Figure 2I upper). The vessels (red) were revealed by the distribution of heme molecules from blood cells. The intensity plots showed higher levels of cholesterol distribution in the TSPO KO liver compared with WT (Figure 2I lower). TAG was observed both as Na^+ and K^+ cations, with similar distributions for both. Because of the similarity between ions indicative of TAG (50:2, 52:2, 52:3, 52:4; Figure S3A), we chose TAG (50:2; yellow) for analysis (Figure 2J upper). The intensity plots indicate that TAG (50:2) levels were slightly elevated in the KO liver compared with the WT liver (Figure 2J lower). In addition, neither TAGs nor cholesterol was found in the bile ducts or blood vessels (Figure S3B). Furthermore, some free fatty acids, including palmitoleic/sapienic, linoleic/linoelaidic, oleic/elaidic/vaccenic, eicosapentaenoic, arachidonic, and docosahexaenoic acids were substantially higher in KO livers compared with WT livers (Figure S3C). These observations corroborate the results of cholesterol and TAG elevation in hepatocytes resulting from the loss of TSPO.

Loss of TSPO inhibited ACAT2 expression in mitochondrial-associated ER membranes (MAMs) in a manner independent of TC accumulation

Because FC accumulated in the absence of TSPO, we next determined whether there is an increase in cholesteryl ester hydrolase (CEH), which transforms CE to FC, or a decrease in ACAT2, which transforms FC to CE in TSPO-deficient cells. We detected CEH and ACAT2 levels in Scram and KD cells or WT and KO primary mouse hepatocytes, following the same treatment with AcLDL or AcLDL+58035 for 24 h. In Scram and KD cells, CEH did not change after treatment with DMSO, AcLDL, or AcLDL+58035 (Figure 3A). However, ACAT2 levels were significantly reduced in the absence of TSPO upon AcLDL or AcLDL+58035 treatment compared with their Scram controls (Figure 3B). This was confirmed by confocal imaging microscopy (Figure 3C). In mouse hepatocytes, CEH expression gradually increased with AcLDL or AcLDL+58035 treatment, more so in KO than WT cells (Figure 3D), while ACAT2 expression was downregulated in KO

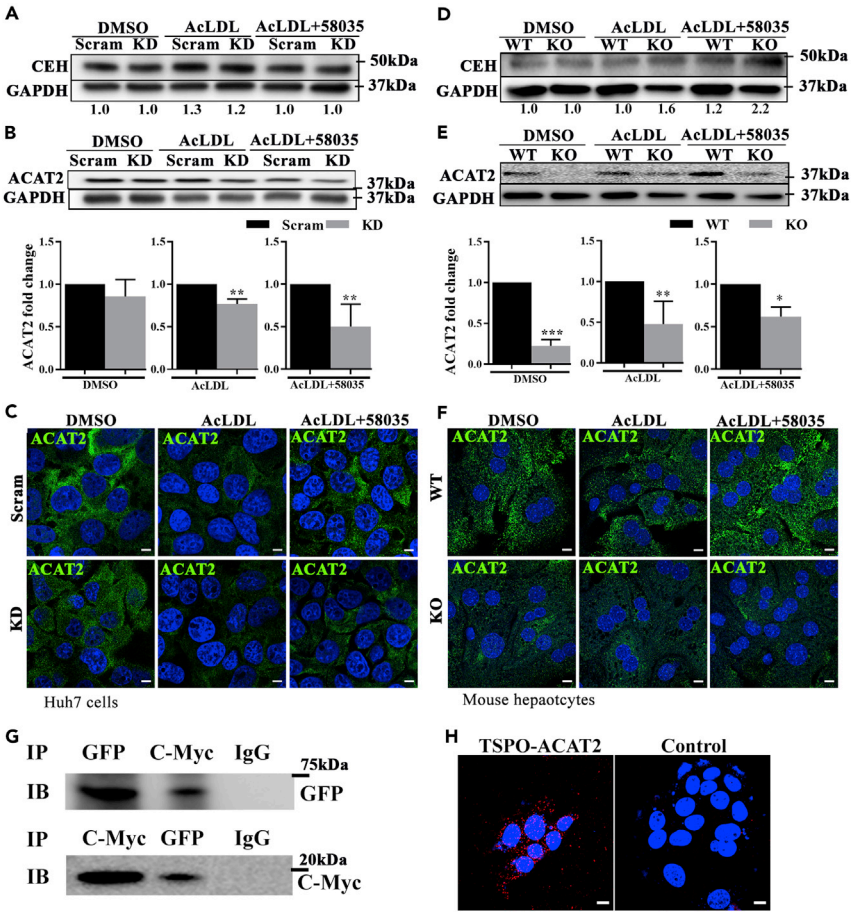

Figure 3. Loss of TSPO inhibited ACAT2 independent of cholesterol accumulation and TSPO-ACAT2 interacted in MAMs

(A) CEH immunoblots from DMSO-, AcLDL-, and AcLDL+58035-treated Scram and TSPO KD Huh7 cells. The numbers under the lanes represent the CEH/GAPDH.

(B) ACAT2 immunoblot from DMSO-, AcLDL-, and AcLDL+58035-treated Scram and TSPO KD Huh7 cells. The bar graph is the fold change of ACAT2/GAPDH.

(C) Immunofluorescence staining of ACAT2 (green) in DMSO-, AcLDL-, and AcLDL+58035-treated Scram and TSPO KD Huh7 cells. Scale, 10 μm.

(D) CEH immunoblot from DMSO-, AcLDL-, and AcLDL+58035-treated WT and TSPO KO primary mouse hepatocytes. The numbers under the lanes represent the CEH/GAPDH.

(E) ACAT2 immunoblot from DMSO-, AcLDL-, and AcLDL+58035-treated WT, TSPO KO primary mouse hepatocytes. The bar graph is the fold change of ACAT2/GAPDH.

(F) Immunofluorescence staining of ACAT2 (green) in DMSO-, AcLDL-, and AcLDL+58035-treated WT and TSPO KO primary mouse hepatocytes Scale, 10μm.

(G) Coimmunoprecipitation of ACAT2-Turbo-GFP and TSPO-Myc and immunoblot with Anti-GFP or Anti-C-Myc in Huh7 cells.

(H) PLA of ACAT2 and TSPO interactions (red spot) in Huh7 cells. Scale, 10 μm. Data are represented as mean ± SD, *$p < 0.05$, **$p < 0.01$, ***$p < 0.001$ by Student's t-test.

compared with WT, independent of AcLDL or AcLDL+58035 treatment, as shown by immunoblot or immunofluorescence staining (Figures 3E and 3F), respectively. These results indicate that the loss of TSPO inhibited ACAT2 expression in a manner independent of cholesterol accumulation.

Mitochondria are juxtaposed with the ER, forming MAMs (Vance, 2014). This interorganelle interaction is closely associated with cell stress and/or mitochondrial functions (Rizzuto et al., 1998; Zhou et al., 2020). To address whether TSPO, located at the OMM, and ACAT2, residing in the ER membrane, interact directly, we cotransfected a plasmid containing TSPO-Myc and a plasmid containing ACAT2-Turbo-GFP

into Huh7 cells and performed coimmunoprecipitation (CO-IP) studies. We validated the overexpression of ACAT2 and TSPO by immunoblotting with anti-ACAT2 and c-Myc antibodies, respectively (Figures S4A and S4B). After immunoprecipitation of anti-Turbo-GFP or c-Myc antibodies from clarified cell lysates, we performed immunoblot analysis using either anti-rabbit C-Myc or Turbo-GFP antibodies. The results show a band of 18–20 kDa, the approximate size of TSPO-Myc, after immunoprecipitation with anti-Turbo-GFP or a 68-kDa ACAT2-GFP band after immunoprecipitation with anti-C-Myc antibody (Figure 3G), suggesting that TSPO interacts directly with ACAT2. To further examine whether endogenous TSPO and ACAT2 interacts, we performed proximity ligation assay (PLA) in Huh7 cells with anti-TSPO (LifeSpan, # LS-B5755-50) and anti-ACAT2 antibodies. The confocal photomicrographs clearly show that endogenous TSPO and ACAT2 interact as seen by the red fluorescence distributed around the nuclei (Figure 3H). These observations provide strong evidence for the direct interaction between TSPO and ACAT2 at the level of MAMs. D'Eletto et al. reported first that TSPO is present in the MAM fraction and its localization is strictly transglutaminase-type-2-dependent in HEK293 cells (D'Eletto et al., 2018). Herein, we confirmed TSPO presence in MAMs and identified TSPO-ACAT2 interactions in hepatocytes.

To detect whether the TSPO-ACAT2 interaction is associated with cholesterol accumulation, we treated the Huh7 cells with DMSO, AcLDL, or AcLDL+58035 and performed immunoblotting with TSPO-Myc after immunoprecipitation with Turbo-GFP. The results show no change in the intensity of TSPO-Myc (Figures S4C and S4D), suggesting that TSPO and ACAT2 interact in a cholesterol-accumulation-independent manner.

To further explore cholesterol metabolism after the loss of TSPO, we examined the transcriptional levels of *Acat2* and liver X receptor α (*Lxrα*) and *Lxrα* downstream factors HMG-CoA reductase (*Hmgcr*) and sterol-regulatory-element-binding transcription factor 1 (*Srebp-1c*). *Acat2* mRNA showed decreased trend and *Lxrα* levels were significantly reduced after loss of TSPO in control (DMSO), AcLDL, and AcLDL+58035 treatments. Although no significant changes were seen in *Hmgcr* and *Srebp-1c* levels, the HMGCR protein was reduced in TSPO KO in all treatments examined (Figures S4E and S4F), suggesting that there was no *de novo* cholesterol synthesis. It was intriguing, however, that *Lxrα* and *Acat2* levels were both reduced in TSPO KO Huh7 compared with WT cells. This finding is in disagreement with a previous report showing that LXRα may negatively regulate ACAT2 expression (Bonamassa and Moschetta, 2013). To assess whether ACAT2 may be degraded in TSPO KO cells, ACAT2 was immunoprecipitated in extracts of mouse hepatocytes from WT and TSPO KO animals, and the precipitates were immunoblotted with an antiubiquitin antibody. The results obtained showed no changes in the ubiquitination of ACAT2 between WT and TSPO KO cells (Figure S4G), indicative of no ubiquitination-associated degradation of ACAT2 in TSPO-deficient cells.

FC accumulation after loss of TSPO enhanced LD enlargement

LDs are universal cellular organelles for the storage of neutral lipids, such as sterol esters and triacylglycerol synthesis (Farese and Walther, 2009). LDs protect cells from lipotoxic effects associated with various disease states, including obesity (Mardinoglu et al., 2015), type 2 diabetes (Sanjabi et al., 2015), liver steatosis (Gluchowski et al., 2017), and atherosclerosis (Plakkal Ayyappan et al., 2016). To detect LD alteration after loss of TSPO, we extracted LDs from DMSO, AcLDL or AcLDL+58035-treated Scram, and KD Huh7 cells. First, we validated the quality of the extracted LDs by immunoblotting for periplin2 (PLIN2), the LD surface structure protein. The results showed that PLIN2 was abundantly expressed in LDs, while no GAPDH expression was found in these LDs-enriched fractions (Figure 4A, left). In contrast, PLIN2 was weakly and GAPDH highly expressed in non-LD fractions (Figure 4A, right). Next, we stained LDs with BODIPY558/568 C12 (Figure 4B upper) and quantified the frequency distribution of LDs (size and number) by ImageJ. The results show that LDs were enlarged after TC or FC accumulation caused by AcLDL or AcLDL+58035 and this enlargement was enhanced after the loss of TSPO (Figure 4B lower).

To further confirm the effect of TSPO on neutral lipid storage, we treated WT and KO primary mouse hepatocytes with DMSO, AcLDL, or AcLDL+58035 for 24 h, followed by lipid staining with Nile red (Figure 4C upper). The lipid distribution was characterized by percentage (%) area of the stained LDs normalized by the cell number. Compared with WT, the % area of LDs/cell significantly increased in KO. Upon AcLDL or AcLDL+58035 treatment, the % area of LDs/cell in KO showed significant increase compared with WT (Figure 4C lower). The maximum LD size of each group was as follows: WT DMSO, 34.4 μm; WT AcLDL 57.4 μm; WT AcLDL+58035 71 μm, while KO DMSO, 36.5 μm; KO AcLDL, 127.1 μm, and KO AcLDL+58035, 53 μm. These results suggest that loss of TSPO played a role in the determination of LD size and numbers through TC or FC changes.

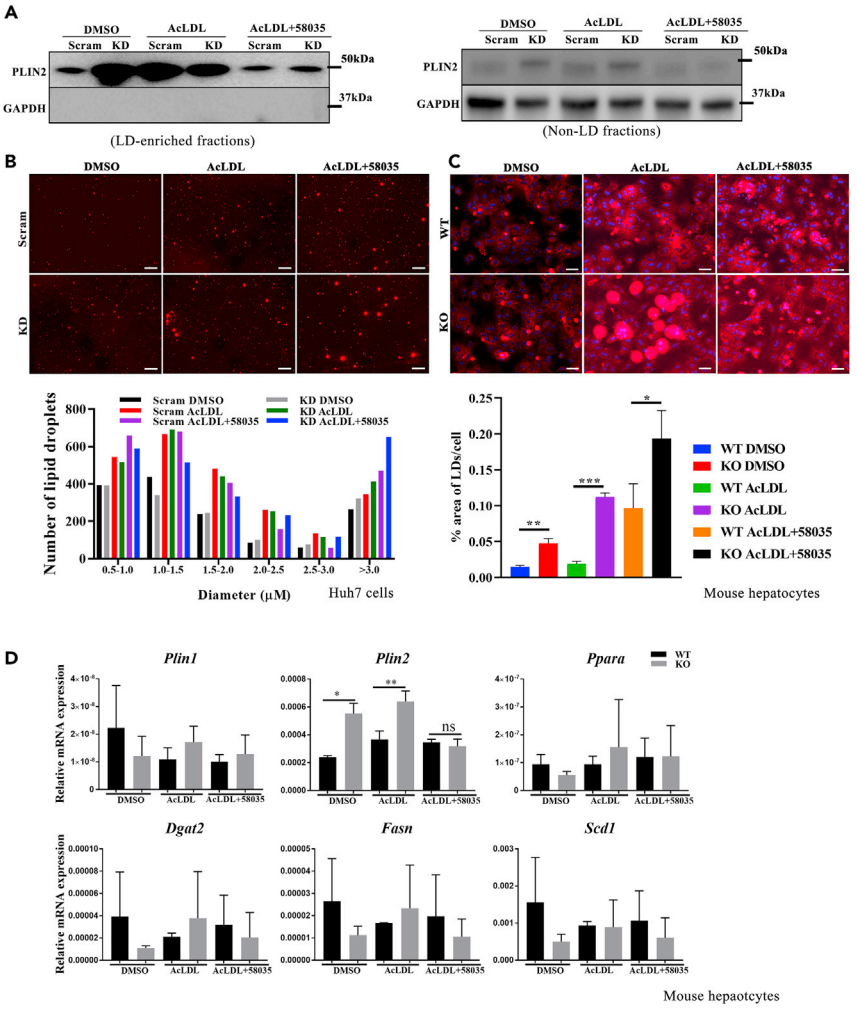

Figure 4. LDs enlargement in TSPO-deficient cells

(A) Immunoblot validation of LDs from Scram and TSPO KD cells treated with DMSO, AcLDL, and AcLDL+58035. The left panel indicates PLIN2 expression but no GAPDH in LD-enriched fraction, the right panel indicates non-LDs fraction by weak PLIN2 but normal GAPDH expression.

(B) LDs staining with BODIPY (red color). LDs size-frequency distribution quantification by ImageJ. Scale, 50 μm.

(C) Nile red staining (red color) of WT and TSPO KO primary mouse hepatocytes treated with DMSO, AcLDL, and AcLDL+58035. Nuclei were stained with DAPI. The LDs were quantified as the % area of LDs/cell. Scale, 50 μm.

(D) qPCR data showing relative mRNA levels of *Plin1*, *Plin2*, *Ppara*, *Dgat2*, *Fasn* and *Scd1* versus *Rps18* in WT and TSPO KO primary mouse hepatocytes treated with DMSO, AcLDL, and AcLDL+58035. Data are represented as mean ± SD, *$p < 0.05$, **$p < 0.01$, ***$p < 0.001$ by student's t-test.

PLIN1 and PLIN2 levels are increased in steatotic hepatocytes (Fujii et al., 2009; Straub et al., 2008) and in rodents and humans with NAFLD (Straub et al., 2008), promoting triglyceride accumulation (Imai et al., 2007). After AcLDL treatment, we found that there was a significant increase in *Plin2* but not *Plin1* expression in TSPO KO hepatocytes compared with WT cells (Figure 4D), suggesting the changes seen in LD morphology are due to changes in expression of structural LD proteins. Interestingly, we noticed that *Lxrα* levels may be positively correlated with *Plin2* at the transcriptional level (Figure S4E). Expression of *Pparα*, responsible for fatty acid β-oxidation, and the lipogenesis genes *Dgat2*, *Fasn, and Scd1* was not significantly changed after cholesterol accumulation (Figure 4D). Together, these results suggest that loss of TSPO augmented LD size partly through changes in genes important for LD structure, which agrees with previous studies (Makino et al., 2016).

We also investigated the effect of inhibiting Niemann-Pick type C1 (NPC1) on LDs in Scram and KD cells. NPC1 is a protein critical for late endosomes and lipid transport, and disruption of NPC1 by the inhibitor

CellPress
OPEN ACCESS

U18666A has been shown to result in cholesterol accumulation in lysosomes. We found that LD size increased more significantly in TSPO KD cells versus Scram in response to U18666A treatment (Figure S5A). Likewise, we found LD size is larger in KD cells than Scram after treatment with MβCD (methyl-β-cyclodextrin)/cholesterol, which depletes cholesterol, followed by loading of cholesterol in the presence of 58035 (Figure S5B). However, after treatment with the fatty acid principle monounsaturated oleic acid, we did not see changes in LD size in KD compared with Scram cells (Figure S5C), suggesting the presence of different regulatory mechanisms for TSPO in cholesterol and free fatty acid accumulation.

TSPO deficiency aggravated ER stress via excessive FC

To determine whether loss of TSPO initiated ER stress, we examined the levels of the master regulator of ER stress GRP-78 (glucose-regulated protein 78) and ER stress markers, IRE1α (inositol requiring kinase enzyme 1 alpha), PERK (protein-kinase-RNA-like ER kinase), and ATF (activating transcription factor) in primary mouse hepatocytes after treatment. With DMSO treatment, GRP-78, PERK, ATF4, and its downstream target CCAAT-enhancer-binding protein homologous protein (CHOP) showed higher levels in KO compared with WT cells, indicating ER stress induction after loss of TSPO. After AcLDL or AcLDL+58035 treatment, GRP-78, PERK, ATF4, and CHOP continuously increased in KO compared with WT cells. GRP78 and CHOP levels were quantified in the PERK/ATF4/CHOP cascade (Figure 5A). IRE1α levels increased in KO compared with WT in DMSO. After AcLDL or AcLDL+58035 treatment, IRE1α levels decreased continuously, although they remained higher in KO than those seen in WT, suggesting dynamic regulation. ATF6, another ER-stress-signal-transduction cascade marker, did not change under these conditions (Figure S6). The CHOP levels (green) in WT and KO mouse hepatocytes were confirmed by immunostaining in these treatments (Figure 5B). Given the presence of greater amounts of FC accumulation in TSPO-deficient cells, our data suggest that ER stress induced IRE1A and the PERK/ATF4/CHOP pathway after loss of TSPO and this stress was aggravated by excessive FC accumulation mainly through the PERK/ATF4/CHOP signaling pathway.

The adaptation of antioxidant defense protection was lost upon excessive FC accumulation in TSPO-deficient cells

Hepatic catalase levels indicate antioxidant defense mechanisms. To assess whether TSPO plays a role in this protective system upon cholesterol accumulation, we treated primary mouse hepatocytes with DMSO, AcLDL, or AcLDL+58035. With DMSO, catalase in KO markedly increased compared with the WT, suggesting TSPO plays a protective role in the antioxidant defense process. Moreover, the catalase levels increased more in KO cells compared with WT in response to AcLDL or AcLDL+58035 (Figure 5C). The ratio of KO/WT (numbers under the lanes) after AcLDL treatment reached the highest level (4.3:1). Then, the ratio of KO/WT upon AcLDL+58035 treatment became less compared with the ratio from AcLDL treatment (3.0:1). Thioredoxin (TRX), another antioxidant marker, is playing a key role in redox signaling by removal of reactive oxygen species and nitrogen species (Matsuzawa, 2017). Here, TRX levels increased in KO compared with WT and kept a consistent ratio (1.4:1) in DMSO and AcLDL treatments, but the ratio became less apparent (1.2:1) after AcLDL+58035 treatment (Figure 5C). These data suggest that the antioxidant defense was gradually lost upon excessive FC accumulation caused by AcLDL+58035 after loss of TSPO.

Next, we examined the levels of ACOX1 (acyl-coenzyme A oxidase 1) and PPARα, responsible for fatty acid β-oxidation in mouse hepatocytes. After AcLDL or AcLDL+58035 treatment, the ACOX1 ratio of KO/WT is 2.0:1.0:0.4 and the PPARα ratio of KO/WT is 1.4:1.7:1.3, respectively (Figure 5D). These results imply that increased fatty acid β-oxidation allowed cells to consume accumulated lipid upon DMSO or AcLDL treatment in KO. However, this consumption was compromised upon excessive FC accumulation with AcLDL+58035 treatment in KO. In agreement with this, decreased fatty acid β-oxidation led to accumulation of triglycerides in cells after the loss of TSPO (Figure 2G), which may contribute to the known insulin resistance in NAFLD.

Furthermore, we examined whether 19-Atriol treatment in Huh 7 cells could initiate ER stress or cell stress adaptation mechanisms. The results show that GRP-78, IRE1A, and CHOP levels substantially increased in response to AcLDL+19-Atriol (Figure 5E). Considering the level of FC accumulation after AcLDL+19-Atriol treatment, these results suggest that FC accumulation with 19-Atriol initiated ER stress via the IRE1A and PERK/ATF4/CHOP signaling pathways, the same pathway as loss of TSPO. Meanwhile, catalase, SOD1, and TRX levels were also elevated after AcLDL+19-Atriol treatment (Figure 5E), indicative of cell adaptation to cell stress caused by FC. Taken together, these results suggest that FC accumulation derived from either TSPO deficiency or TSPO inhibition initiated an adaptive antioxidant defense process and fatty acid

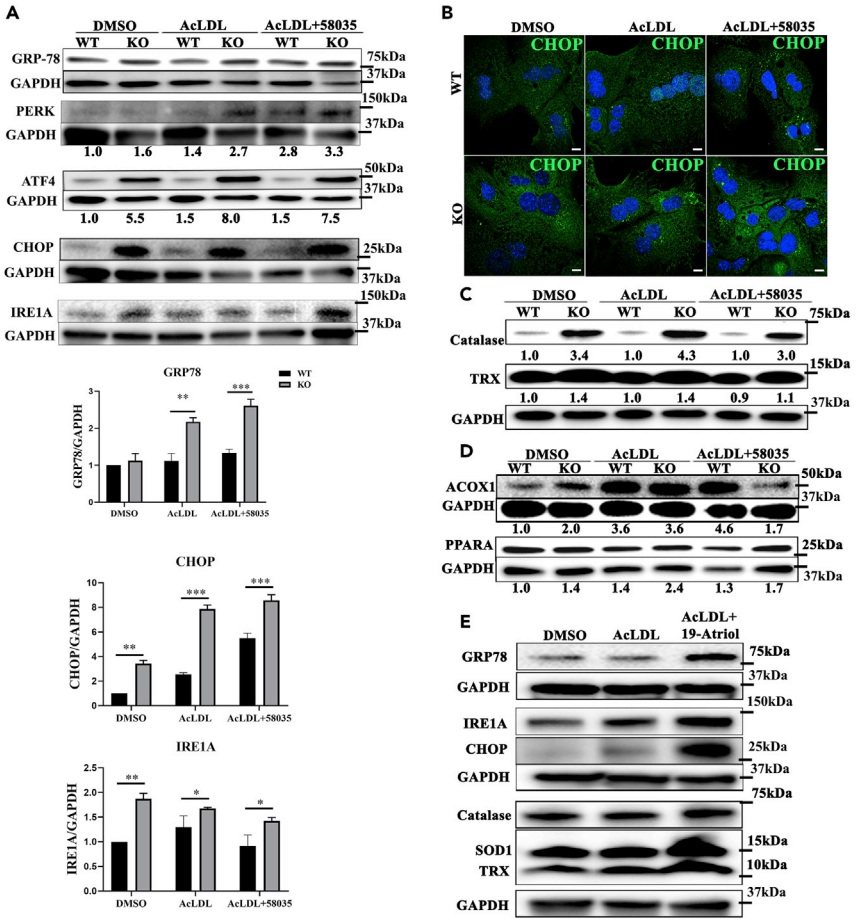

Figure 5. Loss of TSPO enhanced ER stress and adaption mechanism owing to FC accumulation

(A) Immunoblot of GRP-78, PERK, ATF4, CHOP, and IRE1A in WT and TSPO KO primary mouse hepatocytes treated with DMSO, AcLDL, and AcLDL+58035. GRP-78, CHOP, and IRE1A were quantified after DMSO, AcLDL, and AcLDL+58035 treatments.

(B) CHOP immunofluorescence staining (green) in WT and TSPO KO primary mouse hepatocytes treated with DMSO, AcLDL, and AcLDL+58035. Scale, 20 μm.

(C) Immunoblot of catalase and TRX in DMSO-, AcLDL-, and AcLDL+58035-treated WT and TSPO KO primary mouse hepatocytes.

(D) Immunoblot of ACOX1 and PPARα in WT and TSPO KO primary mouse hepatocytes treated with DMSO, AcLDL, and AcLDL+58035.

(E) Immunoblot of GRP-78, IRE1A, CHOP, catalase, SOD1, and TRX in Huh7 cells treated with DMSO, AcLDL, and AcLDL+19-Atriol. The ratio in A, C, and D indicates the densitometric analysis of the tested protein versus the corresponding GAPDH. Data are represented as mean ± SD, *$p < 0.05$, **$p < 0.01$, ***$p < 0.001$ by student's t-test.

β-oxidation. However, this adaptation was gradually lost upon excessive FC accumulation as seen with 58035 treatment, which also marks the transition from SS to late SS or early NASH.

TSPO deficiency causes autophagy

Transmission electron microscopy (TEM) was performed on Huh7 Scram and TSPO KD cells. Compared with Scram, the mitochondrial structure in KD cells was disrupted, showing that the inner mitochondrial matrix content disappeared or showed abnormal cristae (Figure 6A red arrows). LD size was enlarged in Scram but more prominent in KD after AcLDL treatment (middle, Figures 6A and S7 red arrow), consistent with our previous observations (Figure 4B). LDs were wrapped tightly by ER in AcLDL-treated Scram cells (Figure 6A black arrowhead, upper middle), suggesting active lipid mobilization at this contact site. Cholesterol accumulation with AcLDL treatment after loss of TSPO caused more autophagosome formation (Figure 6A black arrow, lower middle panel). After treatment with AcLDL+58035, Scram LD numbers increased and

CellPress
OPEN ACCESS

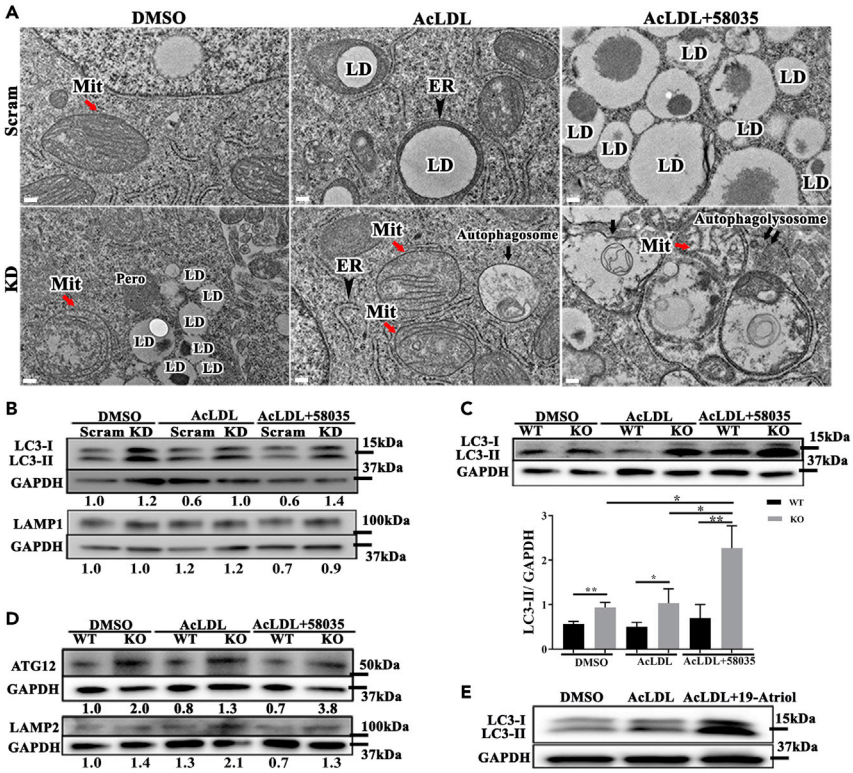

Figure 6. Loss of TSPO caused autophagy owing to FC accumulation

(A) Representative electron micrographs showing the ultrastructure of Scram and TSPO KD cells. Mitochondria (red arrow), autophagosome (black arrow) in TSPO KD after AcLDL treatment and autophagolysosome formation (double black arrows) in TSPO KD after AcLDL+58035 treatment as compared with the corresponding control. Mit, mitochondria; ER, endoplasmic reticulum (black arrowhead); LD, lipid droplet; Pero, peroxisome. Scale, 200 nm.

(B) Immunoblot of LC3 (upper) and LAMP1 (lower) in Scram and TSPO KD cells treated with DMSO, AcLDL, and AcLDL+58035. The ratio indicates the densitometric analysis of LC3-II/GAPDH.

(C and D) Immunoblot of LC3 (C), ATG12 and LAMP2 (D) in WT, and TSPO KO mouse hepatocytes treated with DMSO, AcLDL, and AcLDL+58035. LC3-II was quantified with GAPDH in (C). The ratio indicates the densitometric analysis of LC3-II/GAPDH, ATG12/GAPDH, and LAMP2/GAPDH. Data are represented as mean ± SD, *$p < 0.05$, **$p < 0.01$ by one-way ANOVA.

(E) Immunoblot of LC3 in Huh7 cells treated with DMSO, AcLDL, and AcLDL+19-Atriol.

sizes became larger (Figure 6A upper right). The treatment of AcLDL+58035 in TSPO KD showed more autophagolysosomes formation (Figure 6A double black arrows, lower right).

To determine if cholesterol accumulation affected autophagy as seen under TEM, we detected autophagy-specific markers microtubule-associated protein 1 light chain 3 (LC3) and lysosome-associated membrane protein 1 and 2 (LAMP1 and LAMP2, respectively) in Scram and KD cells and in WT and KO primary mouse hepatocytes. LC3-II was upregulated in KD cells and increased with AcLDL and AcLDL+58035 treatment compared to Scram (Figure 6B). LAMP1 did not change with DMSO or AcLDL treatment between Scram and KD but was slightly upregulated with AcLDL+58035 in KD (Figure 6B). The upregulated LC3-II and LAMP1 confirmed elevated autophagolysosome formation in TSPO KD compared with Scram under AcLDL+58035 treatment as observed under TEM (double black arrows, lower right Figure 6A). In mouse hepatocytes, LC3B-II gradually increased in TSPO KO compared with WT upon DMSO, AcLDL, and AcLDL+58035 treatment (Figure 6C). In addition, Atg12, critical for the ubiquitin-like conjugation system of autophagy and targeted to autophagosomes, was upregulated in KO cells compared with WT. Upon AcLDL or AcLDL+58035 treatment, the ratio of ATG12 between KO and WT increased (Figure 6D). In addition, LAMP2 was upregulated 1.5 times in KO primary hepatocytes compared with WT after treatment with DMSO and about 2 times after treatment with AcLDL or AcLDL+58035. These data also indicate that TC and FC accumulation from AcLDL or AcLDL+58035 treatment augmented autophagosome and autophagolysosome formation in TSPO-deficient hepatocytes (Figure 6D).

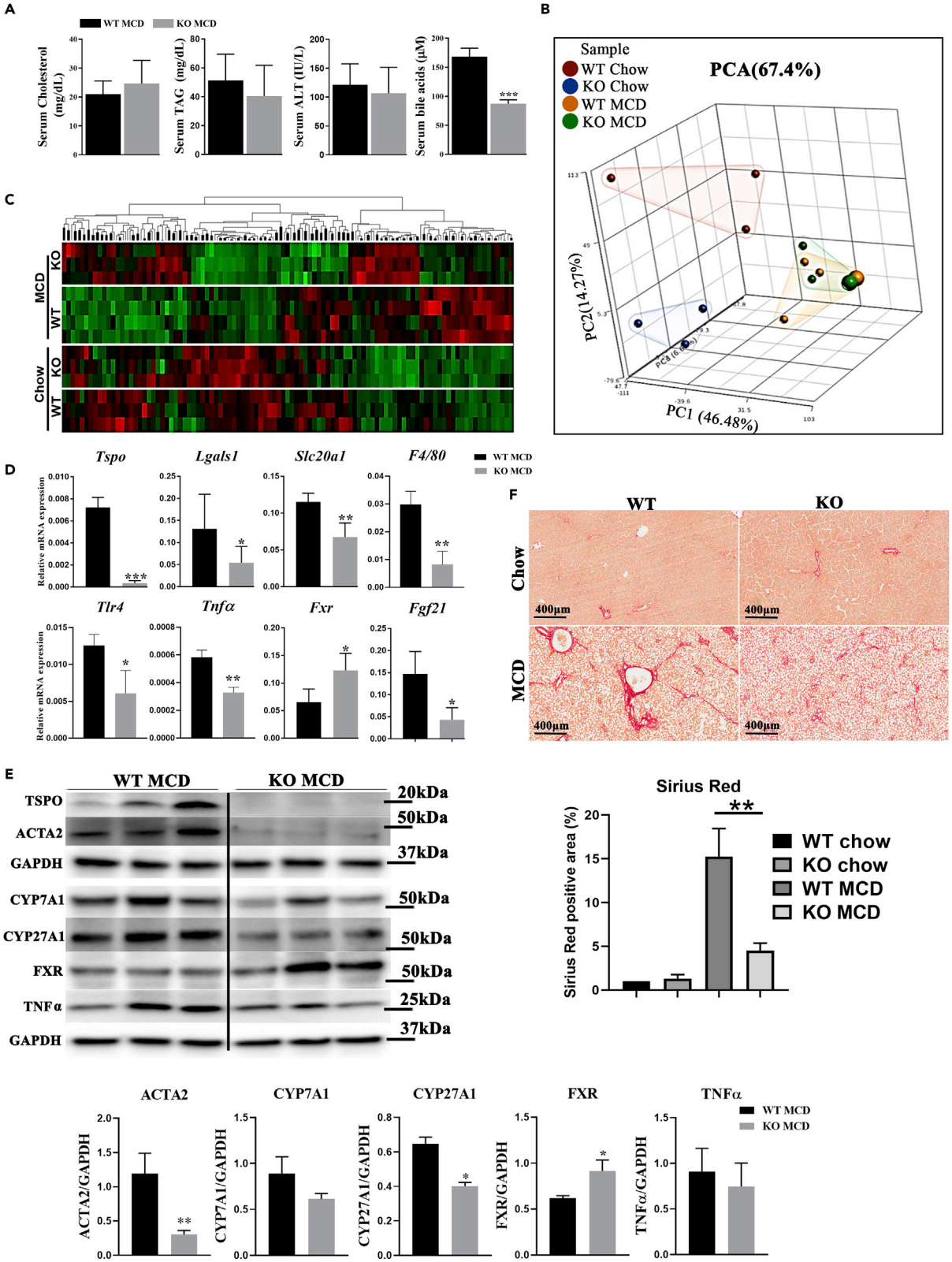
A
WT MCD
KO MCD
Serum Cholesterol (mg/dL)
Serum TAG (mg/dL)
Serum ALT (IU/L)
Serum bile acids (μM)
B
Sample
WT Chow
KO Chow
WT MCD
KO MCD
PCA(67.4%)
PC2(14.27%)
PC1 (46.48%)
C
MCD
KO
WT
Chow
KO
WT
D
Tspo
Lgals1
Slc20a1
F4/80
Tlr4
Tnfα
Fxr
Fgf21
Relative mRNA expression
WT MCD
KO MCD
F
WT
KO
Chow
MCD
400μm
E
WT MCD
KO MCD
TSPO
ACTA2
GAPDH
CYP7A1
CYP27A1
FXR
TNFα
GAPDH
20kDa
50kDa
37kDa
50kDa
50kDa
50kDa
25kDa
37kDa
Sirius Red
Sirius Red positive area (%)
WT chow
KO chow
WT MCD
KO MCD
ACTA2
CYP7A1
CYP27A1
FXR
TNFα
ACTA2/GAPDH
CYP7A1/GAPDH
CYP27A1/GAPDH
FXR/GAPDH
TNFα/GAPDH
WT MCD
KO MCD

CellPress
OPEN ACCESS

Figure 7. Loss of TSPO reduced serum BAs and inflammation and ameliorated liver fibrosis

(A) Serum test of cholesterol, triglyceride, ALT, and total BAs in WT and TSPO KO after MCD feeding.

(B) Schematic summary of PCA in WT and TSPO KO with chow or MCD feeding.

(C) Heatmap of cluster marker genes in WT and TSPO KO with chow or MCD feeding.

(D) qPCR data showing relative mRNA levels of *Tspo, Lgals1, Slc20a1, F4/80, Tlr4, Tnfa, Fxr,* and *Fgf21* versus *Rps18* in WT and TSPO KO after MCD feeding.

(E) Immunoblot showing TSPO, ACTA2, CYP71A, CYP27A1, FXR, and TNFα after MCD feeding between WT and TSPO KO. Immunoblots were quantified by ImageJ.

(F) Sirius red staining showing collagen fiber (red color) distribution between WT and TSPO KO after chow and MCD feeding. Quantification of Sirius red staining. Scale, 400 μM. Data are represented as mean ± SD, *$p < 0.05$, **$p < 0.01$, ***$p < 0.001$ by Student's t-test.

Moreover, we treated Huh7 cells with AcLDL+19-Atriol and found LC3-II substantially increased compared with Scram and AcLDL-treated cells (Figure 6E). Because AcLDL+19-Atriol led to FC accumulation (Figure 2G), this result may also suggest that FC accumulation derived from TSPO inhibition caused autophagy but need further investigation. Thus, we concluded that loss or inhibition of TSPO altered mitochondrial morphology and enhanced interactions between the ER and LDs. TC accumulation after loss of TSPO resulted in autophagy, and excessive FC accumulation led to more autophagolysosomes.

Loss of TSPO ameliorated liver fibrosis and inflammation in MCD-Induced NASH

To assess whether changes in TSPO expression regulated liver fibrogenesis, we fed WT and *Tspo* KO rats (Owen et al., 2017) an MCD diet for 2 months, which is enough to generate NASH associated with fibrosis. Serum analysis showed that the circulating cholesterol levels tended to increase, while serum alanine transaminase (ALT) was reduced in *Tspo* KO MCD as compared with WT MCD rats (Figure 7A). Bile acid (BA) levels were significantly reduced in *Tspo* KO MCD compared with WT MCD. To compare the transcriptome profiles between *Tspo* WT and KO rats after a chow diet or MCD, we performed RNA sequencing (RNA-seq) on samples from 4 groups: WT chow, *Tspo* KO chow, WT MCD, and *Tspo* KO MCD. Principal component analysis (PCA) highlighted the differences (Figure 7B). Hierarchical clustering analysis further confirmed that each group displayed a distinct gene expression pattern (Figure 7C). The transcriptome changes between these 4 groups were analyzed as scatterplots to display the changes (Figure S8). Ingenuity Pathway Analysis was performed to identify potential canonical pathways, diseases and functions, and gene networks associated with RNA-seq readouts, and the results are listed in Table S2. Comparisons of NASH markers *Col1a1 and Acta2* and markers for cholesterol metabolism *Cyp27a1, Cyp7a1,* and *Fgf21* between WT chow and WT MCD and between KO chow and KO MCD were analyzed (Figures S9A and S9B). *Tspo* levels were increased in MCD compared with a chow diet, suggesting *Tspo* expression paralleled liver fibrosis development (Figures S9C–S9E). qPCR and immunoblot analyses validated *Tspo* depletion in KO rats (Figures 7D and 7E). The inflammation markers *Lgals1, Tnfα, F4/80, Tlr4,* and *Slc20a1* (also known as *PiT1*) were decreased (Figure 7D), suggesting less inflammation in KO than WT after MCD. TNFα (Tumor necrosis factor alpha)was again shown downregulated in *Tspo* KO MCD compared with WT MCD by immunoblot analysis (Figure 7E). Farnesoid X receptor (*Fxr* or *Nr1h4*), a negative regulator of BA formation, was significantly increased in *Tspo* KO versus WT with MCD (Figure 7D), suggesting less BA synthesis in *Tspo* KO. Increased levels of FGF21 have been shown to correlate with NAFLD progression (Su et al., 2019), which was seen in WT MCD compared to WT chow (Figure 7D). Immunoblots also showed that actin alpha 2 (ACTA2) was decreased in *Tspo* KO versus WT with MCD. Responsible for BA synthesis, cholesterol 7 alpha-hydroxylase A1 (CYP7A1) showed a trend to decrease, while CYP27A1 significantly decreased in *Tspo* KO MCD as compared with WT MCD. However, FXR levels significantly increased in *Tspo* KO versus WT after MCD (Figure 7E), suggesting reduced BA production in *Tspo* KO rats compared to WT. Furthermore, Sirius red staining showed significantly reduced collagen fibers in *Tspo* KO in comparison to WT MCD rats (Figure 7F), indicating less fibrosis in KO MCD compared with WT MCD. Taken together, our results suggest that the loss of TSPO ameliorated liver fibrosis and inflammation through downregulation of BA synthesis.

DISCUSSION

Herein, we demonstrated several essential roles for TSPO in the progression of NAFLD. Loss of TSPO in hepatocytes triggers the onset of steatosis by TC, FC, and TAG accumulation. Mechanistically, TSPO physically interacts with ACAT2 at MAMs, and loss of TSPO inhibited ACAT2, resulting in FC accumulation in a manner independent of TC accumulation. Moreover, TSPO deficiency induced IRE1A and PERK/ATF4/CHOP pathways in ER stress and autophagy formation and FC accumulation aggravated these events. Meanwhile, TC and FC accumulation after the loss of TSPO led to LD enlargement. Mild TC accumulation after the loss of TSPO initially triggered a cell adaptation mechanism, but excessive FC accumulation caused the loss of this adaptive response. 19-Atriol can specifically block TSPO functions leading to FC accumulation, which phenocopies many biological events in ER stress, autophagy, and antioxidant

reaction. In the NASH model, the loss of TSPO ameliorated the liver fibrosis and inflammation by reducing BA production through upregulating FXR and downregulating CYP27A1 and CYP7A1. Collectively, our results suggest that TSPO plays an essential role in all stages of NAFLD progression. The loss of TSPO may initiate SS, but *in vivo* it also ameliorates liver fibrogenesis and inflammation, halting progression in NAFLD.

TSPO is ubiquitously expressed (Papadopoulos et al., 2006, 2018; Wyatt et al., 2012). In normal livers, TSPO expression is relatively low but becomes elevated upon liver injuries, such as those in response to carbon tetrachloride (CCl_4) or cycloheximide injection (Hatori et al., 2014, 2015; Xie et al., 2012). In this study, we confirmed that TSPO levels were indicative of the progression of NAFLD from patients and rodent samples.

To determine TSPO levels in different cell subtypes of the liver, we isolated hepatocytes, HSCs, and Kupffer cells from rats. *Tspo* mRNA is mainly found in HSCs and Kupffer cells and in low levels in hepatocytes (Figure S10). However, considering hepatocytes occupy more than 70% of the liver, we specifically investigated TSPO role in the hepatocyte cell line Huh7 cell and in primary mouse hepatocytes after lipid loading to mimic NAFLD.

Under chow diet feeding, we observed lipid accumulation in the TSPO KO rat liver by LDs staining and the TSPO KO mouse liver by MALDI IMS as compared with the controls. Thus, we specifically examined the role of TSPO in hepatocytes for SS progression because there is no (or less) activation of HSCs and Kupffer cells at this stage. Given the role of TSPO in binding and transporting cholesterol into mitochondria, we expected TC accumulation in the absence of TSPO. Surprisingly, we noticed FC elevation in TSPO-deficient cells compared with the control, even in the absence of AcLDL treatment. To gain further insight into the mechanism of FC accumulation in TSPO-deficient cells, we looked at levels of the convertases, CEH, and ACAT2, which ultimately determine the levels of free and esterified cholesterol in hepatocytes (Anderson et al., 1998; Chang et al., 1998; Parini et al., 2004). The loss of TSPO suppressed ACAT2 activity independent of cholesterol accumulation, implying that TSPO deficiency can induce FC accumulation by decreasing ACAT2 conversion of FC to CE. Furthermore, we performed Co-IP and PLA and revealed that the mitochondrial TSPO directly interacts with the ER ACAT2 independent of cholesterol accumulation. These findings provide evidence that the TSPO-ACAT2 interaction in MAMs may be a potential modulator for the TC and FC homeostasis and, furthermore, should have an impact on NAFLD progression.

An inhibitor of ACAT 58035 enhances FC accumulation after AcLDL treatment by blocking FC conversion to CE. However, we did not see a continuous increase in FC in response to AcLDL+58035 compared with AcLDL treatment in Huh7. Instead, both TC and FC content decreased in TSPO KD after AcLDL+58035 treatment compared with AcLDL, which might be due to the decreased cell viability in AcLDL+58035. However, in isolated mouse hepatocytes, TC and FC continuously increased after AcLDL or AcLDL+58035 treatment, which was more striking in TSPO KO cells compared with WT, implying that mouse primary hepatocytes are less susceptible to the impairment caused by FC accumulation than the human Huh7 cell line.

The catalase antioxidant system was triggered further after AcLDL treatment in mouse TSPO KO hepatocytes compared with DMSO, suggesting that the cells adapt to maintain cellular homeostasis in some extent. However, this adaptation was lost under additional stress as seen with FC accumulation after treatment with AcLDL+58035 in TSPO-deficient hepatocytes. Previous studies reported that β-oxidation, mitochondrial respiration, antioxidant reactions, and TCA cycle flux were induced in mouse models with nutritional overload, as well as in human subjects with obesity and SS (Iozzo et al., 2010; Koliaki et al., 2015; Miele et al., 2003; Patterson et al., 2016; Satapati et al., 2012; Sunny et al., 2011). ACOX1 is a rate-limiting enzyme in the peroxisomal β-oxidation pathway (Moreno-Fernandez et al., 2018), and PPARα regulates lipid transport and metabolism chiefly through the activation of the mitochondrial and peroxisomal fatty acid β-oxidation pathways (Tyagi et al., 2011). Mitochondrial fatty acid oxidation stimulation is enhanced upon the upregulation of ACOX1 and PPARα by a high-fat diet or the dysregulation of lipid metabolism (Eccleston et al., 2011; Sunny et al., 2011). We showed increased ACOX1 and PPARα levels in TSPO KO cells compared with controls after AcLDL treatment. However, this ratio did not increase more but rather decreased after AcLDL+58035 treatment compared with AcLDL. Taken all these observations into account, our results suggest that mild lipid accumulation primed antioxidant defense and free fatty acid oxidation, but excessive lipid overload is deleterious to these protective systems. Thus, FC accumulation resulting from a disturbed cholesterol balance in TSPO-deficient cells promotes the progression of SS to a later stage.

TSPO was identified as a novel element in the regulation of mitochondrial quality control by autophagy. Gatliff et al. demonstrated that this process depended upon the level of voltage-dependent anion channel

1 (VDAC1) expression; a higher TSPO/VDAC1 ratio leads to the reduction of the autophagic removal of mitochondria by limiting PINK1/PARK2-mediated mitochondrial ubiquitination via periorganelle accumulation of reactive oxygen species (ROS). On the other hand, a reduced TSPO/VDAC1 ratio leads to the induction of mitophagy (a specific autophagy with mitochondria) by reducing ROS production to promote PARK2-mediated ubiquitination of proteins and, thus, removal of dysfunctional mitochondria, allowing for the maintenance of cellular functions (Gatliff et al., 2014). Herein, we found that lipid accumulation (cholesterol and TAG) in TSPO-deficient cells promoted autophagy. In agreement with this, Kim et al. reported that ablation of TSPO in mouse hypothalamic glial cells elicited AMPK-dependent lipophagy (autophagic degradation of intracellular LDs), breaking down LDs into free fatty acids, thereby elevating ATP in a lipid stimulus (Kim et al., 2020). Whether there is an induction of lipophagy as a consequence of lipid accumulation in TSPO-deficient cells remains to be investigated.

BAs are the final steroid metabolites of cholesterol utilization in the liver (Hanukoglu, 1992). Many BAs are highly cytotoxic (Li and Apte, 2015), and therefore, BA synthesis is under tight regulatory control. In patients with NAFLD, BA homeostasis is disrupted and worsens with progression of the disease (Aranha et al., 2008). In contrast, stabilization of BA levels to normal significantly improved NALFD and type 2 diabetes mellitus (Huang et al., 2019). In our MCD NASH study, serum BA levels were suppressed in TSPO KO compared with WT rats. CYP7A1 and CYP27A1, a cholesterol 7α-hydroxylase responsible for the classic pathway and a steroid 27-hydroxylase responsible for the alternative pathway for BA synthesis, were both suppressed in the KO MCD liver compared with the WT MCD liver. The BA level was reduced by 66.7% and 73% in *Cyp7a1*$^{-/-}$ and *Cyp27a1*$^{-/-}$ mice and even more in double-knockout (*Cyp7a1*$^{-/-}$; *Cyp27a1*$^{-/-}$) mice (Rizzolo et al., 2019), indicative of the critical roles of these two hydroxylases in the BA metabolism. In addition, levels of FXR, a negative regulator of BA production and a BA receptor, were significantly increased in KO MCD rats compared with WT MCD. Recently, many emerging and promising therapies for NASH are designed as FXR agonists, for instance, LJN452 (Tropifexor, Novartis) (Tully et al., 2017), GS-9674 (Gilead) (Trauner et al., 2019), and Ocaliva (Intercept) (Samur et al., 2017). Ocaliva (obeticholic acid) is in phase III clinical trials for its ability to improve cholestasis liver disease and NASH by suppressing BA production in the liver, thus reducing the exposure of the liver to toxic levels of BAs (Donkers et al., 2019). Our data also showed that loss of TSPO ameliorated liver fibrosis through downregulation of BA synthesis by reducing CYP7A1 and CYP27A1 and increasing FXR expression, part of the same signaling pathway affected by Ocaliva. These data suggest that TSPO might be a potential therapeutic target for the suppression of NASH.

Despite the unequivocal evidence for the essential role of TSPO in NAFLD progression, several puzzling features remain. TSPO is a ubiquitous protein expressed in hepatocytes, HSCs, and Kupffer cells. Our study demonstrated that loss of TSPO in hepatocytes facilitated SS progression owing to FC and TAG accumulation. This model was simulated by the *in vitro* hepatocyte study in two aspects. First, in the SS stage, HSCs and Kupffer cells are not or less activated. Second, hepatocytes occupy most of liver parenchyma. However, it is still uncertain whether the results obtained from the hepatocyte studies depleted in TSPO can reflect the reality of SS in the liver. Therefore, to assess the liver phenotype in an SS animal model caused by high-fat diet feeding after depletion of TSPO to recapitulate the TSPO deficiency in hepatocytes is essential. In the MCD NASH model, the loss of TSPO function improved liver fibrogenesis by reducing BA formation. This discrepancy of the TSPO role between SS and NASH suggests distinct roles for TSPO dependent on liver cell type and stages of NAFLD. In the MCD NASH model, the reduced fibrosis and inflammation after the loss of TSPO is presumably mediated by TSPO deficiency in HSCs and Kupffer cells, but not hepatocytes. Thus, using HSCs or cocultures of hepatocytes and HSCs or Kupffer cells may be alternative strategies to tease out the cellular basis for TSPO effects in NASH.

Limitations of the study

Although the small cohort of patient samples used is a limitation in our study, the results obtained showed statistical significance between each stage of NAFLD. Moreover, the results obtained are in line with the observations made using labeled TSPO ligands to image TSPO expression in patients with NAFLD (Hatori et al., 2014; Xie et al., 2012). Thus, these human data provide the link between the published imaging studies and the animal models explored herein.

Resource availability

Lead contact

Further information and requests for resources and reagents should be directed to and will be fulfilled by the lead contact Vassilios Papadopoulos: Department of Pharmacology and Pharmaceutical Sciences, School of Pharmacy, University of Southern California, Los Angeles, CA 90089, USA; vpapadop@usc.edu.

Materials availability

This study did not generate new unique reagents.

Data and code availability

RNA-seq data were deposited in the Gene Expression Omnibus under accession number GSE138666. All data supporting the present study are available from the corresponding author on request.

METHODS

All methods can be found in the accompanying Transparent Methods supplemental file.

SUPPLEMENTAL INFORMATION

Supplemental information can be found online at https://doi.org/10.1016/j.isci.2021.102457.

ACKNOWLEDGMENTS

We thank Dr. Cheng Ji at USC (University of Southern California) for the stimulating discussions on cell stress and autophagy, Dr. Junji Watanabe (USC) for help with confocal microscopy and MALDI coordination, Mr. Anthony Rodriguez (USC) for technical assistance with transmission electron microscopy and the Liver Histology Core of the USC Research Center for Liver Diseases for histology services (NIH grant No. P30 DK048522). We also thank Ms. Melanie Galano for critical proofreading of the manuscript. This work was supported by grants from the Canadian Institutes of Health Research (MOP125983 and PJT148659), funds from the USC School of Pharmacy and the John Stauffer Dean's Chair in Pharmaceutical Sciences at USC, and the National Institutes of Health (R21AA027222).

AUTHOR CONTRIBUTIONS

Conceptualization, L.Y., and P.V.; Methodology, L.Y., W,J., S.C., and P.V.; Investigation, L.Y., C,L., L.L., S.C., P.S., L,A., M,P., W.H., W,J., S.C., G.S., C.G., and H.T.; Writing – Original Draft, L.Y., C.L., L.L., and P.V.; Writing –Review & Editing, L.Y., and P.V.; Funding Acquisition, P.V.; Resources, P.S., L,A., M,P., I,Y., S.T., G,L., and R.H.; Supervision, F,J., C.M., B,S., A,K., and P.V. All authors revised the article critically for important intellectual content. All authors have read and approved the final version of the manuscript.

DECLARATION OF INTERESTS

Dr. Yuji Ichida is an employee of PhoenixBio, Co., Ltd, Higashi-Hiroshima, Hiroshima, Japan; Dr. Cristina I. Silvescu is an employee of Bruker Daltonics, Billerica, MA 01821, USA; Dr. Jeremy J. Wolff was an employee of Bruker Daltonics, Billerica, MA 01821, USA, when this work was done.

Received: November 16, 2020
Revised: February 19, 2021
Accepted: April 19, 2021
Published: May 21, 2021

REFERENCES

Abd El-Kader, S.M., and El-Den Ashmawy, E.M. (2015). Non-alcoholic fatty liver disease: the diagnosis and management. World J. Hepatol. *7*, 846–858.

Anderson, R.A., Joyce, C., Davis, M., Reagan, J.W., Clark, M., Shelness, G.S., and Rudel, L.L. (1998). Identification of a form of acyl-CoA:cholesterol acyltransferase specific to liver and intestine in nonhuman primates. J. Biol. Chem. *273*, 26747–26754.

Aranha, M.M., Cortez-Pinto, H., Costa, A., da Silva, I.B., Camilo, M.E., de Moura, M.C., and Rodrigues, C.M. (2008). Bile acid levels are increased in the liver of patients with steatohepatitis. Eur. J. Gastroenterol. Hepatol. *20*, 519–525.

Benedict, M., and Zhang, X. (2017). Non-alcoholic fatty liver disease: an expanded review. World J. Hepatol. *9*, 715–732.

Bonamassa, B., and Moschetta, A. (2013). Atherosclerosis: lessons from LXR and the intestine. Trends Endocrinol. Metab. *24*, 120–128.

Brown, G.T., and Kleiner, D.E. (2016). Histopathology of nonalcoholic fatty liver disease and nonalcoholic steatohepatitis. Metabolism *65*, 1080–1086.

Chang, C.C., Lee, C.Y., Chang, E.T., Cruz, J.C., Levesque, M.C., and Chang, T.Y. (1998). Recombinant acyl-CoA:cholesterol acyltransferase-1 (ACAT-1) purified to essential homogeneity utilizes cholesterol in mixed micelles or in vesicles in a highly cooperative manner. J. Biol. Chem. *273*, 35132–35141.

Chung, J.Y., Chen, H., Midzak, A., Burnett, A.L., Papadopoulos, V., and Zirkin, B.R. (2013). Drug ligand-induced activation of translocator protein (TSPO) stimulates steroid production by aged brown Norway rat Leydig cells. Endocrinology *154*, 2156–2165.

D'Eletto, M., Rossin, F., Occhigrossi, L., Farrace, M.G., Faccenda, D., Desai, R., Marchi, S., Refolo, G., Falasca, L., Antonioli, M., et al. (2018). Transglutaminase type 2 regulates ER-mitochondria contact sites by interacting with GRP75. Cell Rep. *25*, 3573–3581 e3574.

Daniels, T.F., Killinger, K.M., Michal, J.J., Wright, R.W., Jr., and Jiang, Z. (2009). Lipoproteins,

cholesterol homeostasis and cardiac health. Int. J. Biol. Sci. *5*, 474–488.

Donkers, J.M., Roscam Abbing, R.L.P., and van de Graaf, S.F.J. (2019). Developments in bile salt based therapies: a critical overview. Biochem. Pharmacol. *161*, 1–13.

Eccleston, H.B., Andringa, K.K., Betancourt, A.M., King, A.L., Mantena, S.K., Swain, T.M., Tinsley, H.N., Nolte, R.N., Nagy, T.R., Abrams, G.A., et al. (2011). Chronic exposure to a high-fat diet induces hepatic steatosis, impairs nitric oxide bioavailability, and modifies the mitochondrial proteome in mice. Antioxid. Redox Signal. *15*, 447–459.

Fan, J., Campioli, E., Sottas, C., Zirkin, B., and Papadopoulos, V. (2020). Amhr2-Cre-Mediated global Tspo knockout. J. Endocr. Soc. *4*, bvaa001–029.

Farese, R.V., Jr., and Walther, T.C. (2009). Lipid droplets finally get a little R-E-S-P-E-C-T. Cell *139*, 855–860.

Fujii, H., Ikura, Y., Arimoto, J., Sugioka, K., Iezzoni, J.C., Park, S.H., Naruko, T., Itabe, H., Kawada, N., Caldwell, S.H., et al. (2009). Expression of perilipin and adipophilin in nonalcoholic fatty liver disease; relevance to oxidative injury and hepatocyte ballooning. J. Atheroscler. Thromb. *16*, 893–901.

Gatliff, J., East, D., Crosby, J., Abeti, R., Harvey, R., Craigen, W., Parker, P., and Campanella, M. (2014). TSPO interacts with VDAC1 and triggers a ROS-mediated inhibition of mitochondrial quality control. Autophagy *10*, 2279–2296.

Gluchowski, N.L., Becuwe, M., Walther, T.C., and Farese, R.V., Jr. (2017). Lipid droplets and liver disease: from basic biology to clinical implications. Nat. Rev. Gastroenterol. Hepatol. *14*, 343–355.

Hanukoglu, I. (1992). Steroidogenic enzymes: structure, function, and role in regulation of steroid hormone biosynthesis. J. Steroid Biochem. Mol. Biol. *43*, 779–804.

Hatori, A., Yui, J., Xie, L., Kumata, K., Yamasaki, T., Fujinaga, M., Wakizaka, H., Ogawa, M., Nengaki, N., Kawamura, K., et al. (2015). Utility of translocator protein (18 kDa) as a molecular imaging biomarker to monitor the progression of liver fibrosis. Sci. Rep. *5*, 17327.

Hatori, A., Yui, J., Xie, L., Yamasaki, T., Kumata, K., Fujinaga, M., Wakizaka, H., Ogawa, M., Nengaki, N., Kawamura, K., et al. (2014). Visualization of acute liver damage induced by cycloheximide in rats using PET with [(18)F]FEDAC, a radiotracer for translocator protein (18 kDa). PLoS One *9*, e86625.

Huang, H.H., Lee, W.J., Chen, S.C., Chen, T.F., Lee, S.D., and Chen, C.Y. (2019). Bile acid and fibroblast growth factor 19 regulation in obese diabetics, and non-alcoholic fatty liver disease after sleeve gastrectomy. J. Clin. Med. *8*, 815.

Huang, T.D., Behary, J., and Zekry, A. (2020). Non-alcoholic fatty liver disease: a review of epidemiology, risk factors, diagnosis and management. Intern. Med. J. *50*, 1038–1047.

Imai, Y., Varela, G.M., Jackson, M.B., Graham, M.J., Crooke, R.M., and Ahima, R.S. (2007). Reduction of hepatosteatosis and lipid levels by an adipose differentiation-related protein antisense oligonucleotide. Gastroenterology *132*, 1947–1954.

Iozzo, P., Bucci, M., Roivainen, A., Nagren, K., Jarvisalo, M.J., Kiss, J., Guiducci, L., Fielding, B., Naum, A.G., Borra, R., et al. (2010). Fatty acid metabolism in the liver, measured by positron emission tomography, is increased in obese individuals. Gastroenterology *139*, 846–856, 856 e841-846.

Kim, S., Kim, N., Park, S., Jeon, Y., Lee, J., Yoo, S.J., Lee, J.W., Moon, C., Yu, S.W., and Kim, E.K. (2020). Tanycytic TSPO inhibition induces lipophagy to regulate lipid metabolism and improve energy balance. Autophagy *16*, 1200–1220.

Kleiner, D.E., Brunt, E.M., Van Natta, M., Behling, C., Contos, M.J., Cummings, O.W., Ferrell, L.D., Liu, Y.C., Torbenson, M.S., Unalp-Arida, A., et al. (2005). Design and validation of a histological scoring system for nonalcoholic fatty liver disease. Hepatology *41*, 1313–1321.

Koliaki, C., Szendroedi, J., Kaul, K., Jelenik, T., Nowotny, P., Jankowiak, F., Herder, C., Carstensen, M., Krausch, M., Knoefel, W.T., et al. (2015). Adaptation of hepatic mitochondrial function in humans with non-alcoholic fatty liver is lost in steatohepatitis. Cell Metab. *21*, 739–746.

Lee, L., Alloosh, M., Saxena, R., Van Alstine, W., Watkins, B.A., Klaunig, J.E., Sturek, M., and Chalasani, N. (2009). Nutritional model of steatohepatitis and metabolic syndrome in the Ossabaw miniature swine. Hepatology *50*, 56–67.

Li, T., and Apte, U. (2015). Bile acid metabolism and signaling in cholestasis, inflammation, and cancer. Adv. Pharmacol. *74*, 263–302.

Makino, A., Hullin-Matsuda, F., Murate, M., Abe, M., Tomishige, N., Fukuda, M., Yamashita, S., Fujimoto, T., Vidal, H., Lagarde, M., et al. (2016). Acute accumulation of free cholesterol induces the degradation of perilipin 2 and Rab18-dependent fusion of ER and lipid droplets in cultured human hepatocytes. Mol. Biol. Cell *27*, 3293–3304.

Mardinoglu, A., Heiker, J.T., Gartner, D., Bjornson, E., Schon, M.R., Flehmig, G., Kloting, N., Krohn, K., Fasshauer, M., Stumvoll, M., et al. (2015). Extensive weight loss reveals distinct gene expression changes in human subcutaneous and visceral adipose tissue. Sci. Rep. *5*, 14841.

Matsuzawa, A. (2017). Thioredoxin and redox signaling: roles of the thioredoxin system in control of cell fate. Arch. Biochem. Biophys. *617*, 101–105.

Midzak, A., Akula, N., Lecanu, L., and Papadopoulos, V. (2011). Novel androstenetriol interacts with the mitochondrial translocator protein and controls steroidogenesis. J. Biol. Chem. *286*, 9875–9887.

Miele, L., Grieco, A., Armuzzi, A., Candelli, M., Forgione, A., Gasbarrini, A., and Gasbarrini, G. (2003). Hepatic mitochondrial beta-oxidation in patients with nonalcoholic steatohepatitis assessed by 13C-octanoate breath test. Am. J. Gastroenterol. *98*, 2335–2336.

Moreno-Fernandez, M.E., Giles, D.A., Stankiewicz, T.E., Sheridan, R., Karns, R., Cappelletti, M., Lampe, K., Mukherjee, R., Sina, C., Sallese, A., et al. (2018). Peroxisomal beta-oxidation regulates whole body metabolism, inflammatory vigor, and pathogenesis of nonalcoholic fatty liver disease. JCI Insight *3*, e93626.

Owen, D.R., Fan, J., Campioli, E., Venugopal, S., Midzak, A., Daly, E., Harlay, A., Issop, L., Libri, V., Kalogiannopoulou, D., et al. (2017). TSPO mutations in rats and a human polymorphism impair the rate of steroid synthesis. Biochem. J. *474*, 3985–3999.

Papadopoulos, V., Baraldi, M., Guilarte, T.R., Knudsen, T.B., Lacapere, J.J., Lindemann, P., Norenberg, M.D., Nutt, D., Weizman, A., Zhang, M.R., et al. (2006). Translocator protein (18kDa): new nomenclature for the peripheral-type benzodiazepine receptor based on its structure and molecular function. Trends Pharmacol. Sci. *27*, 402–409.

Papadopoulos, V., Fan, J., and Zirkin, B. (2018). Translocator protein (18 kDa): an update on its function in steroidogenesis. J. Neuroendocrinol. *30*, e12500.

Parini, P., Davis, M., Lada, A.T., Erickson, S.K., Wright, T.L., Gustafsson, U., Sahlin, S., Einarsson, C., Eriksson, M., Angelin, B., et al. (2004). ACAT2 is localized to hepatocytes and is the major cholesterol-esterifying enzyme in human liver. Circulation *110*, 2017–2023.

Patterson, R.E., Kalavalapalli, S., Williams, C.M., Nautiyal, M., Mathew, J.T., Martinez, J., Reinhard, M.K., McDougall, D.J., Rocca, J.R., Yost, R.A., et al. (2016). Lipotoxicity in steatohepatitis occurs despite an increase in tricarboxylic acid cycle activity. Am. J. Physiol. Endocrinol. Metab. *310*, E484–E494.

Plakkal Ayyappan, J., Paul, A., and Goo, Y.H. (2016). Lipid droplet-associated proteins in atherosclerosis (Review). Mol. Med. Rep. *13*, 4527–4534.

Puri, P., Baillie, R.A., Wiest, M.M., Mirshahi, F., Choudhury, J., Cheung, O., Sargeant, C., Contos, M.J., and Sanyal, A.J. (2007). A lipidomic analysis of nonalcoholic fatty liver disease. Hepatology *46*, 1081–1090.

Rizzolo, D., Buckley, K., Kong, B., Zhan, L., Shen, J., Stofan, M., Brinker, A., Goedken, M., Buckley, B., and Guo, G.L. (2019). Bile acid homeostasis in a cholesterol 7alpha-hydroxylase and sterol 27-hydroxylase double knockout mouse model. Hepatology *70*, 389–402.

Rizzuto, R., Pinton, P., Carrington, W., Fay, F.S., Fogarty, K.E., Lifshitz, L.M., Tuft, R.A., and Pozzan, T. (1998). Close contacts with the endoplasmic reticulum as determinants of mitochondrial Ca2+ responses. Science *280*, 1763–1766.

Samur, S., Klebanoff, M., Banken, R., Pratt, D.S., Chapman, R., Ollendorf, D.A., Loos, A.M., Corey, K., Hur, C., and Chhatwal, J. (2017). Long-term clinical impact and cost-effectiveness of obeticholic acid for the treatment of primary biliary cholangitis. Hepatology *65*, 920–928.

Sanjabi, B., Dashty, M., Ozcan, B., Akbarkhanzadeh, V., Rahimi, M., Vinciguerra, M., van Rooij, F., Al-Lahham, S., Sheedfar, F., van

Kooten, T.G., et al. (2015). Lipid droplets hypertrophy: a crucial determining factor in insulin regulation by adipocytes. Sci. Rep. *5*, 8816.

Satapati, S., Sunny, N.E., Kucejova, B., Fu, X., He, T.T., Mendez-Lucas, A., Shelton, J.M., Perales, J.C., Browning, J.D., and Burgess, S.C. (2012). Elevated TCA cycle function in the pathology of diet-induced hepatic insulin resistance and fatty liver. J. Lipid Res. *53*, 1080–1092.

Savino, S., Denora, N., Iacobazzi, R.M., Porcelli, L., Azzariti, A., Natile, G., and Margiotta, N. (2016). Synthesis, characterization, and cytotoxicity of the first oxaliplatin Pt(IV) derivative having a TSPO ligand in the axial position. Int. J. Mol. Sci. *17*, 1010.

Straub, B.K., Stoeffel, P., Heid, H., Zimbelmann, R., and Schirmacher, P. (2008). Differential pattern of lipid droplet-associated proteins and de novo perilipin expression in hepatocyte steatogenesis. Hepatology *47*, 1936–1946.

Su, X., Kong, Y., and Peng, D. (2019). Fibroblast growth factor 21 in lipid metabolism and non-alcoholic fatty liver disease. Clin. Chim. Acta *498*, 30–37.

Sunny, N.E., Parks, E.J., Browning, J.D., and Burgess, S.C. (2011). Excessive hepatic mitochondrial TCA cycle and gluconeogenesis in humans with nonalcoholic fatty liver disease. Cell Metab. *14*, 804–810.

Takahashi, Y., and Fukusato, T. (2014). Histopathology of nonalcoholic fatty liver disease/nonalcoholic steatohepatitis. World J. Gastroenterol. *20*, 15539–15548.

Tateno, C., Kawase, Y., Tobita, Y., Hamamura, S., Ohshita, H., Yokomichi, H., Sanada, H., Kakuni, M., Shiota, A., Kojima, Y., et al. (2015). Generation of novel chimeric mice with humanized livers by using hemizygous cDNA-uPA/SCID mice. PLoS One *10*, e0142145.

Teratani, T., Tomita, K., Suzuki, T., Furuhashi, H., Irie, R., Hida, S., Okada, Y., Kurihara, C., Ebinuma, H., Nakamoto, N., et al. (2017). Free cholesterol accumulation in liver sinusoidal endothelial cells exacerbates acetaminophen hepatotoxicity via TLR9 signaling. J. Hepatol. *67*, 780–790.

Tomita, K., Teratani, T., Suzuki, T., Shimizu, M., Sato, H., Narimatsu, K., Okada, Y., Kurihara, C., Irie, R., Yokoyama, H., et al. (2014). Free cholesterol accumulation in hepatic stellate cells: mechanism of liver fibrosis aggravation in nonalcoholic steatohepatitis in mice. Hepatology *59*, 154–169.

Tous, M., Ferre, N., Camps, J., Riu, F., and Joven, J. (2005). Feeding apolipoprotein E-knockout mice with cholesterol and fat enriched diets may be a model of non-alcoholic steatohepatitis. Mol. Cell. Biochem. *268*, 53–58.

Trauner, M., Gulamhusein, A., Hameed, B., Caldwell, S., Shiffman, M.L., Landis, C., Eksteen, B., Agarwal, K., Muir, A., Rushbrook, S., et al. (2019). The nonsteroidal farnesoid X receptor agonist cilofexor (GS-9674) improves markers of cholestasis and liver injury in patients with primary sclerosing cholangitis. Hepatology *70*, 788–801.

Tully, D.C., Rucker, P.V., Chianelli, D., Williams, J., Vidal, A., Alper, P.B., Mutnick, D., Bursulaya, B., Schmeits, J., Wu, X., et al. (2017). Discovery of tropifexor (LJN452), a highly potent non-bile acid FXR agonist for the treatment of cholestatic liver diseases and nonalcoholic steatohepatitis (NASH). J. Med. Chem. *60*, 9960–9973.

Tyagi, S., Gupta, P., Saini, A.S., Kaushal, C., and Sharma, S. (2011). The peroxisome proliferator-activated receptor: a family of nuclear receptors role in various diseases. J. Adv. Pharm. Technol. Res. *2*, 236–240.

Vance, J.E. (2014). MAM (mitochondria-associated membranes) in mammalian cells: lipids and beyond. Biochim. Biophys. Acta *1841*, 595–609.

Wang, X., Zheng, Z., Caviglia, J.M., Corey, K.E., Herfel, T.M., Cai, B., Masia, R., Chung, R.T., Lefkowitch, J.H., Schwabe, R.F., et al. (2016). Hepatocyte TAZ/WWTR1 promotes inflammation and fibrosis in nonalcoholic steatohepatitis. Cell Metab. *24*, 848–862.

Wyatt, S.K., Manning, H.C., Bai, M., Ehtesham, M., Mapara, K.Y., Thompson, R.C., and Bornhop, D.J. (2012). Preclinical molecular imaging of the translocator protein (TSPO) in a metastases model based on breast cancer xenografts propagated in the murine brain. Curr. Mol. Med. *12*, 458–466.

Xie, L., Yui, J., Hatori, A., Yamasaki, T., Kumata, K., Wakizaka, H., Yoshida, Y., Fujinaga, M., Kawamura, K., and Zhang, M.R. (2012). Translocator protein (18 kDa), a potential molecular imaging biomarker for non-invasively distinguishing non-alcoholic fatty liver disease. J. Hepatol. *57*, 1076–1082.

Yamasaki, C., Ishida, Y., Yanagi, A., Yoshizane, Y., Kojima, Y., Ogawa, Y., Kageyama, Y., Iwasaki, Y., Ishida, S., Chayama, K., et al. (2020). Culture density contributes to hepatic functions of fresh human hepatocytes isolated from chimeric mice with humanized livers: novel, long-term, functional two-dimensional in vitro tool for developing new drugs. PLoS One *15*, e0237809.

Zhou, Z., Torres, M., Sha, H., Halbrook, C.J., Van den Bergh, F., Reinert, R.B., Yamada, T., Wang, S., Luo, Y., Hunter, A.H., et al. (2020). Endoplasmic reticulum-associated degradation regulates mitochondrial dynamics in brown adipocytes. Science *368*, 54–60.

iScience, Volume *24*

Supplemental information

Cholesterol-binding translocator protein TSPO regulates steatosis and bile acid synthesis in nonalcoholic fatty liver disease

Yuchang Li, Liting Chen, Lu Li, Chantal Sottas, Stephanie K. Petrillo, Anthoula Lazaris, Peter Metrakos, Hangyu Wu, Yuji Ishida, Takeshi Saito, Lucy Golden-Mason, Hugo R. Rosen, Jeremy J. Wolff, Cristina I. Silvescu, Samuel Garza, Garett Cheung, Tiffany Huang, Jinjiang Fan, Martine Culty, Bangyan Stiles, Kinji Asahina, and Vassilios Papadopoulos

Figure S1

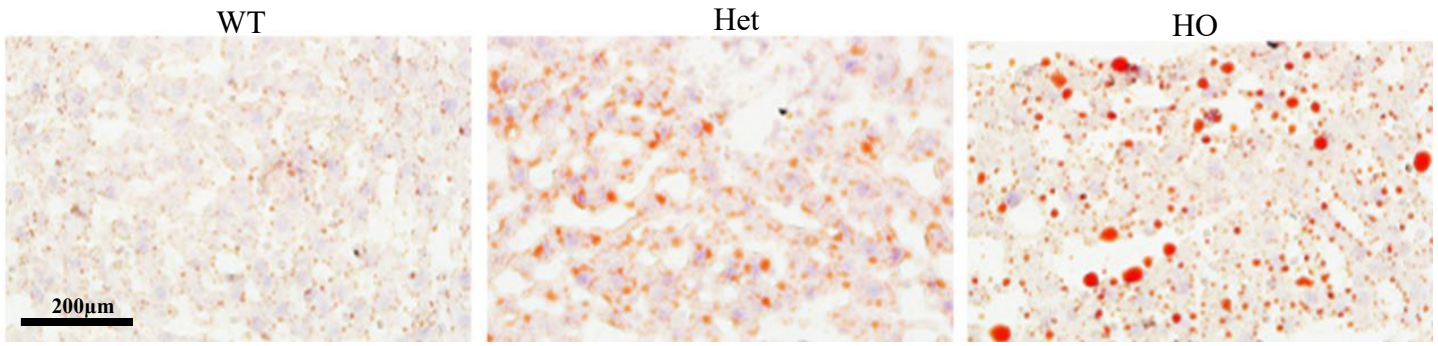

Figure S2

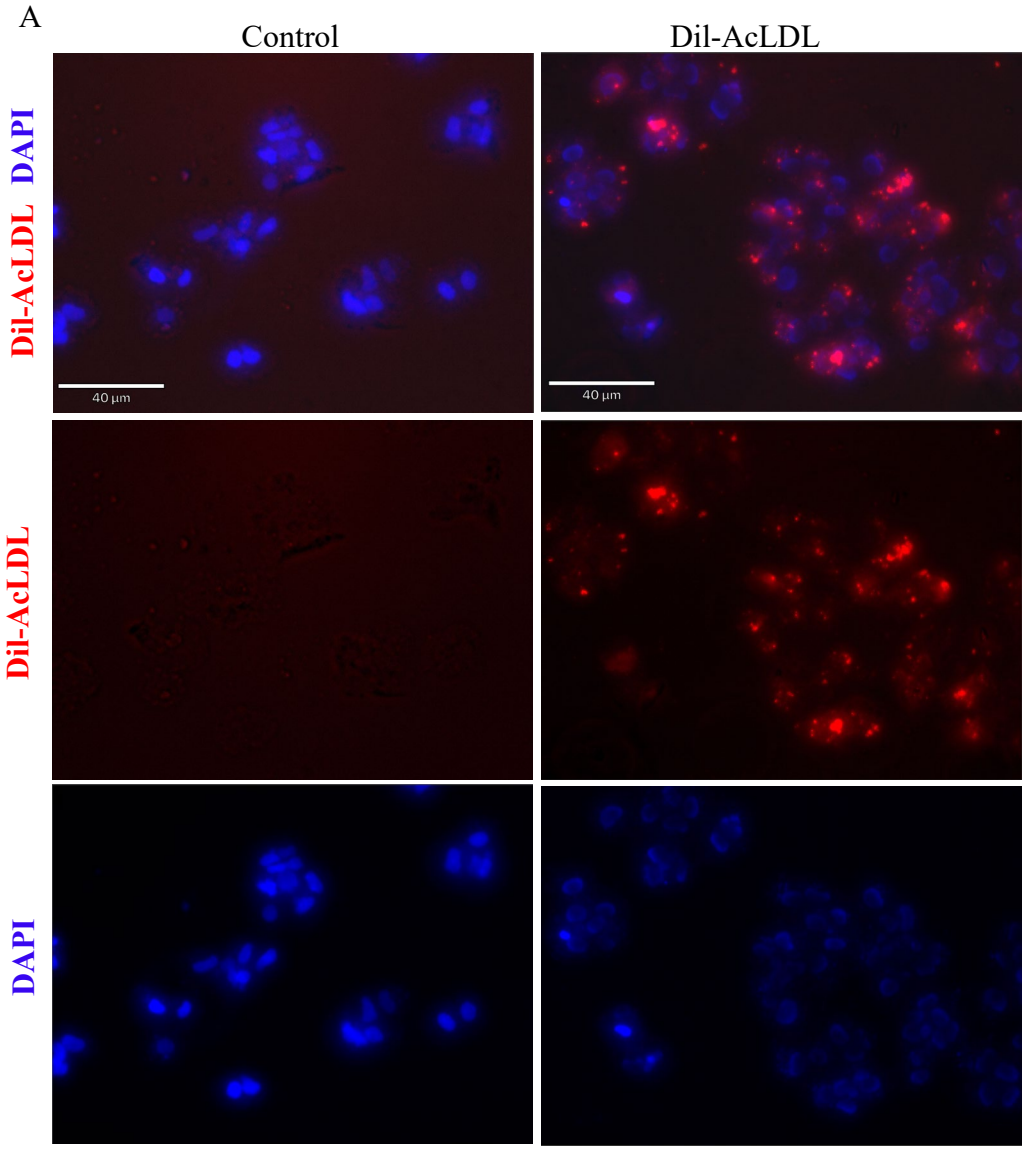
A
Control
Dil-AcLDL
DAPI
Dil-AcLDL
40 μm
40 μm
Dil-AcLDL
DAPI

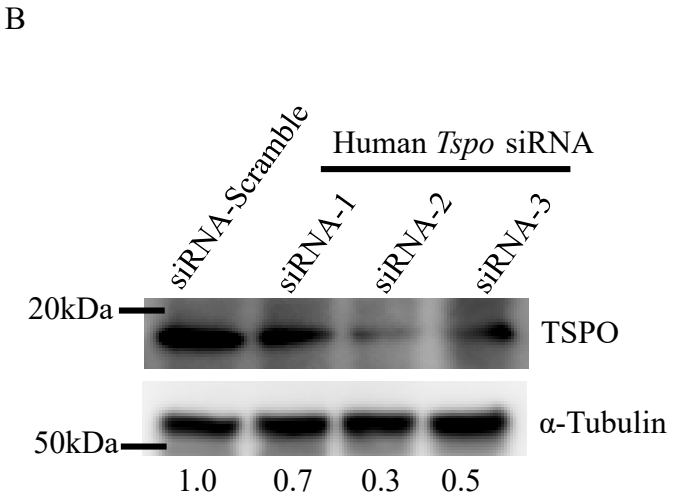
B
Human *Tspo* siRNA
siRNA-Scramble
siRNA-1
siRNA-2
siRNA-3
20kDa
TSPO
50kDa
α-Tubulin
1.0
0.7
0.3
0.5

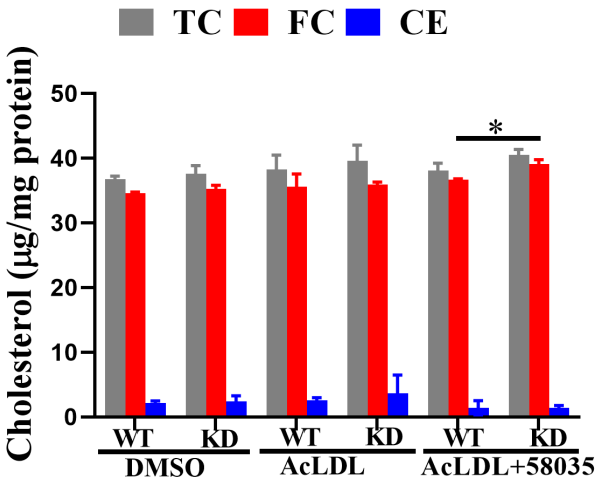
C
TC
FC
CE
Cholesterol (μg/mg protein)
50
40
30
20
10
0
*
WT
KD
WT
KD
WT
KD
DMSO
AcLDL
AcLDL+58035

Figure S3

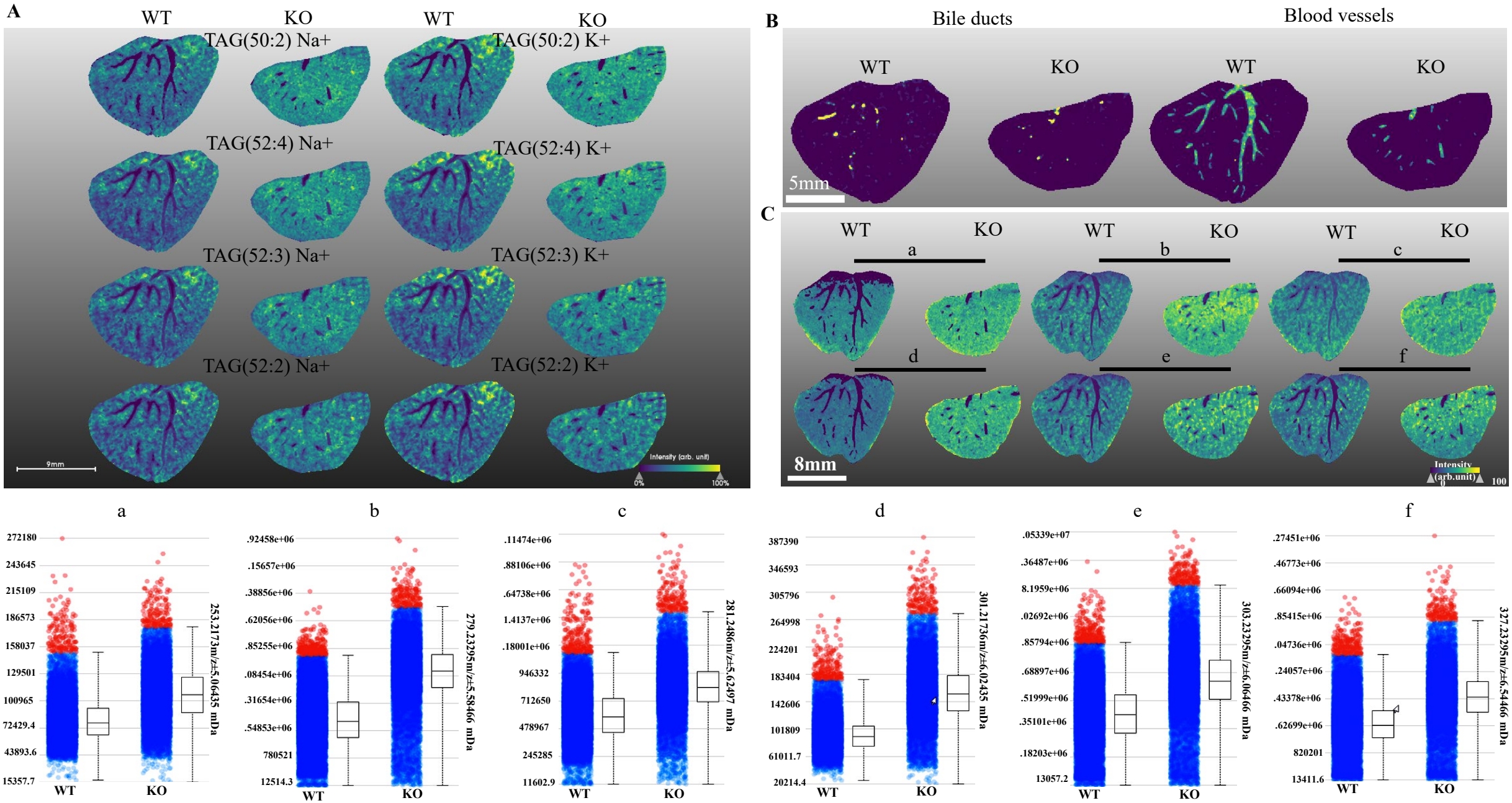
A
WT
KO
WT
KO
TAG(50:2) Na+
TAG(50:2) K+
TAG(52:4) Na+
TAG(52:4) K+
TAG(52:3) Na+
TAG(52:3) K+
TAG(52:2) Na+
TAG(52:2) K+
9mm
Intensity (arb. unit)
0%
100%
B
Bile ducts
Blood vessels
WT
KO
WT
KO
5mm
C
WT
KO
WT
KO
WT
KO
a
b
c
d
e
f
8mm
Intensity (arb.unit)
0
100
a
272180
243645
215109
186573
158037
129501
100965
72429.4
43893.6
15357.7
WT
KO
253.2173m/z±5.06435 mDa
b
.92458e+06
.15657e+06
.38856e+06
.62056e+06
.85255e+06
.08454e+06
.31654e+06
.54853e+06
780521
12514.3
WT
KO
279.23295m/z±5.58466 mDa
c
.11474e+06
.88106e+06
.64738e+06
1.4137e+06
.18001e+06
946332
712650
478967
245285
11602.9
WT
KO
281.2486m/z±5.62497 mDa
d
387390
346593
305796
264998
224201
183404
142606
101809
61011.7
20214.4
WT
KO
301.21736m/z±6.02435 mDa
e
.05339e+07
.36487e+06
8.1959e+06
.02692e+06
.85794e+06
.68897e+06
.51999e+06
.35101e+06
.18203e+06
13057.2
WT
KO
303.23295m/z±6.06466 mDa
f
.27451e+06
.46773e+06
.66094e+06
.85415e+06
.04736e+06
.24057e+06
.43378e+06
.62699e+06
820201
13411.6
WT
KO
327.23295m/z±6.54466 mDa

Figure S4

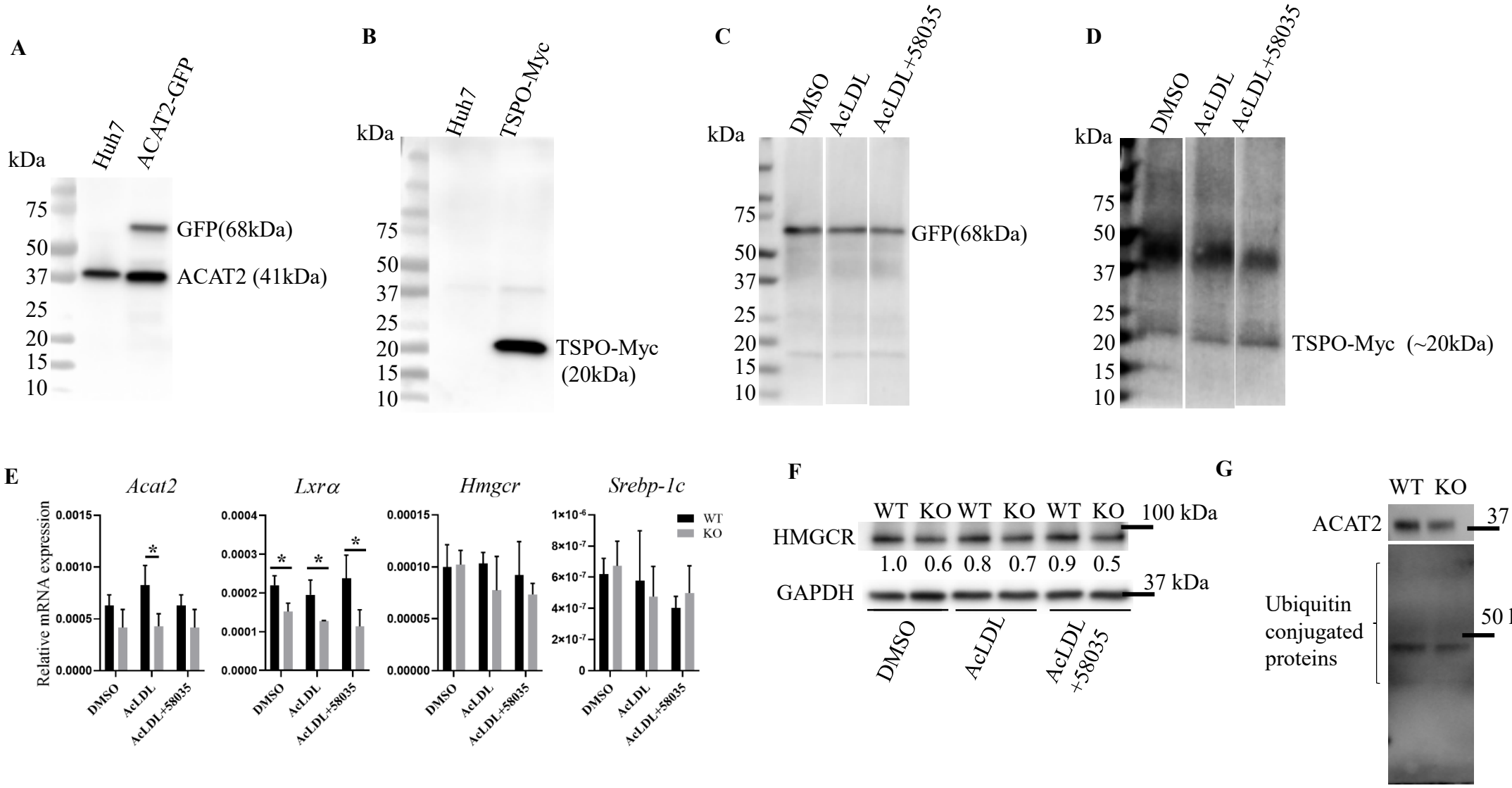
A
Huh7
ACAT2-GFP
kDa
75
50
37
25
20
15
10
GFP(68kDa)
ACAT2 (41kDa)
B
Huh7
TSPO-Myc
kDa
TSPO-Myc
(20kDa)
C
DMSO
AcLDL
AcLDL+58035
kDa
GFP(68kDa)
D
DMSO
AcLDL
AcLDL+58035
kDa
TSPO-Myc (~20kDa)
E
Acat2
Lxrα
Hmgcr
Srebp-1c
Relative mRNA expression
WT
KO
DMSO
AcLDL
AcLDL+58035
F
WT KO WT KO WT KO
100 kDa
HMGCR
1.0 0.6 0.8 0.7 0.9 0.5
37 kDa
GAPDH
DMSO
AcLDL
AcLDL +58035
G
WT KO
ACAT2
37 kDa
Ubiquitin conjugated proteins
50 kDa

Figure S5

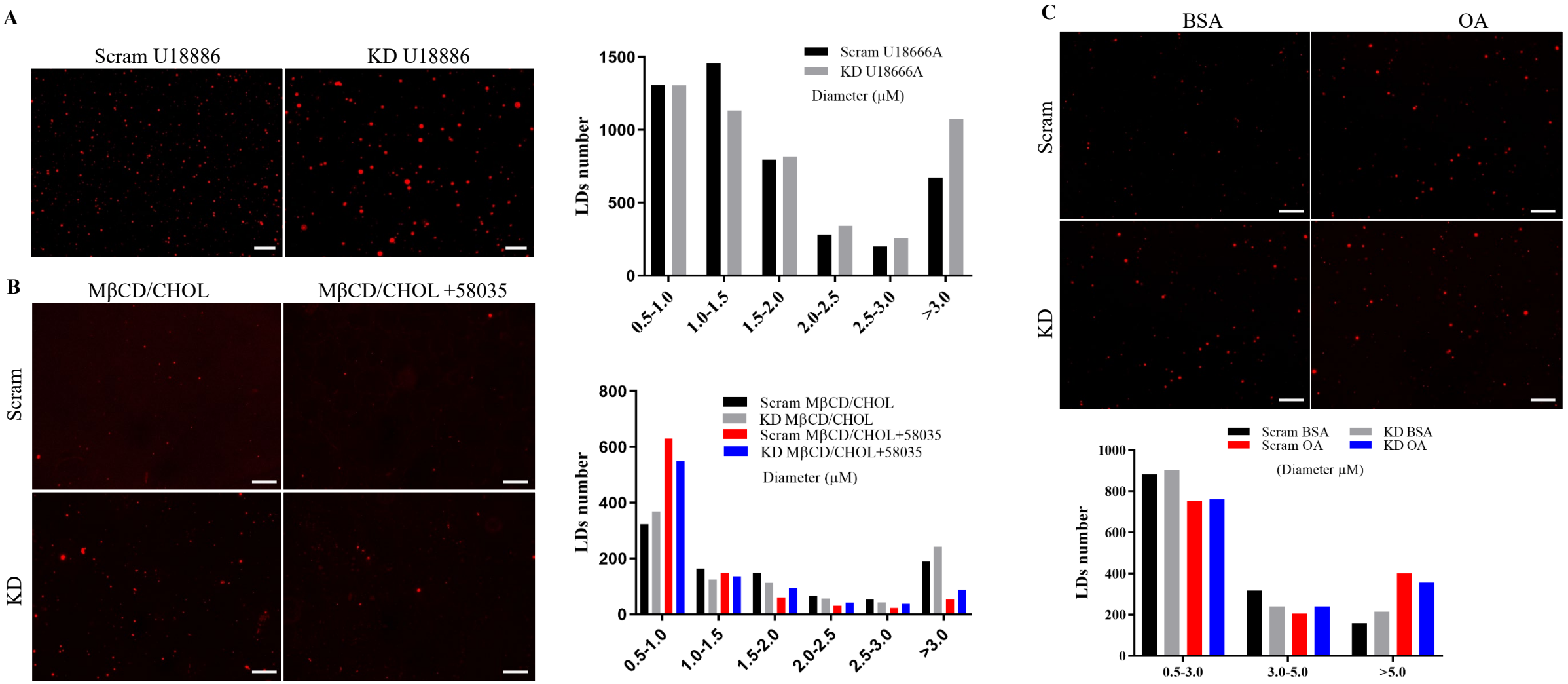
A
Scram U18886
KD U18886
Scram U18666A
KD U18666A
Diameter (μM)
LDs number
1500
1000
500
0
0.5-1.0
1.0-1.5
1.5-2.0
2.0-2.5
2.5-3.0
>3.0
B
MβCD/CHOL
MβCD/CHOL +58035
Scram
KD
Scram MβCD/CHOL
KD MβCD/CHOL
Scram MβCD/CHOL+58035
KD MβCD/CHOL+58035
Diameter (μM)
LDs number
800
600
400
200
0
0.5-1.0
1.0-1.5
1.5-2.0
2.0-2.5
2.5-3.0
>3.0
C
BSA
OA
Scram
KD
Scram BSA
Scram OA
KD BSA
KD OA
(Diameter μM)
LDs number
1000
800
600
400
200
0
0.5-3.0
3.0-5.0
>5.0

Figure S6

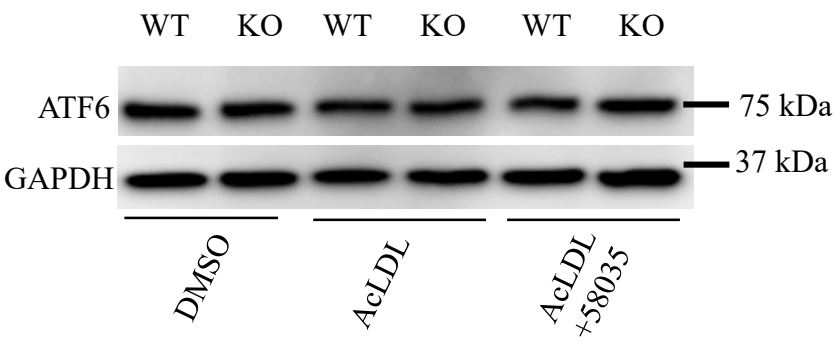
WT
KO
WT
KO
WT
KO
ATF6
GAPDH
75 kDa
37 kDa
DMSO
AcLDL
AcLDL
+58035

Figure S7

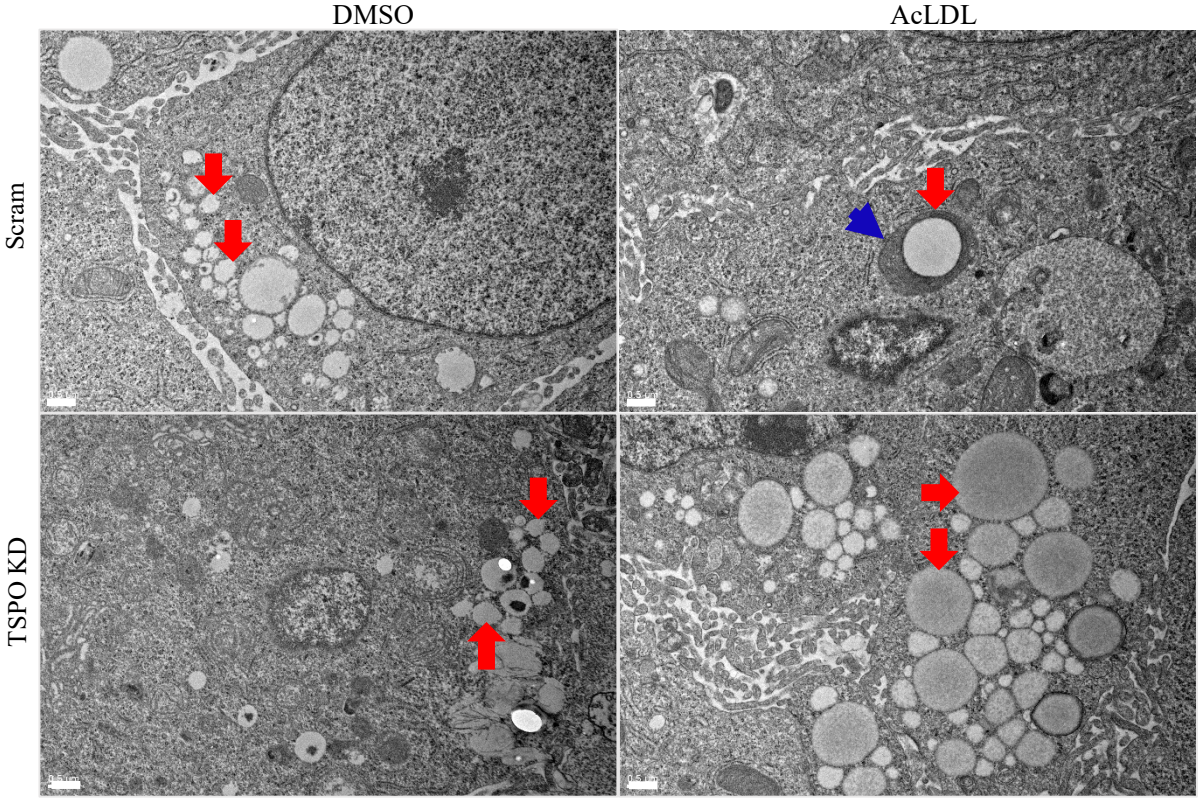

Figure S8

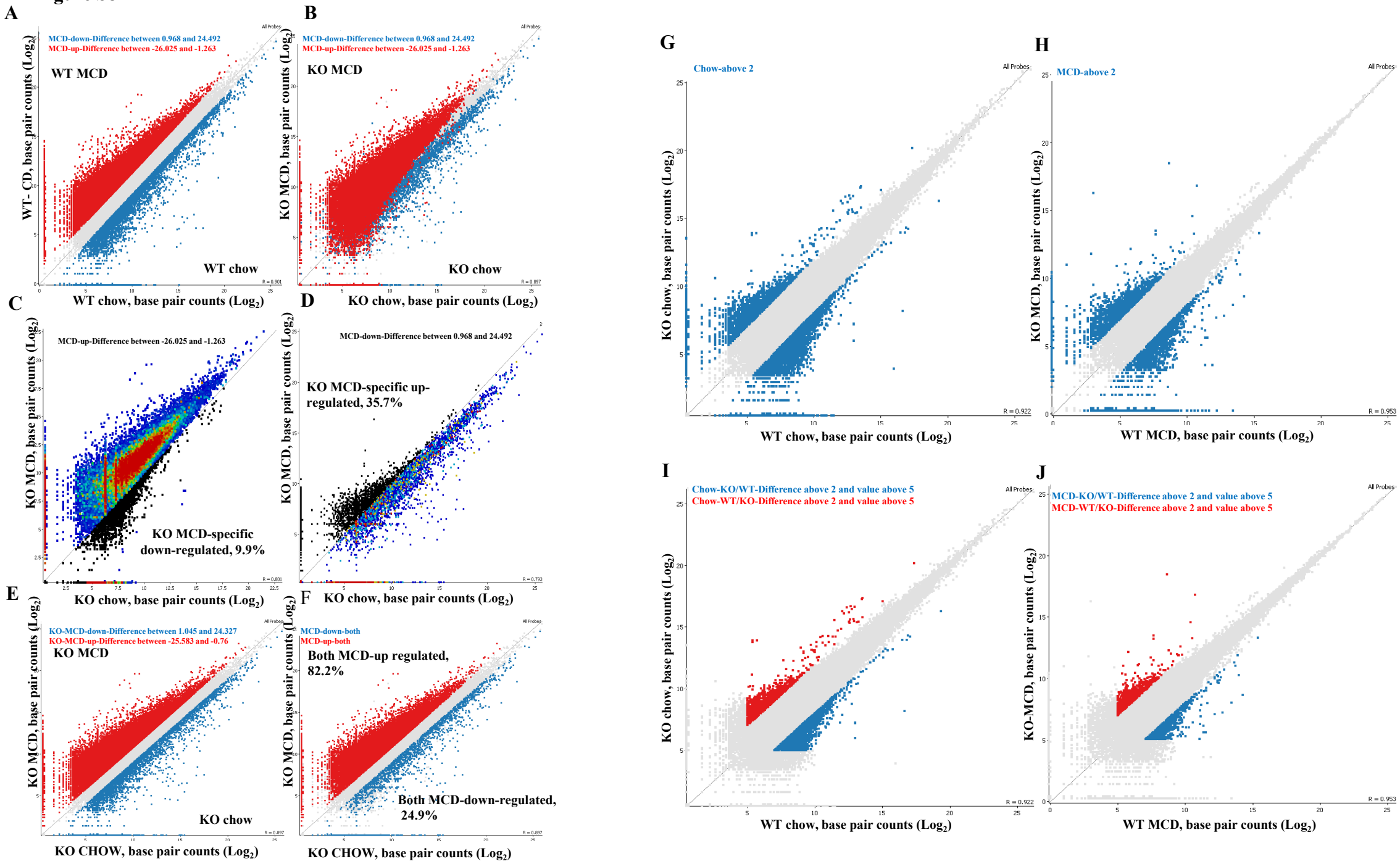
A
MCD-down-Difference between 0.968 and 24.492
MCD-up-Difference between -26.025 and -1.263
WT MCD
WT chow
WT- CD, base pair counts (Log2)
WT chow, base pair counts (Log2)
B
MCD-down-Difference between 0.968 and 24.492
MCD-up-Difference between -26.025 and -1.263
KO MCD
KO chow
KO MCD, base pair counts (Log2)
KO chow, base pair counts (Log2)
C
MCD-up-Difference between -26.025 and -1.263
KO MCD-specific down-regulated, 9.9%
KO MCD, base pair counts (Log2)
KO chow, base pair counts (Log2)
D
MCD-down-Difference between 0.968 and 24.492
KO MCD-specific up-regulated, 35.7%
KO MCD, base pair counts (Log2)
KO chow, base pair counts (Log2)
E
KO-MCD-down-Difference between 1.045 and 24.327
KO-MCD-up-Difference between -25.583 and -0.76
KO MCD
KO chow
KO MCD, base pair counts (Log2)
KO CHOW, base pair counts (Log2)
F
MCD-down-both
MCD-up-both
Both MCD-up regulated, 82.2%
Both MCD-down-regulated, 24.9%
KO MCD, base pair counts (Log2)
KO CHOW, base pair counts (Log2)
G
Chow-above 2
KO chow, base pair counts (Log2)
WT chow, base pair counts (Log2)
H
MCD-above 2
KO MCD, base pair counts (Log2)
WT MCD, base pair counts (Log2)
I
Chow-KO/WT-Difference above 2 and value above 5
Chow-WT/KO-Difference above 2 and value above 5
KO chow, base pair counts (Log2)
WT chow, base pair counts (Log2)
J
MCD-KO/WT-Difference above 2 and value above 5
MCD-WT/KO-Difference above 2 and value above 5
KO-MCD, base pair counts (Log2)
WT MCD, base pair counts (Log2)

Figure S9

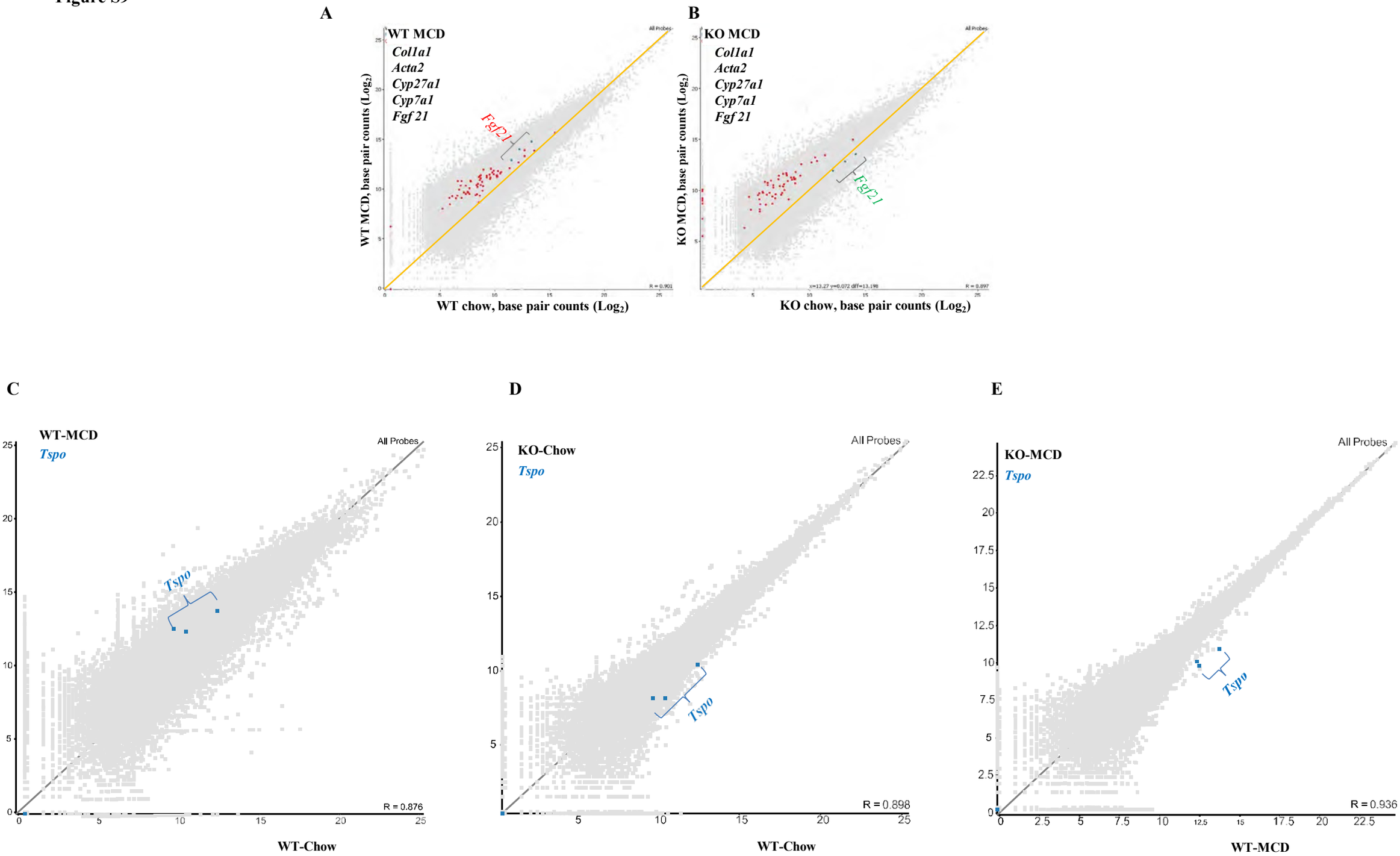
A
WT MCD
Col1a1
Acta2
Cyp27a1
Cyp7a1
Fgf 21
Fgf21
WT MCD, base pair counts (Log2)
WT chow, base pair counts (Log2)
B
KO MCD
Col1a1
Acta2
Cyp27a1
Cyp7a1
Fgf 21
Fgf21
KO MCD, base pair counts (Log2)
KO chow, base pair counts (Log2)
C
WT-MCD
Tspo
All Probes
R = 0.876
WT-Chow
D
KO-Chow
Tspo
All Probes
R = 0.898
WT-Chow
E
KO-MCD
Tspo
All Probes
R = 0.936
WT-MCD

Figure S10

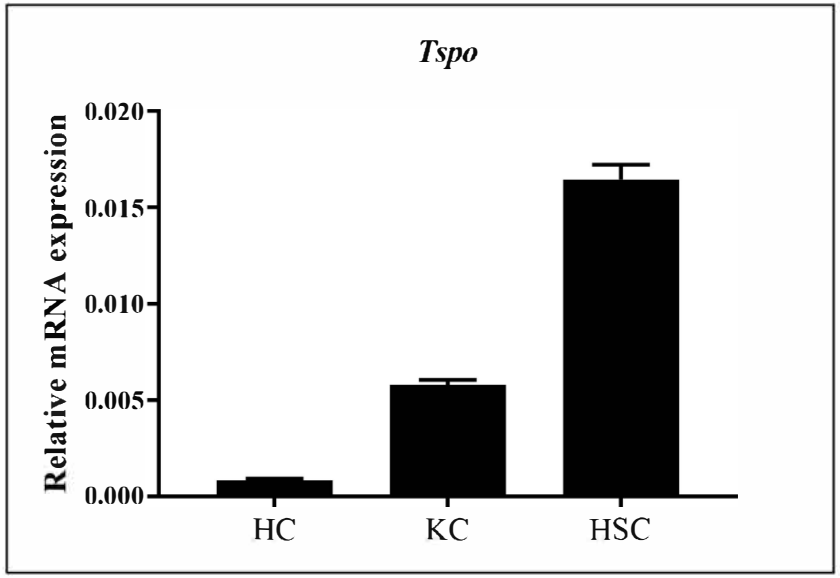
Tspo
Relative mRNA expression
0.020
0.015
0.010
0.005
0.000
HC
KC
HSC

Figure S11

A TSPO conserved peptide

Mus musculus	WRDNHGWRGGRRLPE
Mus Pahari	WRDNSGRRGGSRLPE
Human	WRDNSGRRGGSRLAE
Rat	WRDNSGRRGGSRLTE
	* * * * * * * * ** *

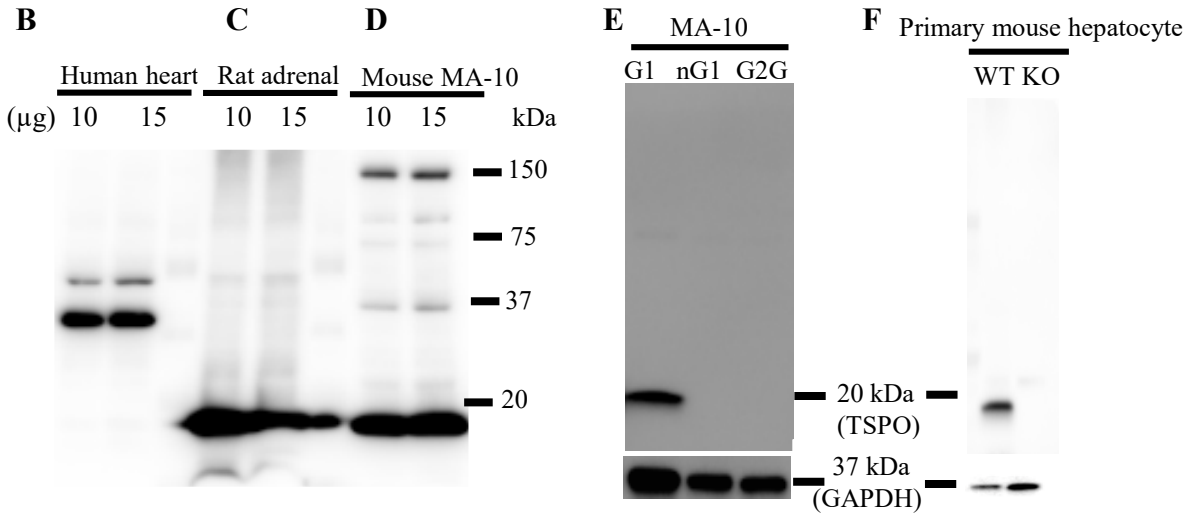

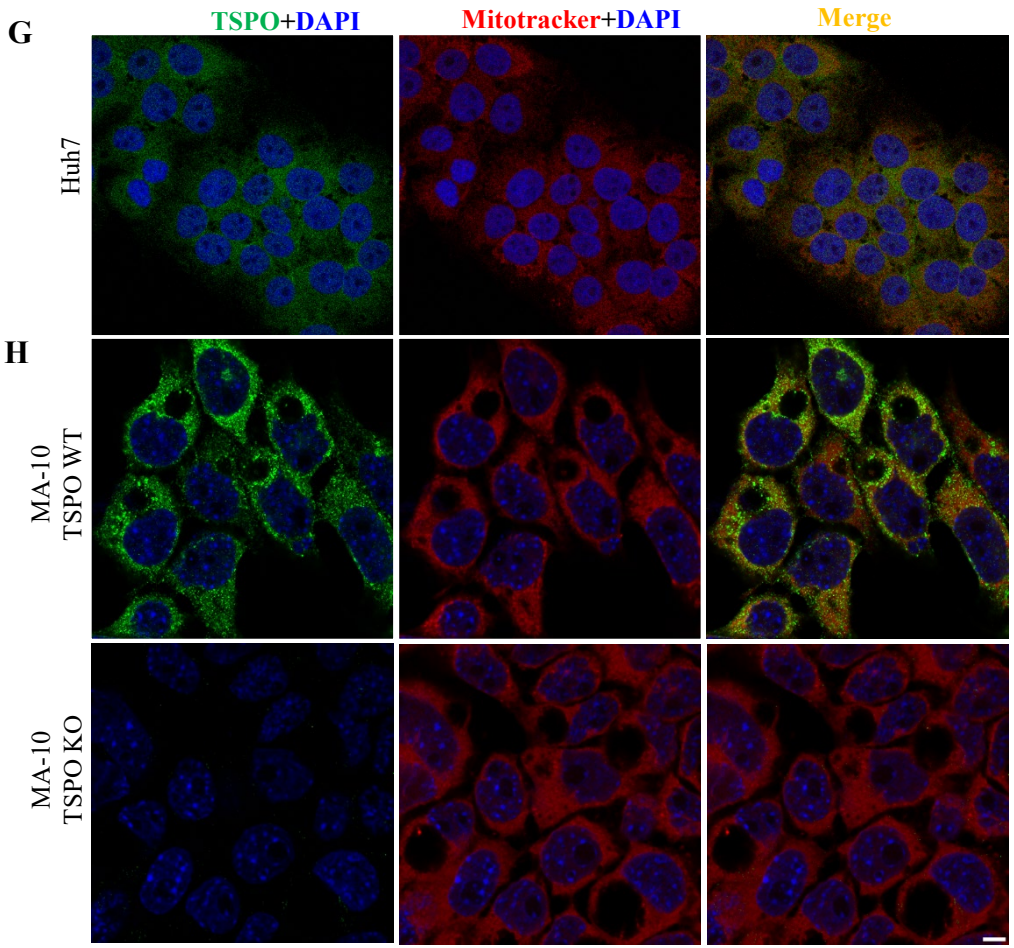

Supplemental Figure Legends

Figure S1. Related to Figure 2. The TSPO HO rats with abnormal LD accumulation displayed a steatosis phenotype. The rat liver cryosections of TSPO WT, heterozygous deletion (Het), and homozygous deletion (HO, in main text as KO) was stained with Oil Red O (red color). The results show abnormal LD (Lipid droplet) accumulation, one hallmark of steatosis, in *Tspo* HO rats compared to WT and Het. Scale, 200μm.

Figure S2. Related to Figure 2. Free cholesterol elevation in TSPO-deficient cells. (A) Dil-AcLDL uptake in Huh7 cells. Huh7 cells were treated with Dil-AcLDL (50μg/mL) (red color) for 24hrs, the cells were fixed in 4%PFA for 10min. After PBS washing 3 times, the cells nuclear was stained with DAPI. The images were captured under an inverted microscope. (a): Huh7 cells were treated with DMSO as control. (b): Huh7 cells were treated with Dil-AcLDL. Scale bar, 40μm. (B) TSPO was knocked out (KD) using different human *Tspo* siRNAs (siRNA-1, -2 and -3) in humanized mouse hepatocytes, α-Tubulin was used as the loading control. (C) Total cholesterol (TC), free cholesterol (FC) and cholesterol ester (CE) were measured in primary WT and TSPO KD (*Tspo* siRNA 2) humanized mouse hepatocytes. Data are represented as mean ± SD, *$p<0.05$, **$p<0.01$ by one-way ANOVA.

Figure S3. Related to Figure 2. Triglycerides and fatty acids distribution in WT and TSPO KO mouse liver. (A) Triglycerides (yellow) are observed both as Na^+ and K^+ cations, with similar distributions for both ions in TAG (50:2), (52:4), (52:3) and (52:2). The blue indicating blood vessels. Scale, 9mm. (B) For bile ducts, taurocholic acid was observed as an [M-H+2K] + ion. For blood vessels, heme is observed as [M+] ions. In general, the TAGs were not strongly localized with either the bile ducts or blood vessels. Bile ducts: yellow. Blood vessel: blue. Scale bar, 5mm. (C) Fatty acids (yellow) were analyzed using negative ion mode with 9-AA matrix. A few of the fatty acids were observed in WT and KO tissues, with fatty acids generally being more abundant in KO tissue. Similar to the triglycerides, the fatty acids were not localized near the blood vessels (blue), but in general were fairly evenly distributed around a liver. The plots for each of the observed fatty acids showed similar trends. Specifically, elevated levels of all the observed fatty acids were observed in the KO liver compared to WT liver. a, palmitoleic/sapienic acid; b, linoleic/linoelaidic acid; c, oleic/elaidic/vaccenic acid; d, eicosapentaenoic acid; e, arachidonic acid; f, docosahexaenoic acid. Scale, 8mm. Data represented as mean ± SD.

Figure S4. Related to Figure 3. TSPO directly interacts with ACAT2 in a manner independent of cholesterol accumulation. After co-transfection of TSPO-myc plasmid and ACAT2-Turbo-GFP plasmid into WT Huh7 cells, we validated the overexpression of ACAT2 with ACAT2 antibody (A) and TSPO with C-Myc antibody (B), respectively. After incubation of the anti-Turbo-GFP antibodies with clarified cell lysates, immunoblotting by Turbo-GFP (control, C) and C-Myc antibody, the results showed 18-20 kDa of TSPO band (D). The cells were treated with AcLDL or AcLDL+58035 and immunoprecipitated with GFP antibody, the results showed TSPO and ACAT2 interacted in a manner independent of cholesterol accumulation (C, D). QPCR of *Acta2, Lxra, Hmgcr* and *Srebp-1c* in primary WT and TSPO KO hepatocytes with DMSO, AcLDL and AcLDL+58035 treatment (E). Data are represented as mean ± SD, *$p<0.05$ by Student's t-test. HMGCR immunoblot in WT and TSPO KO primary mouse hepatocytes with DMSO, AcLDL and AcLDL+58035 treatment (F). Immunoprecipitation with ACAT2 antibody and immunoblot with ubiquitin in WT and TSPO KO mouse hepatocytes (G).

Figure S5. Related to Figure 4. Lipid droplet frequency distribution after treatment with U18666A, MβCD/CHOL, MβCD/CHOL+58035 or oleic acid in Huh7. (A) LDs distribution (size, number) in Scram and TSPO KD Huh7 cells after U18666A treatment for 24hrs. LDs were isolated, stained with nile red, imaged (left panel) and quantified (right panel). (B) LDs distribution (size, number) in Scram and TSPO KD Huh7 cells after MβCD/CHOL or MβCD/CHOL+58035 treatment for 24hrs. The LDs were isolated, stained with nile red, imaged (left panel) and quantified (right panel). CHOL: cholesterol. (C) LDs distribution (size, number) in Scram and TSPO KD Huh7 cells after treatment with BSA or oleic acid (OA) for 24hrs. The LDs were isolated, stained with nile red, imaged (left panel) and quantified (right panel). Scale, 50μm.

Figure S6. Related to Figure 5. No change of ATF6 between WT and TSPO KO. ATF6 immunoblot in WT and TSPO KO primary mouse hepatocytes with DMSO, AcLDL and AcLDL+58035 treatment.

Figure S7. Related to Figure 6. The LD size in Scram and TSPO KD Huh7 cells after treatment with AcLDL. The Scram and TSPO KD cells were treated with DMSO and AcLDL for 24hr and then observed under TEM. Compared to Scram, the LD diameters in TSPO KD cells were enlarged with AcLDL treatment. LD, red arrow; ER, blue arrow. Scale, 500 nm.

Figure S8. Related to Figure 7. MCD diet mediated transcriptome changes in reflection in TSPO KO rats. (A) The scatterplot of RNA-seq gene expression analysis between WT chow vs. WT MCD. MCD diet mediated transcript expression data farthest away from the diagonal line were selected for further analysis. (B) The selected data points from A were overlaid on the RNA-seq transcript expression data from TSPO KO rats: KO chow vs. KO MCD. Apparently, the MCD diet-related genes were affected by TSPO KO. (C) The up-regulated MCD-mediated genes from WT are overlaid on RNA-seq transcript expression data from TSPO KO rats. Some TSPO KO specific down-regulated genes are selected (in dark), accounting for 9.9 % of the total MCD diet up-regulated genes. (D) The down-regulated MCD-mediated genes from WT were overlaid on RNA-seq transcript expression data from TSPO KO rats. Some TSPO KO specific up-regulated genes are selected (in dark), accounting of 35.7% of the total up-regulated genes by MCD diet. (E) The scatterplot of RNA-seq gene expression analysis between TSPO KO chow vs. KO MCD. The MCD diet-mediated transcript expression data farthest away from the diagonal line were selected for further comparison. (F) The MCD diet-mediated gene expression from TSPO KO rats were laid over the WT rats. Both TSPO KO vs WT shared 82.2% genes that were up-regulated and 24.9% of genes that were down-regulated. (G, H) The selected genes with over 2-fold difference between KO vs WT (chow) and KO vs WT (MCD). (I, J) The selected genes with over 5-fold difference between KO vs WT (chow) and KO vs WT (MCD).

Figure S9. Related to Figure 7. The comparisons of NASH markers (*Col1a1, Acta2*) and cholesterol metabolism markers (*Cyp27a1, Cyp7a1, Fgf21* and *Tspo*) between WT chow/WT MCD and KO chow/KO MCD rats. (A) The NASH markers *Col1a1, Acta2* and cholesterol metabolism markers of *Cyp27a1, Cyp7a1,* and *Fgf21* mediated by MCD diet are up regulated in the WT MCD rats. (B) The same markers are shown in the TSPO KO rats. Remarkably, the *Fgf21* was down-regulated in TSPO KO MCD but up-regulated in KO chow. (C) *Tspo* was up regulated after MCD diet than in Chow diet. (D) *Tspo* was higher in WT-Chow than in KO-Chow. (E) *Tspo* was higher in WT-MCD than in KO-MCD.

Figure S10. Related to Figure 2. TSPO mainly expressed in the primary HSCs. Hepatocyte (HC), Kupffer cells (KC) and Hepatic stellate cells (HSC) was isolated from rat and the real-time PCR was performed. mRNA relative expression is *Tspo/Gapdh*.

Figure S11. Related to Figure 1 and 7. Characterization of the generated TSPO polyclonal antibody in rabbit. (A) Comparison of conserved peptide sequence in different species. Western blots of TSPO in (B)human heart lysate, (C) rat adrenal lysate, (D) mouse tumor Leydig cell line MA-10, and (E) mouse MA-10 (G1) and two MA-10 TSPO knockout (nG1 and G2G) cell lines, and (F) in primary hepatocytes from TSPO wild type and TSPO KO mouse. GAPDH was used as an internal control. (G) Co-staining of TSPO (green) and Mitotracker (Mit) (red) in WT human Huh7 cells. (H) Co-staining of TSPO (green) and Mit (red) in mouse TSPO WT MA-10 and TSPO KO MA-10 cells. Nuclear is stained by DAPI. Scale, 20μm.

Transparent Methods

EXPERIMENTAL MODEL AND SUBJECT DETAILS

Standard Protocol Approvals and Patient Consent

The NAFLD patient study was done in accordance with the guidelines approved by McGill University Health Centre Institutional Review Board (IRB). Prior written informed consent was obtained from all subjects who participated in the study (protocol: SDR-11-669).

Experimental Animals

TSPO KO mice were generated in our laboratory (Fan et al., 2020). *Tspo* mutant rats (Het and KO) were generated using CompoZr® knockout Zinc Finger Nuclease Technology to delete an 89-bp fragment flanking the exon 3/intron 3 junction in *Tspo* gene (Owen et al., 2017). The mice or rats were bred and maintained in accordance with protocols approved by the IACUC of the University of Southern California.

For the NAFLD model, seven-week-old male C57BL/6J mice (Jackson Labs) were allowed to acclimate housing in our facility for 2 weeks before dietary intervention. Mice were fed a diet to induce NASH with the fructose-palmitate-cholesterol diet (FPC, Tekland) incorporating 1.25% cholesterol for 20 weeks (n=12). The drinking water was supplemented with 23.1g/L of glucose and 18.9 g/L fructose (55%/45% glucose/fructose ratio). Age-matched mice maintained on chow or FPC diet incorporating 0.05% cholesterol served as normal (n=6) and steatosis (n=12), respectively.

For MCD (methionine choline deficient) diet studies, TSPO WT and KO male rats aged 12 wks old were fed either regular rat chow or an MCD diet (MP Biomedicals, #960439; n = 4) for 8 wks. The rats were divided into 4 groups (WT chow, KO chow, WT MCD and KO MCD, n=4). The body weight was recorded every week. After 2 mo, deeply anesthetized rats were decapitated and trunk blood was collected into tubes (BD Vacutainer, 367820), or into a microcontainer (BD Microtainer Blood Collection Tubes, 365965) followed by 10 min centrifugation at 1200×g. The serum was collected from BD Vacutainer for bile acid analysis, the plasma was collected from BD Microtainer Blood Collection Tubes for albumin, alanine aminotransferase (ALT), aspartate aminotransferase (AST), Alkaline Phosphatase, glucose, total bilirubin, total cholesterol, and triacylglycerol measurement (Antech Diagnostics, CA, USA). Fresh liver tissue samples from WT chow, KO chow, WT MCD and KO MCD were placed into micro-Eppendorf tubes and stored in -80ºC for protein and RNA analyses. The left lobe from the livers from the above 4 groups were sliced with a scalpel approximately 0.5 cm in maximal dimension and fixed in 4% phosphate-buffered paraformaldehyde for 2h.

Cell culture

Human liver Huh7 cells (originally isolated from a liver tumor from a 57-year-old Japanese male) were purchased from JCRB Cell Bank. Cells, both non-transfected and transfected (see below), were grown in DMEM (Dulbecco's modified Eagle medium) supplemented with 10% heat-inactivated fetal bovine serum (Hi-FBS) and 1% penicillin-streptomycin. Cells were kept at 37ºC in a humidified incubator with an atmosphere of 5% CO2.

To observe AcLDL uptake, Huh7 cells at 80% confluence were treated with Low Density Lipoprotein from Human Plasma, Acetylated, DiI complex (DiI AcLDL) (50µg/mL) for 24 hrs.,

and cells were then fixed in 4% PFA for 10 min. Cells were washed 3 times with PBS, and nuclei were stained with DAPI. The images were captured with an inverted fluorescent microscope (REVOLVE, Echo, USA). For cholesterol accumulation, stable cell lines of Scram Huh7 and TSPO KD Huh7 cells were seeded until confluence reached approximately 80% and then treated with DMSO, AcLDL (Thermo Fisher Scientific, #J65029-8+, 50 μg/mL) or AcLDL and compound 58035 (Sigma, #S9318, 10 μg/mL) for 24 hrs. For the TSPO CRAC inhibitor experiment, 80% confluence Huh7 cells were treated with DMSO, AcLDL (50 μg/mL) or AcLDL (50 μg/mL) +5-Androsten-3, 17, 19-triol (19-Atriol) (100 μM) for 24 hrs., and the cells were then collected for TC and FC measurements. For cholesterol depletion using methyl-β-cyclodextrin (MβCD), KD and Scram cells were seeded in human Lipoprotein Deficient Serum (LPDS; LP4, Sigma). After treatment for 24 hrs., cells were harvested for isolation of lipid droplets with the Lipid Droplet Isolation Kit (Cell Biolabs, Inc. MET-5011). For the accumulation of free fatty acids, KD and Scram cells were treated with either 5% bovine serum albumin (BSA; fatty acid-free, endotoxin-free; IC15240105, Sigma) or 400 μM OA (O3008, Sigma) for 24 hrs. Cells were harvested for isolation of lipid droplets with the Lipid Droplet Isolation Kit (Cell Biolabs, Inc. MET-5011). For OA treatment, KD and Scram cells were treated with either 5% bovine serum albumin (BSA; fatty acid-free, endotoxin-free) or 400 μM OA for 24 hrs.

Primary mouse hepatocytes were isolated from a 8-week-old wild type male C57BL/6 and a TSPO global knock out (KO) male mouse using a two-step collagenase perfusion protocol through the portal vein (Severgnini et al., 2012). Perfusions yielded 80% initial cell viability by trypan blue exclusion and a final 93% viability following Percoll gradient centrifugation. The hepatocytes were seeded at 1×10^6/ml in basic medium containing insulin (1 μg/ml), hydrocortisone (0.25 μM) for 4 hrs or until cells were fully attached to the collagen I (Gibco, USA) coated wells, then the medium was replaced with 10% Hi-FBS DMEM. After incubation overnight, the cells were treated as noted above for cell lines.

Primary rat hepatocytes were isolated from an 8-week-old male Sprague Dawley. The isolation is as the same as described above for mouse hepatocytes. The male rat HSCs (hepatic stellate cells) and KCs (Kupffer cells) were isolated by gradient ultracentrifugation of a non-parenchymal cell-enriched fraction following pronase-collagenase digestion of the liver by the Southern California Research Center for ALPD and Cirrhosis (Li et al., 2016; Xiong et al., 2008). Cell viability was ascertained by trypan blue dye exclusion and for both HSCs and KCs was about 95%.

Human hepatocytes were isolated from humanized liver chimeric mice (HLCM). In brief, HLCM were produced by an injection of commercially available cryopreserved primary human hepatocytes (PHH) (Lot: JFC, 1-year old, Caucasian male, BioIVT Westbury, NY) into the spleen of severe combined immunodeficiency (SCID) mice with albumin enhancer/promoter driven cDNA-urokinase type plasminogen activator (cDNA-uPA) transgene expression (Tateno et al., 2015). The use of PHH for the production of HLCM has been approved by Utilization of Human Tissue Ethical Committee of PhoenixBio Co., Ltd. (0031). After 13-27 weeks post PHH injection, HLCM with high replacement rates (>90%, estimated by blood human albumin levels which is highly correlated with histological replacement index (Sugahara et al., 2020) were subjected to human hepatocyte isolation. Human hepatocytes were isolated by a two-step collagenase perfusion method as described previously (Yamasaki et al., 2020).

See results for which cell lines or isolated cells were used in any one experiment done with the methods detailed below. The methods did not change between cell lines or isolated cells except as noted.

METHOD DETAILS

Clinical Data

This study included a total of 12 liver specimens from 12 patients undergoing liver resection for different etiologies. Following sharp resection of a small liver specimen, samples were immediately perfused with ice-cold normal saline solution. After gross examination by a pathologist, samples were released. All samples were scored by a pathologist according to the NAFLD Activity Score (NAS) (Kleiner et al., 2005): normal livers (n=3), livers with steatosis (n=3), non-alcoholic steatohepatitis (NASH) (n=3) and cirrhosis (n=3) **(Table S1)**.

Immunohistochemical (IHC) Staining of Human Samples

Formalin-fixed, paraffin-embedded (FFPE) human CRCLM resected blocks were used for this study. Serial sections 4 µm thick were cut from each FFPE block, mounted on charged glass slides (Superfrost Plus; Fisher Scientific, Waltham, MA), and baked at 65°C for 1hr prior to staining. IHC staining was performed using the Ventana BenchMark LT fully automated machine (Ventana Medical System Inc. Arizona, USA) and stained for TSPO (1:2000; Monoclonal rabbit Anti-Human PBR, Abcam cat. No ab109497) using extended antigen retrieval (CC1 buffer). Antibodies see **Table S5.**

Histopathological Analysis and Scoring of Human Samples

All human patients' slides were scanned at 40X magnification using the Aperio AT Turbo system. Images were viewed using the Aperio ImageScope ver.11.2.0.780 software program for scoring analysis and assessment of signals. The positivity was assessed with an Aperio ScanScope (Aperio Technologies Inc., Vista, CA), ImageScope software, and an optimized algorithm (positive pixel count V9, Aperio, Inc.).

Histology Slides Preparation and Picro-Sirius Red Staining of Rat MCD Fed Samples

PFA fixed liver tissues were dehydrated by sequentially increasing ethanol concentrations, cleared in xylene, and then embedded in paraffin wax. The liver collagen after MCD feeding was visualized with Picro-Sirius Red Stain Kit (American MasterTech, Pint Kit Item: KTPSRPT). Briefly, the paraffin slides were deparaffinized with xylene, rehydrated in gradient concentration of alcohol (100%, 95%, 70%, 50%) and rinsed with deionized H_2O. The slides were immersed in Picro-Sirius red stain solution for 1min following by a 0.5% acetic acid rinse. After dehydration in absolute alcohol. The slides were cleared in xylene and mounted with permanent mounting media. The images were captured with an inverted microscope (REVOLVE, Echo, USA). The collagen density was quantified using Image J software.

Generation of Stable TSPO KD Cell Line in Huh7

Huh7 cells were transfected with human PBR (TSPO) shRNA plasmid (Cat#: sc-40821-SH, Santa Cruz) or Scramble shRNA plasmid-A (Scram) (Cat#: sc-108060, Santa Cruz) using Lipofectamine 3000 Transfection Reagent (Thermo Fisher Scientific, Cat# L3000001). After 2 days of transfection, the cells were selected with puromycin (1 mg/ml) for two weeks. The cells were then

harvested and subjected to immunoblotting and confocal detection to confirm knockdown before use. The resulting cell lines were TSPO KD and Scram.

siRNA transfection

Human hepatocytes were transfected with human TSPO siRNA (Millipore Sigma, NM_000714: SASI_Hs01_00054085 for siRNA-1; SASI_Hs01_00054086 for siRNA-2 and SASI_Hs01_00054085 for siRNA-3, Millipore Sigma) and negative control siRNA (SIC001-5X1NMOL, Millipore Sigma) following the instructions of Lipofectamine™ RNAiMAX Transfection Reagent (Invitrogen, Cat# 13778150). The transfection efficiency was determined by immunoblot against rabbit TSPO antibody. After comparison, TSPO siRNA-2 was chosen for later experiments.

Matrix-assisted Laser Desorption/ionization (MALDI) Imaging Mass Spectrometry (IMS)

WT and TSPO KO mice 3 months old males were harvested, and the left liver lobe dissected and immediately placed on an aluminum boat floating on liquid nitrogen for 3-5 minutes. The frozen tissue was stored in -80°C for later use or immediately mounted onto a specimen disc using OCT as a mounting glue for cryostat sectioning (thickness 10 µm). The tissue sections were placed onto a Bruker ITO-coated slide (Bruker, Cat# # 237001). Slides were kept frozen at -80C until shipped on dry ice to Bruker Scientific LLC (Billerica, MA, USA). TC, CE, fatty acids, and triglycerides were examined in positive ion mode. The images were generated with SCiLS software.

Quantitative Real-time PCR (qPCR)

Total RNA was extracted from cells or tissues using Quick-RNA™ MiniPrep (#R1054&1055, Zymo Research, USA). Reverse-transcription was performed using a PrimeScript RT reagent kit (#RR037A, Takara, USA). qPCR was amplified with SYBR Green Real-Time PCR Master Mixes (#A25742, Thermo Fisher Scientific, USA) and performed on Real-Time PCR Instruments (CFX384, BIO-RAD, USA). The oligonucleotides used are listed in **Table S3**. The internal control is *Gapdh* or ribosomal protein *S18 (Rps18)*. The relative mRNA levels per sample were calculated by subtracting the detection limit (40 Ct) from the cycle threshold value (Ct) of each gene in the same sample to obtain the ΔCt value. Taking the log2 of −ΔCt resulted in the relative expression value of each gene for each sample expressed in arbitrary units. Each value was normalized against that of *Gapdh* or *Rps18*. The samples were run independently in triplicate.

MTT Assay

Cell viability was assessed with the MTT (3-(4,5-dimethylthiazol-2-yl)-2,5-diphenyltetrazolium bromide) colorimetric assay (Roche, #11465007001). Briefly, the cells were seeded in a 96-well plate for overnight until confluence reached approximately 90%, and the cells were then treated with AcLDL or AcLDL + 58035 for 24 hrs. Next, the MTT solution (5 mg/mL) was added to each well for 4 h at 37°C. The resulting formazan crystals were dissolved in solubilization solution and incubated overnight at 37°C. The optical density (OD) at 595nm was then read with a Multimode Plate Reader VICTOR X5 (PerkinElmer, USA). Each treatment was replicated six times.

Lipid Droplet Isolation and Quantification

The LDs were isolated from cells with the Lipid Droplet Isolation Kit (Cell Biolabs, Inc. MET-5011). In the final step, 200µl LDs from the top LD-enriched fractions in the tube (containing the floating LDs) were picked up and transferred to a fresh microcentrifuge tube. For quality control,

samples of LD-enriched fractions were subjected to western blot for the detection of Perilipin-1, 2 and 3; only the samples with no detectable GAPDH were used for further study. For the LD size-frequency distribution study, the LDs were diluted 10 times with PBS and stained with BODIPY 558/568 C12 (Thermo Fisher Scientific, D3835) for 15min in the dark. LDs were then put onto slides and observed under a fluorescence microscope on the TXRED channel (REVOLVE, VWR). Twenty images in different fields were randomly captured using a 10-x objective. The size of the LD was quantified with ImageJ software (NIH, Bethesda, MD, USA).

Nile Red Staining

Nile red staining was used to localize and quantitate intracellular lipids. Briefly, 10,000 cells/100µl were seeded either in a Corning 96-Well Black Polystyrene Microplate (Sigma, CLS3603-48EA) or on coverslips inside a petri dish filled with phenol red-free complete medium (Gibco, USA) overnight. The cells were exposed to AcLDL or AcLDL+58035 for 24 h. For fluorescence observation, cells were washed twice with PBS and fixed with 4% (wt/vol) paraformaldehyde (PFA) for 10 min. Then the fixed cells were washed twice with PBS and quenched with 50mM glycine in PBS for 10min. Intracellular neutral lipids were stained with Nile red staining solution (1:100 dilution from 10mg Nile red/10ml DMSO) for 15 min in the dark. Cell nuclei were stained with DAPI (4', 6-diamidino-2-phenylindole). All the staining procedures were performed at room temperature protecting the samples from light. Images were acquired with an inverted fluorescence microscope (REVOLVE, Echo, USA). LD size was quantified with ImageJ software.

Cholesterol Quantification

Total cholesterol and free cholesterol levels were measured with a Cholesterol Quantitation Kit (Sigma, MAK043-1KT). Briefly, 1×10^6 cells were trypsinized and washed with PBS, and 300ul of chloroform:isopropanol:IGEPAT CA-630 (7:11:0.1) was added in each 2ml microcentrifuge tube. The cells were homogenized by the TissueLyzer II (Qiagen, USA). After centrifugation, the organic phase was transferred to a new tube and dried at 50°C in a SpeedVac Concentrator (Thermo, SPD131DDA) for 30min to remove the chloroform. The dried lipids were then dissolved in Cholesterol Assay Buffer. A standard curve was prepared with cholesterol standard solution and cholesterol assay buffer. In a 96-well plate, 50 µl of samples and standards (1-5ng) were added to the reaction mixture and incubated at 37°C for 1 hr covered with aluminum foil. The absorbance was detected at 570nm with a Multimode Plate Reader VICTOR X5 (PerkinElmer, USA). Each sample was replicated four times.

Triacylglycerol (TAG) Quantification

Triglyceride quantification followed commercial kit instructions (#ab65336, Abcam) with modifications. Briefly, 10^6 cells were plated and harvested 24 hours after treatment. Cells were then resuspended and homogenized in 500 µl of 5% NP-40/ddH2O solution, followed by 5 minutes heat on a heater block and then cooled down to RT. Samples were centrifuged at 13,500 rpm for 5 mins, and 200 ul supernatant was transferred to a new tube for measurement. Standard was prepared following the instructions. Then, 50 ul of samples or standard were loaded to 96 well plates in duplicate, and 2 ul of ligase was added to each well for 20 mins incubation at RT. Finally, 50 ul of enzyme mix was added to each well of sample or standard, incubated for 1 hour at RT protected from light, and the absorbance read at 570 nm. The results were normalized to protein concentration.

Immunofluorescence Staining and Confocal Microscopy

The slides were baked at 65°C for 30 hrs prior to staining. After de-paraffinization with xylene, the slides were rehydrated with series gradient ethanol from 100%, 95%, 70%, 50% and rinsed with deionized H_2O. 0.1% Trion X-100 was used for permeabilization and 5% donkey serum in 3% BSA/PBS was used to block non-specific background. Anti-TSPO (1:400; polyclonal rabbit, generated by the Papadopoulos laboratory, see supplemental information) was incubated with the slides at 4°C overnight. The anti-Rabbit IgG (H+L) Highly Alexa Fluor 647 antibody (Cat# A-31573, Thermo Fisher Scientific) was incubated for 30 mins. DAPI was added for nuclear staining. Images were acquired with an inverted fluorescence microscope (REVOLVE, Echo, USA).

Cells were seeded onto coverslips at 200,000 cells/ml in 12-well plate. For mitochondria staining, 100 nM MitoTracker Deep Red FM (Thermo Fisher Scientific, M22426) was added to the cells. After treatment, cells were fixed in 4% PFA for 10 mins, followed by permeabilization with 0.1% Triton X-100 for 10 mins and blocking with 5% donkey serum in 3% BSA/PBS for 30 mins. The cells were then incubated with primary antibodies against TSPO or ACAT2 (See **Table S5**) at 4°C overnight. After rinsing with PBS, cells were incubated with the appropriate second antibodies (See antibodies in **Table S5**). DAPI was added for nuclear staining. Images were captured with a ZEISS LSM 880 with Airyscan confocal microscope (Carl Zeiss, Germany) using a 63× Oil objective. Identical settings were used for Scram and KD cells.

Immunoblotting and Co-immunoprecipitation (Co-IP)

The proteins were extracted with RIPA buffer (Santa Cruz Biotechnology USA, sc-24948A) containing Protease Inhibitor Tablets (Pierce, #A32963). Protein concentration was determined by BCA Protein Assay (Pierce, #23225). 10µg protein was subjected to 4-20% SDS-PAGE. After transfer to the PVDF (polyvinylidene difluoride) membrane, proteins were blocked in 5% BSA I PBS containing 0.1% Tween-20 (PBST) for 30 mins. The primary antibody was incubated with the membrane at 4°C overnight. After washing by PBST, the horseradish peroxidase-conjugated secondary antibody was added and incubated for 1 hr. After washing with PBST, the protein band was visualized by Chemiluminescent substrate for quantitative chemiluminescent western blots (Radiance Plus, #AC2103, Azure) on an Azure Biosystem (Azure c600) (Primary and secondary antibodies were listed in **Table S4**). GAPDH antibody or β-actin antibody was used as an internal control. The protein band was quantified by densitometry using Image J software.

For the Co-IP assay, PBR Human Tagged ORF Clone (TSPO; NM_000714; RC220107, Origene) and Human Tagged ORF Clone ACAT2 (NM_005891; RG201821, Origene) was transfected into WT Huh7 cells. The protein was extracted from the transfected cells with Lysis/Equilibration Buffer, the interaction between TSPO-Myc and ACAT2-TuboGFP protein was performed according to the instructions for Capturem™ IP & Co-IP Kit (Takara, #635721).

For the ACAT2 antibody IP assay, WT and TSPO KO mouse hepatocytes were isolated as above. After 3 hrs culture, the medium was replaced with DMEM supplemented with 10% Hi-FBS and 1% penicillin-streptomycin, and the cells were cultured for 24 hrs. Then the cells were harvested, and the cell pellets lysed according to the instruction of Immunoprecipitation kit (Abcam, Cat# ab206996). The solubilized protein was immunoprecipitated with anti-rabbit ACAT2 (Cell signaling, Cat# 13294). For the immunoblot, after the protein separation by SDS-PAGE, the PVDF

membrane was probed with Ubiquitin monoclonal antibody (Ubi-1, # 13-1600, Thermo Fisher Scientific).

Duolink Proximity Ligation Assay (PLA)

Duolink In Situ Red Starter Kit (DUO92105) was purchased by Sigma-Aldrich. The assay was run per kit instructions. Briefly, Huh7 cells were seeded on a coverslip overnight. After 4% PFA fixation, the cells were covered with blocking solution. The cells were then incubated with anti-goat TSPO (LifeSpan, Cat# LS-B5755-50) and anti-rabbit ACAT2 (Cell signaling, Cat# 13294) overnight. The Duolink In Situ PLA probe anti-rabbit PLUS and Duolink In Situ PLA probe anti-goat Minus was incubated with cells for 1hr at 37°C. The ligation and amplification proceeded per the manufacturer's instructions. Coverslips were mounted with Duolink In Situ Mounting Media with DAPI. The images were captured under a ZEISS LSM 880 with Airyscan confocal microscope (Carl Zeiss, Germany) using a 63× Oil objective.

Transmission Electronic Microscopy (TEM)

1×10^6 cells were harvested and fixed in 1/2 strength Karnovsky solution containing 2.5% glutaraldehyde (EM grade, Sigma) and 2% paraformaldehyde in PBS overnight at 4°C. The cell pellet was rinsed in 0.1M cacodylate buffer and post-fixed in 2% aqueous OsO_4/0.2M cacodylate buffer for 2 hours at 4°C, followed by rinsing several times with 0.1M cacodylate buffer. The cells were then EM-block stained with statured uranyl acetate at 4°C overnight. After rinsing with 0.1M sodium acetate buffer, the cells were dehydrated through a gradient series of: 70% EtOH (ethanol), 15 min; 90% EtOH, 15 mins; 100% EtOH, 2×15 mins; propylene oxide (PO)/EtOH (1:1), 15 mins; PO/ETOH (2:1), 15 mins; and PO, 2×15 mins. Cells were then infiltrated with Epon resin/PO (1:1) overnight. After that, the cells were placed into Epon resin/PO resin (2:1) for 8 hrs, followed by vacuum polymerization in 100% Epon resin overnight. Cells were then embedded in fresh Epon resin at 60 °C for 24 hrs and subjected to ultra-thin sectioning (~70nm). The thin sections were transferred to 200 mesh copper grids and stained with 2% uranyl acetate for 30 mins and 2.66% lead citrate (pH 12) for 10 mins. The images were acquired under transmission electron microscopy (JEM-2100 Electron Microscope, Japan) at the Doheny Eye Institute (Los Angeles, USA).

RNA-seq Library Preparation and Sequencing

Libraries for RNA-Seq were prepared with Kapa Stranded mRNA. The workflow consisted of mRNA enrichment, cDNA generation, end repair to generate blunt ends, A-tailing, adaptor ligation, and PCR amplification. Different adaptors were used for multiplexing samples in one lane. The RNA sequence data was generated on an HiSeq3000 for a single-read 50bp read run. A data quality check was done on an Illumina SAV. Demultiplexing was performed with Illumina Bcl2fastq2 v 2.17 program. RNA-seq data were deposited in the Gene Expression Omnibus under accession number GSE138666 (https://www.ncbi.nlm.nih.gov/geo/query/acc.cgi?acc=GSE138666).

RNA-seq Data Analysis

All analyses were performed in Partek® Flow® software, version 8. For alignment, unaligned sequenced reads were trimmed from both ends to a fixed-length dependent on the positional base at which the PHRED quality score fell below 20. A minimum read length filter retaining reads greater than 25 bases in length were used. Trimmed reads were aligned to the rat genome assembly, rn6 using the STAR (version 2.6.1d) aligner. A seed mismatch limit of 1 was applied. Raw read

counts were obtained by quantitating aligned reads to rn6 (Ensembl Transcripts release 96), using a modified version of the expectation-maximization algorithm. For normalization, reads with raw counts > 10 were normalized using the Upper Quartile (UQ) normalization method. An offset of 1.0 was added to all normalized read counts. Principle components analysis (PCA) was performed to assess the overall variability in the gene dataset, in which log transformation with a log base of 2 and a log cutoff of 1.0 was applied to all normalized read counts.

For differential expression analysis, normalized read counts for each gene were statistically modeled using differential gene expression algorithm (GSA) that uses the Akaike Information Criterion corrected (AICc). Comparisons were performed with KO MCD versus WT MCD, and KO CHOW versus WT CHOW, respectively. An expression filter based on the cutoff of absolute fold change > 1.2 and *P*-value < 0.05 was applied to select the differential expressed (DE) genes. Hierarchical cluster analysis was performed on the subset of DE genes that were normalized by standardizing the algorithm applied across genes. The analysis was run with Pearson Correlation distance measure and average linkage clustering option.

QUANTIFICATION AND STATISTICAL ANALYSIS

Statistical Analysis

Statistical analysis was performed with GraphPad Prism 8.4.3 (Graph Pad Software, USA). Data were presented as the means ± standard deviation (SD). Statistical significance of differences was determined using an independent t-test between two groups and significant differences more than two groups were evaluated by one-way ANOVA with Tukey-Kramer as post hoc test. $p < 0.05$ was considered statistically significant.

Key Resources Table for this study

REAGENT or RESOURCE	SOURCE	IDENTIFIER
Antibodies		
Monoclonal rabbit Anti-Human PBR (TSPO)	Abcam	Cat# ab109497; RRID: AB_10862345
Polyclonal rabbit Anti-Human FXR (NR1H4)	Abclonal	Cat# A12788; RRID: AB_2759628
Monoclonal rabbit Anti-Human ACAT2	Cell Signaling	Cat# 13294; RRID: AB_2798172
Monoclonal mouse Anti-Human Cyp7a1(clone 15B9.1)	Millipore Sigma	Cat# MABD42; RRID: AB_2756360
Polyclonal rabbit Anti-Human LC3B	Millipore Sigma	Cat# L7543; RRID: AB_796155
Polyclonal rabbit Anti-Human CYP27A1	Proteintech	Cat# 14739-1-AP; RRID: AB_2089276
Polyclonal rabbit Anti-Mouse TSPO	ProSci Inc	In this paper
Biological samples		
Human NAFLD samples	Research Institute of the McGill University Health Center, Montreal, Quebec, H4A 3J1, Canada. Department of Surgery, McGill University, Montreal, Quebec, H3G 1A4, Canada	In this paper
Healthy Human heart lysate	ProSci, Inc. CA, USA	Cat. No. 1470
Healthy Rat adrenal lysate	ProSci, Inc. CA, USA	Cat. No. 1470
Primary human hepatocytes	BioIVT Westbury, NY	Lot: JFC
Primary rat hepatic stellate cells (From Sprague Dawley)	Southern California Research Center for ALPD and Cirrhosis, Los Angeles, CA 90089, USA	https://keck.usc.edu/alpd-and-cirrhosis-research-center/

Primary rat hepatocytes (From Sprague Dawley)	Southern California Research Center for ALPD and Cirrhosis, Los Angeles, CA 90089, USA	https://keck.usc.edu/alpd-and-cirrhosis-research-center/
Primary ra Kupffer cells (From Sprague Dawley)	Southern California Research Center for ALPD and Cirrhosis, Los Angeles, CA 90089, USA	https://keck.usc.edu/alpd-and-cirrhosis-research-center/
Chemicals, peptides, and recombinant proteins		
U18666A	Calbiochem	Cat# 662015
Lipoprotein deficient serum from fetal calf	Kalen Biomedical, LLC	Cat# 880100-5
Goat-anti-rabbit HRP	Li-Cor	Cat# 926-80011
DAPI (4', 6-diamidino-2-phenylindole)	Life technologies	Cat# P36931
5-Androsten-3,17,19-triol	Mcule, Inc. CA, USA	Quotation reference I-10729
TSPO peptide	ProSci Inc	CWRDNSGRRGGSRLAE
58035	Sigma Aldrich	Cat#S9318
Bovine Serum Albumin (BSA), ≥98%, Fatty Acid-free, MP Biomedicals	Sigma Aldrich	Cat# IC15240105
Cholesterol–methyl-β-cyclodextrin	Sigma Aldrich	Cat# C4951-30MG
Chloroform	Sigma Aldrich	Cat# C2432
Collagenase, Type I	Sigma Aldrich	Cat# C0130
Ethanol	Sigma Aldrich	Cat# EX0276-1
Hydrocortisone	Sigma Aldrich	Cat# H0888
IGEPAL	Sigma Aldrich	Cat# 18896
Nile red	Sigma Aldrich	Cat# 19123
Oleic Acid-Albumin from bovine serum	Sigma Aldrich	Cat# O3008-5ML
Percoll	Sigma Aldrich	Cat# P4937
Tween® 20	Sigma Aldrich	Cat# 8221840500

BODIPY 558/568 C12	Thermo Fisher Scientific	Cat# D3835
Collagen I rat protein	Thermo Fisher Scientific	Cat# A1048301
Cocktail proteinase inhibitor	Thermo Fisher Scientific	Cat# 78430
DMEM, high glucose	Thermo Fisher Scientific	Cat# 11965118
Insulin	Thermo Fisher Scientific	Cat# 2585014
Low Density Lipoprotein from Human Plasma, Acetylated (AcLDL)	Thermo Fisher Scientific	Cat# L35354
Low Density Lipoprotein from Human Plasma, Acetylated, DiI complex (DiI AcLDL)	Thermo Fisher Scientific	Cat# L3484-200ul
NP-40 (Nonidet P-40) Surfact-Amps™ Detergent Solution	Thermo Fisher Scientific	Cat# PI85125
Pierce™ Protein A Plus Agarose	Thermo Fisher Scientific	Cat# 22811
Puromycin Dihydrochloride	Thermo Fisher Scientific	Cat# A1113803
Dimethyl sulfoxide (DMSO)	VWR	Cat# 80058-040
Isopropanol	VWR	Cat# BDH133
Critical commercial assays		
Immunoprecipitation kit	Abcam	Cat# ab206996
Triglyceride Assay Kit - Quantification	Abcam	Cat#: ab65336
Picro-Sirius Red Stain Kit	American MasterTech	Pint Kit Item: KTPSRPT
Matrix-assisted laser desorption/ionization (MALDI) imaging mass spectrometry (IMS)	BRUKER	N/A
Lipid Droplet Isolation Kit	Cell Biolabs, Inc.	Cat# MET-5011
Lipofectamine™ RNAiMAX Transfection Reagent	Invitrogen	Cat# 13778150
HPLC	ProSci Inc	N/A
MTT	Sigma Aldrich	Cat#11465007001
Cholesterol Quantification kit	Sigma Aldrich	Cat#MAK043-1KT

Duolink In Situ Red Starter Kit	Sigma Aldrich	Cat# DUO92105
PrimeScript RT reagent kit	TAKARA	Cat# RR037A
SYBR Green Real-Time PCR Master	Thermo Fisher Scientific	Cat# A25742
Lipofectamine™ 3000 Transfection Reagent	Thermo Fisher Scientific	Cat# L3000001
Quick-RNA™ MiniPrep	Zymo Research	Cat# R1054 & R1055
Deposited data		
Raw and analyzed data	This paper	GEO: GSE127915
Experimental models: cell lines		
Huh7 cell line	JCRB Cell Bank	Cat# 0403
MA-10 cells	Fan et al., 2018	In this paper
Experimental models: organisms/strains		
Rat Sprague Dawley: TSPO heterozygous (Het)	David R. Owen., 2017	Biochemical Journal 474, 3985-3999.
Rat Sprague Dawley: TSPO homozygous (HO, in main text as KO)	David R. Owen., 2017	Biochemical Journal 474, 3985-3999.
Mouse C57BL6/J	Wang, X, 2016	Cell Metab 24, 848-862.
Mouse C57BL/6J mouse: TSPO KO	Fan, Jinjiang, 2020	J Endocr Soc 4, bvaa001.
Oligonucleotides		
Human TSPO siRNA: SASI_Hs01_00054085	Millipore Sigma	NM_000714
Human TSPO siRNA: SASI_Hs01_00054086	Millipore Sigma	NM_000714
Human TSPO siRNA: SASI_Hs01_00054085	Millipore Sigma	NM_000714
negative control siRNA	Millipore Sigma	SIC001-5X1NMOL
Recombinant DNA		
PBR shRNA Plasmid (h)	Santa Cruz	Cat#: sc-40821-SH
Control shRNA Plasmid-A	Santa Cruz	Cat#: sc-108060
Software and algorithms		
Photoshop CS6	Adobe	Adobe Photoshop Version: 19.0 20170929.r.165 2017/09/29: 1138933 x64

SCiLS	Bruker	https://www.bruker.com/en/products-and-solutions/mass-spectrometry/ms-software/scils-lab.html
Zen lite	Carl Zeiss Microscopy, LLC	https://www.zeiss.com/microscopy/us/home.html
GraphPad Prism 7	GraphPad Software	http://www.graphpad.com
Aperio ImageScope software	Leica Biosystems	https://www.leicabiosystems.com/digital-pathology/manage/aperio-imagescope/
Primer-Blast	NCBI	https://www.ncbi.nlm.nih.gov/tools/primer-blast/index.cgi?LINK_LOC=BlastHome
ImageJ Software	NIH	https://imagej.nih.gov/ij/
Partek Flow	Partek Flow	https://libguides.usc.edu/healthsciences/PartekFlow
Ingenuity Pathway Analysis 2019	Qiagen	https://www.qiagenbioinformatics.com/products/ingenuity-pathway-analysis/
Other		
Chow Diet, 18% Calories from Fat	Harlan Teklad	# 2018
MCD diet	MP Biomedicals	#960439
Picro-Sirius Red Pint Stain Kit/Ea	American MasterTech	Cat# KTPSRPT
MitoTracker™ Deep Red FM	Thermo Fisher Scientific	Cat# M22426
Pierce™ IP Lysis Buffer	Thermo Fisher Scientific	Cat# 87787

Table S1. NAFLD activity score (NAS) for the patient liver samples. Related to main Figures 1.

								NAS staging								
Sample	**Sex**	**Age**	**BMI**	**Diabetic**	**Smoking**	**Type of Procedure**	**Diagnosis**	**Steatosis**	**Lobular Inflammation**	**Hepatocyte Ballooning**	**Fibrosis score**	**% Micro steatosis**	**% Macro steatosis**	**% Total steatosis**	**NAS**	**Grading**
1	Female	52	21	No	No	Resection	Biliary cystadenoma	0	0	1	1A	0	0	0	2	Normal (Low)
2	Female	51	20	Yes	No	Resection	CRCLM	0	1	0	1A	0	0	0	2	Normal (Low)
3	Male	67	20	No	Yes	Resection	CRCLM	0	1	0	1A	1	3	4	2	Normal (Low)
4	Male	64	24	No	No	Resection	CRCLM	2	1	0	1A	15	30	45	4	Steatosis (NAFLD)
5	Male	52	25	No	No	Resection	CRCLM	2	1	1	1A	10	40	50	5	Steatosis (NAFLD)
6	Female	78	19.6	No	No	Resection	CRCLM	0	1	1	1A	0.5	0.5	1	3	Steatosis (NAFLD)
7	Female	65	30	Yes	No	Resection	CRCLM	2	2	1	1A	10	30	40	6	NASH
8	Male	67	20	No	No	Resection	Net carcinoid tumor	2	3	2	1C	10	50	60	8	NASH
9	Female	72	25	No	No	Resection	CRCLM	1	2	1	2	1	9	10	6	NASH
10	Female	65	25	No	No	Resection	Benign	0	3	1	3	0	0	0	7	Cirrhosis
11	Male	75	28	Yes	No	Resection	Benign	0	3	1 or 2	3	1	3	4	7	Cirrhosis
12	Male	70	18	No	No	Resection	Klatskin tumor /Cholangiocarcinoma	0	3	2	3	0	0	0	8	Cirrhosis

Note: BMI, body mass index; CRCLM: colorectal cancer liver metastases

Table S2. Ingenuity Pathway Analysis of the genes involved in the liver diseases and functions. Related to main Figures 7.

Categories	**Diseases or Functions Annotation**	**p-value**	**Molecules**
Liver Proliferation	Proliferation of liver cells	0.00495	BMP7, IFT88, LGALS1, PIK3R1, SLC20A1, SOCS3
Liver Proliferation	Proliferation of hepatocytes	0.0347	BMP7, IFT88, SLC20A1, SOCS3
Liver Proliferation	Proliferation of oval cells	0.0892	IFT88
Liver Fibrosis, Liver Proliferation	Proliferation of hepatic stellate cells	0.303	LGALS1
Categories	**Diseases or Functions Annotation**	**p-value**	**Molecules**
Glutathione Depletion In Liver	Conjugation of glutathione	0.00772	GSTA5, GSTM1
Categories	**Diseases or Functions Annotation**	**p-value**	**Molecules**
Liver Damage	Histopathological change of liver	0.0328	DLL4
Liver Damage	Liver Damage	0.26	ADM, DLL4, TM4SF4, TSPO
Liver Damage	Hepatic injury	0.331	ADM, TM4SF4, TSPO
Categories	**Diseases or Functions Annotation**	**p-value**	**Molecules**
Biliary Hyperplasia	Hyperplasia of bile duct cells	0.00665	IFT88
Categories	**Diseases or Functions Annotation**	**p-value**	**Molecules**
Liver Cirrhosis	Cirrhosis	0.00712	CD180, CYP3A5, GCLM, GUCY1A1, IL12RB2, SSTR3, TSPO
Liver Cirrhosis	Cirrhosis of liver	0.0794	CD180, CYP3A5, GCLM, IL12RB2
Liver Cirrhosis	Compensated cirrhosis	0.0831	CYP3A5
Liver Cirrhosis	Primary biliary cirrhosis	0.145	CD180, IL12RB2
Categories	**Diseases or Functions Annotation**	**p-value**	**Molecules**
Liver Fibrosis	Fibrosis of liver portal space	0.0133	IFT88
Liver Fibrosis	Fibrosis of liver	0.0276	BMP7, IFT88, SIRT6, SOCS3
Liver Fibrosis	Migration of hepatic stellate cells	0.142	LGALS1
Liver Fibrosis, Liver Proliferation	Proliferation of hepatic stellate cells	0.303	LGALS1
Categories	**Diseases or Functions Annotation**	**p-value**	**Molecules**
Liver Inflammation/Hepatitis	Chronic inflammation of liver	0.0133	SIRT6
Liver Inflammation/Hepatitis	Infection by Hepatitis C virus genotype 1	0.0831	CYP3A5
Liver Inflammation/Hepatitis	Experimental hepatitis	0.119	SOCS3
Liver Inflammation/Hepatitis	Inflammation of liver	0.192	CYP3A5, IL12RB2, SIRT6, SOCS3, TSPO
Liver Inflammation/Hepatitis	Infection by hepatitis B virus	0.422	CYP3A5
Categories	**Diseases or Functions Annotation**	**p-value**	**Molecules**
Hepatocellular carcinoma, Liver Hyperplasia/Hyperproliferation	Metastasis of hepatocellular carcinoma	0.0198	PIK3R1
Liver Hyperplasia/Hyperproliferation	Early stage liver cancer	0.0263	SIRT6
Hepatocellular carcinoma, Liver Hyperplasia/Hyperproliferation	Development of hepatocellular carcinoma	0.0363	MGMT, PIK3R1, SOCS3
Liver Hyperplasia/Hyperproliferation	Relapsed hepatosplenic T-cell lymphoma	0.0393	POLE
Liver Hyperplasia/Hyperproliferation	Refractory hepatosplenic T-cell lymphoma	0.0393	POLE
Liver Hyperplasia/Hyperproliferation	Resectable liver cholangiocarcinoma	0.0393	POLE
Liver Hyperplasia/Hyperproliferation	Advanced liver tumor	0.0792	POLE, SSTR3
Liver Hyperplasia/Hyperproliferation	Unresectable liver cholangiocarcinoma	0.0831	POLE
Liver Hyperplasia/Hyperproliferation	Hyperplasia of liver	0.107	IFT88
Hepatocellular carcinoma, Liver Hyperplasia/Hyperproliferation	Hepatocellular carcinoma	0.133	ADCY2, AOX1, BMP7, DUSP11, ETS1, ID1, MGMT, PIK3R1, POLE, SCIMP, SOCS3, SSTR3
Liver Hyperplasia/Hyperproliferation	Locally advanced liver cholangiocarcinoma	0.148	POLE

Liver Hyperplasia/Hyperproliferation	Proliferation of liver cancer cells	0.165	SOCS3
Liver Hyperplasia/Hyperproliferation	Metastatic liver cholangiocarcinoma	0.171	POLE
Hepatocellular carcinoma, Liver Hyperplasia/Hyperproliferation	Advanced hepatocellular carcinoma	0.229	SSTR3
Hepatocellular carcinoma, Liver Hyperplasia/Hyperproliferation	Childhood type hepatocellular carcinoma	0.234	POLE
Liver Hyperplasia/Hyperproliferation	Hepatoblastoma	0.289	POLE
Liver Hyperplasia/Hyperproliferation	Liver tumor	0.337	AASS, ADCY2, AMOT, AOX1, APBA2, ARHGAP32, ARHGEF7, ATXN2, BMP7, CYP3A5, DACT2, DDIT4, DTX4, DUSP11, ETS1, GNAI1, GREB1L, GSTA5, GSTM1, HIST1H3G, ID1, IFT88, KCNJ5, KLF10, LSAMP, MCM4, MEX3B, MGMT, NAV2, NKIRAS1, PARP8, PHOSPHO2, PIK3R1, PLXND1, POLE, PRLR, RCSD1, REEP1, RPL37, RXRG, SCIMP, SEPHS2, SGPL1, SIRT6, SLC25A15, SLC39A4, SOCS3, SSTR3, TMEM167B, TMEM56, UBXN2A, WDR62, ZNF48, ZNHIT2
Liver Hyperplasia/Hyperproliferation	Liver cancer	0.374	AASS, ADCY2, AMOT, AOX1, APBA2, ARHGEF7, ATXN2, BMP7, CYP3A5, DACT2, DDIT4, DTX4, DUSP11, ETS1, GNAI1, GREB1L, GSTA5, GSTM1, HIST1H3G, ID1, KLF10, LSAMP, MCM4, MEX3B, MGMT, NAV2, PHOSPHO2, PIK3R1, PLXND1, POLE, RCSD1, REEP1, RPL37, RXRG, SCIMP, SEPHS2, SGPL1, SIRT6, SLC39A4, SOCS3, SSTR3, TMEM167B, UBXN2A, WDR62, ZNF48, ZNHIT2
Liver Hyperplasia/Hyperproliferation	Liver carcinoma	0.402	AASS, ADCY2, AMOT, AOX1, APBA2, ARHGEF7, ATXN2, BMP7, CYP3A5, DACT2, DDIT4, DTX4, DUSP11, ETS1, GNAI1, GREB1L, GSTA5, HIST1H3G, ID1, KLF10, LSAMP, MCM4, MEX3B, MGMT, NAV2, PHOSPHO2, PIK3R1, PLXND1, POLE, RCSD1, REEP1, RPL37, RXRG, SCIMP, SEPHS2, SGPL1, SLC39A4, SOCS3, SSTR3, TMEM167B, UBXN2A, WDR62, ZNF48, ZNHIT2
Categories	**Diseases or Functions Annotation**	**p-value**	**Molecules**
Hepatocellular Peroxisome Proliferation	Formation of peroxisome membrane	0.0263	PEX11A

Table S3. Primers sequences used in the study. Related to main Figures 1, 4, 7.

SPECIES	GENE	FORWARD 5' ⟶ 3'	REVERSE 5' ⟶ 3'
Mus musculus	*Acat2*	GCGAACGCATCAGGAATGAA	TAGCTATTGCCGCAGACACC
	Dgat2	CATCACCACCGTCGTGGG	CTCCCAGGAGCTGGCAC
	Fasn	TCCGAGACCTCGCAGGTATTA	CTGTCGTGTCAGTAGCCGAGT
	Gapdh	GTTGTCTCCTGCGACTTCA	GGTGGTCCAGGGTTTCTTA
	Hmgcr	GCGTGGGATCCAAGGACTG	GCTCAGCACGTCCTCTTCAA
	LXRa	CGACAGTTTTGGTAGAGGGACA	CGCTTTTGTGGACGAAGCTC
	Plin1	CTGTCTGAGACTGAGGTGGC	TTCTCCTGCTCAGGGAGGTC
	Plin2	GCTCTCCTGTTAGGCGTCTC	TTGGCCACTCTCATCACCAC
	Ppara	GTGCAGCCTCAGCCAAGTT	TGGGGAGAGAGGACAGATGG
	Rps18	GTTGGTGGAGCGATTTGTCTGGTT	TATTGCTCAATCTCGGGTGGCTGA
	Scd1	CCCTCCGGAAATGAACGAGAG	AAAATCCCGAAGAGGCAGGTG
	Srebp-1c	GGGGCCTGACAGGTGAAATC	TGAGCTGGAGCATGTCTTCAAA
	Tspo	TAGCTTGCAGAAACCCTCTTGGCA	TGTGAAACCTCCCAGCTCTTTCCA
Rattus norvegicus	*Gapdh*	CCATTCTTCCACCTTTGATGCT	TGTTGCTGTAGCCATATTCATTGT
	F4/80	TGTCCAGCTTATGCCACCTG	TGGGCCCTGAAAGTTGGTTT
	Fgf21	ACCGCAGTCCAGAAAGTCTC	TGCAGGCCTCAGGATCAAAG
	Fxr	ATGCTGAAGCTTATGCCGGA	AAGATCCTTGGATTGCTTTGGG
	Lgals1	TACACTTCAACCCCCGCTTC	TGATGCACACCTCCGTGATG
	Rps18	ATAGCCAGGTTCTGGCCAAC	TTGGACACACCCACAGTACG
	Slc20a1	CATCCTCCGTAAGGCAGATCC	GAAAACTGCACATCCCACCG
	Tnfa	ATGGGCTCCCTCTCATCAGT	GCTTGGTGGTTTGCTACGAC
	Tspo	AGAGCATACTCTTGCCGTCG	ACTCCTAAAGGGGTTGCAGG

Table S4. List of antibodies used in western blotting. Related to main Figures 2-7.

PRIMARY ANTIBODIES	SUPPLIER	REFERENCE	DILUTION
GRP-78	Abcam	Cat# ab21685; RRID: AB_2119834	1:1000
HMGCR	Abcam	Cat# ab174830; RRID: AB_2749818	1:1000
Oxidative Stress Defense (Catalase, SOD1, TRX, smooth muscle Actin)	Abcam	Cat# ab179843; RRID: AB_2716714	1:250
PPAR alpha	Abcam	Cat# ab24509; RRID: AB_448110	1:1000
FXR	Abclonal	Cat# A12788; RRID: AB_2759628	1:1000
PLIN2	Abclonal	Cat# A6276; RRID: AB_2766881	1:1000
PERK	Cell signaling	Cat# 3192; RRID: AB_2095847	1:1000
IRE1α	Cell signaling	Cat# 3294; RRID: AB_823545	1:1000
ACAT2	Cell signaling	Cat# 13294; RRID: AB_2798172	1:1000
LAMP1	Cell signaling	Cat# 9091; RRID: AB_2687579	1:1000
ATF-4 (D4B8)	Cell signaling	Cat# 11815; RRID: AB_2616025	1:1000
α-Smooth Muscle Actin	Cell Signaling	Cat# 14968; RRID: AB_2798667	1:1000
ATG12 (D88H11)	Cell signaling	Cat# 4180; RRID: AB_1903898	1:1000

β-ACTIN	Cell signaling	Cat# 4970; RRID: AB_2223172	1:2000
CHOP (D46F1)	Cell signaling	Cat# 5554; RRID: AB_10694399	1:1000
GAPDH	Cell signaling	Cat# 2118; RRID: AB_561053	1:2000
MYC-Tag	Cell signaling	Cat# 2278; RRID: AB_490778	1:1000
CYP7A1	Millipore	Cat# MABD42; RRID: AB_2756360	1:1000
TSPO	ProSci Inc	Generated by Dr. Papadopoulos lab, see supplemental information	1:1000
Lamp2	Proteintech	Cat# 10397-1-AP; RRID: AB_2134630	1:1000
ACOX1	Proteintech	Cat# 10957-1-AP; RRID: AB_2221670	1:1000
TNF Alpha	Proteintech	Cat# 17590-1-AP; RRID: AB_2271853	1:1000
CYP27A1	Proteintech	Cat# 14739-1-AP; RRID: AB_2089276	1:1000
α-Tubulin	Sigma-Aldrich	Cat# T9026; RRID: AB_477593	1:10000
LC3B	Sigma-Aldrich	Cat# L7543; RRID: AB_796155	1:2000
CEH	Thermo Fisher Scientific	Cat# PA5-50285; RRID: AB_2635738	1:1000
CHOP	Thermo Fisher Scientific	Cat# MA1-250; RRID: AB_2292611	1:1000
TurboGFP	Thermo Fisher Scientific	Cat# PA5-22688; RRID: AB_2540616	1:1000
Ubiquitin	Thermo Fisher Scientific	Cat# 13-1600; RRID: AB_2533002	1:1000
ATF6	Novus Biological	Cat# NBP1-40256; RRID: AB_2058774	1:1000
SECONDARY ANTIBODIES	**SUPPLIER**	**REFERENCE**	**DILUTION**
Anti-Mouse IgG H&L (HRP)	Abcam	Cat# ab6728; RRID: AB_955440	1:1000
Anti-Rabbit HRP	Li-Cor	Cat# 926-80011; RRID: AB_2721264	1:10000

Table S5. List of antibodies used in immunohistochemistry and immunofluorescence. Related to main Figures 1, 3 and 5.

PRIMARY ANTIBODIES	SUPPLIER	REFERENCE	DILUTION
TSPO	Abcam	Cat# ab109497; RRID: AB_10862345	1:2000
ACAT2	Cell signaling	Cat# 13294; RRID: AB_2798172	1:400
TSPO	LifeSpan	Cat# LS-B5755-50; RRID: AB_10914795	1:400
CHOP	Thermo Fisher Scientific	Cat# MA1-250; RRID: AB_2292611	1:400
TSPO	ProSci Inc	Generated by Dr. Papadopoulos lab	1:1000
SECONDARY ANTIBODIES	**SUPPLIER**	**REFERENCE**	**DILUTION**
Anti-Rabbit IgG (H+L) Highly Alexa Fluor 488	Thermo Fisher Scientific	Cat# A-21206; RRID: AB_2535792	1:400
Anti-Rabbit IgG (H+L) Highly Alexa Fluor 647	Thermo Fisher Scientific	Cat# A-31573; RRID: AB_2536183	1:400
Anti-Rabbit IgG (H+L) Highly Alexa Fluor 647	Thermo Fisher Scientific	Cat# A-31573; RRID: AB_2536183	1:400

Anti-Rabbit IgG (H+L) Highly Alexa Fluor 647	Thermo Fisher Scientific	Cat# A-31573; RRID: AB_2536183	1:400

Table S6. ELISA results for affinity purification. Related to main Figures 1, 7.

Dilutions	Serum before purification (OD450)	Immunodepleted (flow-through) after purification (OD450)	Purified Antibody at 1.0 mg/ml (OD450)
1:1,000	2.225	0.349	2.856
1:5,000	0.706	0.111	1.857
1:25,000	0.22	Not tested	0.694
1:125,000	0.092	Not tested	0.22
1:625,000	0.063	Not tested	0.105

Abbreviations: ELISA, enzyme-linked immunosorbent assay

ADDITIONAL RESOURCES

Generation and Characterization of TSPO Polyclonal Antibody

To date, there is no commercial TSPO antibody available for the protein detection in across human, mouse and/or rat species. Therefore, we attempted to generate a TSPO antibody applicable to human, mouse and rat. After comparison of all the peptide sequences from manufacturers and the literature (Hatori et al., 2012; Ji et al., 2008), we picked the peptide sequence of WRDNSGRRGGSRLAE (**Fig. S11A**) for the synthesis and performed immunogen administration into rabbits (ProSci. Inc. CA. USA). The immunoaffinity purification was performed through a chromatography column prepared by cross-linking of the synthesized TSPO peptide (CWRDNSGRRGGSRLAE) with cysteine to a CNBr-activated Sepharose 4B gel. A direct ELISA was conducted with the serum, immunodepleted serum (or "flow-through"), and the purified antibody to check the efficiency of the purification product. These three fractions were initially brought to 1.0mg/ml and then diluted in as given **(Table S6**), and the optical density (OD) readings taken as shown. The gradient dilution of the purified anti-TSPO antibody suggested an immune response to the antigen.

Next, we examined the antibody in tissue or cells from different species. Using this anti-rabbit TSPO antibody in immunoblots, we could detect TSPO as a 36kDa band in human heart lysate (Cat. No.: 1401, ProSci, Inc. CA, USA) (**Fig. S11B**), an 18kDa band in rat adrenal lysate (Cat. No. 1470, ProSci, Inc. CA, USA) (**Fig. S11C**) and an 18kDa band in MA-10 mouse tumor Leydig cells (**Fig. S11D**). With the cell lysate from mouse MA-10 and TSPO KO MA-10 cells (Fan et al., 2018), there is 18kDa band in wild type MA-10 but no expression in TSPO KO MA-10 cells, further confirmation of the knockout of TSPO mediated by CRISPR/CAS9 in MA-10 cells (**Fig. S11E**) and the specificity of the antibody. Using primary hepatocytes from a male C57BL/6 wild type and a male TSPO KO mouse, after probing with TSPO antibody, results showed TSPO expression in wild type but no expression in KO hepatocytes (**Fig. S11F**), indicative of TSPO recognition by the generated TSPO antibody in mouse hepatocytes.

Because TSPO is a resident protein in outer mitochondrial membrane, we examined TSPO distribution in Huh7 cells under confocal laser-scanning microscopy. The results showed that TSPO was localized mainly in the mitochondrial membrane, evidenced by co-staining with MitoTracker (**Fig. S11G**), a mitochondrial maker. In MA-10 cells, we observed TSPO located in the mitochondrial membrane but not detected in TSPO KO MA-10 cells (Fan et al., 2018; **Fig. S11H**). These observations confirmed that the TSPO antibody we generated is applicable to the detection of TSPO in human, mouse, and rat. This TSPO antibody was used for immunofluorescence staining (**Fig. 1B, 2B** and **Fig. S11 G, H**) and immunoblot (**Fig. 7E**) in our present study.

Supplemental References

Hatori, A., Yui, J., Yamasaki, T., Xie, L., Kumata, K., Fujinaga, M., Yoshida, Y., Ogawa, M., Nengaki, N., Kawamura, K.*, et al.* (2012). PET imaging of lung inflammation with [18F]FEDAC, a radioligand for translocator protein (18 kDa). PLoS One *7*, e45065.

Ji, B., Maeda, J., Sawada, M., Ono, M., Okauchi, T., Inaji, M., Zhang, M.R., Suzuki, K., Ando, K., Staufenbiel, M.*, et al.* (2008). Imaging of Peripheral Benzodiazepine Receptor Expression as Biomarkers of Detrimental versus Beneficial Glial Responses in Mouse Models of Alzheimer's and Other CNS Pathologies. Journal of Neuroscience *28*, 12255-12267.

Li, Y., Lua, I., French, S.W., and Asahina, K. (2016). Role of TGF-beta signaling in differentiation of mesothelial cells to vitamin A-poor hepatic stellate cells in liver fibrosis. Am J Physiol Gastrointest Liver Physiol *310*, G262-272.

Severgnini, M., Sherman, J., Sehgal, A., Jayaprakash, N.K., Aubin, J., Wang, G., Zhang, L., Peng, C.G., Yucius, K., Butler, J.*, et al.* (2012). A rapid two-step method for isolation of functional primary mouse hepatocytes: cell characterization and asialoglycoprotein receptor based assay development. Cytotechnology *64*, 187-195.

Sugahara, G., Ishida, Y., Sun, J., Tateno, C., and Saito, T. (2020). Art of Making Artificial Liver: Depicting Human Liver Biology and Diseases in Mice. Semin Liver Dis *40*, 189-212.

Xiong, S., She, H., Zhang, A.S., Wang, J., Mkrtchyan, H., Dynnyk, A., Gordeuk, V.R., French, S.W., Enns, C.A., and Tsukamoto, H. (2008). Hepatic macrophage iron aggravates experimental alcoholic steatohepatitis. Am J Physiol Gastrointest Liver Physiol *295*, G512-521.